

Научном већу Института за физику у Београду

Београд, 29. 3. 2019.

Предмет: Покретање поступка за избор у звање истраживач сарадник

Молим Научно веће Института за физику у Београду да покрене поступак за мој избор у звање истраживач сарадник.

У прилогу достављам:

1. мишљење руководиоца пројекта са предлогом комисије за избор у звање;
2. стручну биографију;
3. преглед научне активности;
4. списак и копије објављених научних радова и других публикација;
5. уверење о последњем овереном и уписаном семестру на докторским студијама;
6. уверења о завршеним основним и мастер академским студијама;
7. потврду о прихватању предлога теме докторске дисертације.

С поштовањем,

Ива Бачић

Истраживач приправник



Научном већу Института за физику у Београду

Београд, 1. март 2019. године

Предмет: Мишљење руководиоца пројекта о избору Иве Бачић у звање истраживач сарадник

Ива Бачић је запослена у Лабораторији за примену рачунара у науци, у оквиру Националног центра изузетних вредности за изучавање комплексних система Института за физику у Београду и ангажована је на пројекту основних истраживања Министарства просвете, науке и технолошког развоја Републике Србије ОН171017, под називом "Моделирање и нумеричке симулације сложених вишечестичних физичких система". На поменутом пројекту ради на темама из самоорганизације у спрегнутим ексцитабилним системима под руководством др Игора Франовића. С обзиром да испуњава све предвиђене услове у складу са Правилником о поступку, начину вредновања и квантитативном исказивању научноистраживачких резултата истраживача МПНТР, сагласан сам са покретањем поступка за избор Иве Бачић у звање истраживач сарадник.

За састав комисије за избор Иве Бачић у звање истраживач сарадник предлажем:

- (1) др Игор Франовић, научни сарадник, Институт за физику у Београду,
- (2) др Антун Балаж, научни саветник, Институт за физику у Београду,
- (3) проф. др Милан Кнежевић, редовни професор Физичког факултета Универзитета у Београду.



др Антун Балаж
научни саветник
руководилац пројекта ОН171017

Биографија Иве Бачић

Ива Бачић рођена је у Суботици 12. јуна 1992. године, где је завршила основну школу и природни смер Гимназије „Светозар Марковић“. Након тога, уписала је 2010. године основне академске студије на Физичком факултету Универзитета у Београду, смер Теоријска и експериментална физика, где је дипломирала 2014. године са просечном оценом 9.44/10. Исте године је уписала мастер академске студије на Физичком факултету, смер Теоријска и експериментална физика, које је завршила 2015. године са просечном оценом 9.67/10. У току мастер студија, Ива је посетила синхротрон SOLEIL у Француској, у склопу израде мастер рада на тему *Inner-Shell Action Spectroscopy of Trapped Substance P Peptide Ions and their Nanosolvated Complexes*, под менторством др Александра Милосављевића, вишег научног сарадника Института за физику у Београду. Мастер рад је оцењен оценом 10, а резултати рада су у представљени на конференцији COST XLIC WG2 Expert Meeting on Biomolecules на Фрушкој Гори у априлу 2015. године. Новембра 2015. године, Ива је уписала докторске академске студије на Физичком факултету, ужа научна област Статистичка физика. Под менторством др Игора Франовића, научног сарадника из Лабораторије за примену рачунара у науци (Scientific Computing Laboratory) Института за физику у Београду, Ива се у склопу докторских академских студија бави коефектима шума и вишеструких временских скала у системима спрегнутих ексциtabilних јединица.

Од марта 2016. године, Ива је запослена на Институту за физику у Београду на позицији истраживач приправник у Лабораторији за примену рачунара у науци, где је ангажована на пројекту основних истраживања ОН171017 *Моделирање и нумеричке симулације сложених вишечестичних система* Министарства просвете, науке и технолошког развоја Републике Србије. Поред тога, учествовала је и у DAAD билатералном пројекту између Републике Србије и СР Немачке *Emergent dynamics in systems of coupled excitable units* 2017. и 2018. године, у оквиру ког је више пута посетила Weierstrass Institute (WIAS) у Берлину, Немачка, као и Технички универзитет у Берлину, Немачка. Такође, Ива учествује и на COST акцији CA17120 *Chemobionics* од 2018. године.

Ива је до сада је објавила три научна рада категорије M21, један рад категорије M22 и два саопштења са међународних скупова штампана у изводу (M34). Ивин рад *Disordered configurations of the Glauber model in two-dimensional networks*, објављен у часопису *EPL (Europhysics Letters)*, истакнут је у *Research Highlights* за 2018. годину на *Europhysics News*. Своје резултате је до сада представила на семинару на WIAS-у, као и на конференцији *Dynamics of Coupled Oscillator Systems* на WIAS-у. Позвана је на студијско усавршавање на зимску школу *Complexity Science Hub Winter School*, која ће се одржати 2019. године у Обергурглу, Аустрија.

Поред матерњег, Ива говори два светска језика, енглески и немачки.

Преглед научне активности Иве Бачић

Током мастер студија, Ива се бавила интеракцијом синхротронског зрачења са наносолватисаним молекулама. Под руководством др Александра Милосављевића, научног саветника из Лабораторије за физику сударних процеса Института за физику у Београду, на синхротрону SOLEIL у Француској, користећи тандем масену X-ray спектрометрију биополимера у јонској замци, испитивала је ефекте наносолватације на акционе спектре и фрагментацију. Уочена су два различита резонантна процеса која доводе до појачаног губитка воде са наносолватисаних молекула неuropeптида *Substance P*, повезана са ексцитацијом К-љуске кисеоникових атома који припадају или пептидној вези или кластеру молекула воде. Разматрање процеса фрагментације пептида као функције активационе енергије фотона у близини C, N и O К-ивице показало је да фрагментација има јаку зависност од активационе енергије.

У склопу докторских студија, под руководством др Игора Франовића, научног сарадника из Лабораторије за примену рачунара у науци Института за физику у Београду, Ива се бави емергентним феноменима у спрегнутим системима, насталим услед садејства шума, адаптивности у интеракцији и локалне ексцитабилности. Ексцитабилност је заједничка карактеристика великог броја система, укључујући многобројне биолошке системе (неуронске мреже, срчано ткиво, бета ћелије панкреаса, генске регулаторне мреже), моделе хемијске кинетике, ласере, моделе социјалних интеракција, климатске динамике, земљотреса и др. Са аспекта теорије нелинеарних динамичких система, особина ексцитабилности је заснована на чињеници да се систем налази у близини бифуркације од стационарног ка осцилаторном режиму. Манифестујући богато колективно понашање, укључујући низ феномена синхронизације и парцијална синхронизације, патерне, таласе ексцитације, просторно локализована решења и др, системи интерагујућих ексцитабилних јединица издвојени су у посебну класу динамичких система.

Комплексна динамика у ексцитабилним системима често укључује више карактеристичних временских скала на нивоу појединачних јединица (тзв. *slow-fast* динамика) и/или услед интеракција. Један од најважнијих примера где динамика интеракција укључује вишеструке временске скале односи се на концепт адаптивности, који подразумева коеволуцију локалне динамике и динамике интеракција. При томе, динамика веза (јачина интеракција, промена броја линкова) одвија се на споријој карактеристичној скали у односу на локалну динамику јединица. Међу најважнијим примерима система са адаптивношћу истичу се неуронски системи, где се у оквиру пластичности синапси, јачина синаптичких веза повећава или смањује у складу са релативним временима опаљивања пре- и пост-синаптичког неурона.

Модели система спрегнутих ексциtabilних јединица типично укључују деловање шума, који потиче интринзичних флукуација, флукуација у окружењу или од *coarse-grained* динамике на нижим просторним и временским скалама. Неки од извора шума у ексциtabilних системима укључују *quasi-random* ослобађање неуротрансмитера у неуронима или *finite-size* ефекте у хемијским реакцијама. Под утицајем шума, особина ексциtabilности постаје израженија. Познато је да шум у системима који се налазе у близини бифуркационог прага може да индукује тзв. резонантне феномене, који подразумевају нелинеаран одговор система на шум, као последицу тога што шум уводи нову временску скалу у систем. У случају класичних ексциtabilних система, добро је познат феномен резонанце кохеренце, где осцилације изазване шумом постају најрегуларније на интермедијарном интензитету шума. У случају осцилаторних система у близини бифуркације, релативно недавно уочен је феномен инверзне стохастичке резонанце, где фреквенција осцилација пертурбованих шумом има минимум на интермедијарном интензитету шума. Експериментално је потврђено да овај феномен игра значајну улогу у неуронским системима, укључујући редуковање фреквенције опаљивања у одсуству неуромодулатора, сузбијање патолошки дуге краткорочне меморије, изазивање и супресију тоничног опаљивања као и оптимизацију преноса информација.

У светлу наведеног, планирано је да најважнији допринос Ивине докторске дисертације буде анализа карактеристика ексциtabilног понашања интерагујућих система, за разлику од класичног концепта ексциtabilности који се односи на појединачне јединице. Посебно, рад у оквиру тезе тицаће се три групе емергентних феномена. Прва линија истраживања се односи на феномен макроскопске ексциtabilности, сценарија у којем се популација ексциtabilних јединица и сама понаша као ексциtabilни елемент. На примеру популације спрегнутих стохастичких неуронских мапа, развојем *mean-field* модела заснованог на гаусијанској апроксимацији, анализирани су карактеристике режима макроскопске ексциtabilности, као и других режима колективне динамике. Показано је да постоји висок степен квалитативне и квантитативне усаглашености између предвиђања *mean-field* модела и динамике реалног система у погледу карактеризације макроскопске ексциtabilности, стохастичких бифуркација, кривих фазног одговора макроскопских варијабли на пертурбацију, као и статистичких особина временских серија. У склопу друге линије истраживања, која се односи на мотиве адаптивно спрегнутих ексциtabilних јединица, испитан је стохастички процес *switching* динамике. *Switching* динамика подразумева споре стохастичке флукуације између метастабилних стања изведених из коегзистентних атрактора одговарајућег детерминистичког система, или флукуације између осцилаторних мода изазваних шумом. Откривене су две генеричке форме *switching* динамике, које зависе од брзине адаптације, и чија феноменологија је објашњена проучавањем *layer* проблема и *reduced* проблема у оквиру *slow-fast* анализе. Трећа линија истраживања подразумева испитивање резонантних феномена на мотивима спрегнутих

ексцитабилних система. Досадашњи резултати, добијени на парадигматском моделу где је локална динамика представљена активним ротатором, открили су два нова генеричка сценарија за феномен инверзне стохастичке резонанце.

Поред наведеног испитивања емергентних феномена у спрегнутим ексцитабилним системима, Ива Бачић се у току докторских студија бавила и процесом уређивања кинетичког Изинговог (Глауберовог) модела на комплексним мрежама, као и проучавањем структуре неуређених конфигурација. Разматрани су случајеви регуларне топологије повезаности, мрежа са случајном и *small-world* топологијом добијене преповезивањем регуларне решетке, као и двослојних мрежа с различитом структуром повезаности између слојева. Експлицитно је показано да *small-world* топологија у термодинамичком лимесу онемогућава уређивање, при чему се неуређене конфигурације састоје од два домена, који одговарају мулти-кластер структурама на почетној регуларној решетки.

Списак публикација Иве Бачић

Радови у врхунским међународним часописима (категирија M21):

1. **I. Ваћић**, V. Klinshov, V. Nekorkin, M. Perc, and I. Franović,
Inverse stochastic resonance in a system of excitable active rotators with adaptive coupling,
EPL **124**, 40004 (2018) [ISSN=0295-5075, IF(2015)=1.963]
2. I. Franović, O. V. Maslennikov, **I. Ваћић**, and V. I. Nekorkin,
Mean-field dynamics of a population of stochastic map neurons,
Phys. Rev. E **96**, 012226 (2017) [ISSN: 1539-3755, IF(2016)=2.366]
3. **I. Ваћић**, I. Franović, and M. Perc,
Disordered Configurations of the Glauber Model in Two-dimensional Networks,
EPL **120**, 68001 (2017) [ISSN=0295-5075, IF(2015)=1.963]

Радови у врхунским међународним часописима (категирија M22):

1. **I. Ваћић**, S. Yanchuk, M. Wolfrum, and I. Franović,
Noise-induced switching in two adaptively coupled excitable systems,
Eur. Phys. J. - Spec. Top. **227**, 1077 (2018) [ISSN=1951-6355, IF(2017)=1.947]

Саопштења са међународног скупа штампана у изводу (M34):

1. **I. Ваћић**, V. Klinshov, V. Nekorkin, M. Perc, and I. Franović, Inverse stochastic resonance in a system of excitable active rotators with adaptive coupling, WIAS Workshop „Dynamics of Coupled Oscillator Systems“, 19 - 21 November 2018, Berlin, Germany
2. **I. Ваћић**, M. Lj. Ranković, F. Canon, V. Cerovski, C. Nicolas, A. Giuliani, and A. R. Milosavljević, Gas-phase X-ray action spectroscopy of protonated nanosolvated substance P peptide around O K-edge, COST XLIC WG2 Expert Meeting on Biomolecules, 27-30 April 2015, Fruška Gora, Serbia

Mean-field dynamics of a population of stochastic map neuronsIgor Franović,^{1,*} Oleg V. Maslennikov,^{2,†} Iva Bačić,¹ and Vladimir I. Nekorkin²¹*Scientific Computing Laboratory, Center for the Study of Complex Systems, Institute of Physics Belgrade, University of Belgrade, Pregrevica 118, 11080 Belgrade, Serbia*²*Institute of Applied Physics of the Russian Academy of Sciences, 46 Ulyanov Street, 603950 Nizhny Novgorod, Russia*

(Received 6 March 2017; published 27 July 2017)

We analyze the emergent regimes and the stimulus-response relationship of a population of noisy map neurons by means of a mean-field model, derived within the framework of cumulant approach complemented by the Gaussian closure hypothesis. It is demonstrated that the mean-field model can qualitatively account for stability and bifurcations of the exact system, capturing all the generic forms of collective behavior, including macroscopic excitability, subthreshold oscillations, periodic or chaotic spiking, and chaotic bursting dynamics. Apart from qualitative analogies, we find a substantial quantitative agreement between the exact and the approximate system, as reflected in matching of the parameter domains admitting the different dynamical regimes, as well as the characteristic properties of the associated time series. The effective model is further shown to reproduce with sufficient accuracy the phase response curves of the exact system and the assembly's response to external stimulation of finite amplitude and duration.

DOI: [10.1103/PhysRevE.96.012226](https://doi.org/10.1103/PhysRevE.96.012226)**I. INTRODUCTION**

Gaining a comprehensive understanding of the emergent dynamics of neuronal populations and their interactions is a topical issue in neuroscience [1,2]. The acquired neurobiological data corroborate that the operational tasks at different levels of the brain's multiscale hierarchical organization are distributed across anatomically segregated, but functionally integrated, moduli [3–5]. Within theoretical studies, substantial attention have received the phenomena unfolding on the intermediate (mesoscopic) scale [6], whereby the considered models are supposed to reflect the behavior of assemblies comprising microcolumns or cortical columns [7–9]. The mesoscopic dynamics typically consists of oscillations of different frequencies and amplitudes, which may be interspersed by episodes of chaotic or pseudo-chaotic irregular behavior [7]. This can further be modulated via interplay with activity generated at other scales, primarily the stochastic fluctuations from the microscopic level and the slow rhythms derived from the macroscopic structures.

Conceptually, the given phenomena are often addressed by invoking a paradigm where each population exhibiting a collective mode is regarded as a large-scale oscillator, such that the assembly's response to external stimuli, noise, or collective oscillations from afferent populations may be examined using the methods of nonlinear dynamics [10]. The ensuing models of collective motion are developed using different forms of mean-field (MF) approximation, which mainly apply the bottom-up strategy [11] to build reduced and analytically tractable description of population behavior starting from the high-dimensional system of (stochastic) differential equations for the local neuron dynamics. An additional point that makes the mesoscopic circuits particularly suitable for the MF treatment is that the often used assumption on assembly homogeneity approximately holds at this scale

[12]. In terms of fashion by which the population dynamics is statistically characterized, one may classify the effective systems into neural mass or probability density models [8,13]. The former rely on the large coherence approximation and yield the mean-rate dynamics [14], whereas the latter involve the diffusion approximation, providing for the evolution of the assembly-averaged dynamics and the corresponding variance [15,16]. The MF approach and its generalization to spatially extended systems have become a standard tool for analyzing diverse problems in neuroscience and other fields [17–23].

Nevertheless, one should emphasize that the MF analysis has so far exclusively been applied to the class of continuous-time systems, while the effective models for assemblies of coupled maps have been lacking. In particular, the collective motion of spiking or bursting neurons influenced by noise has been extensively studied using different models of coupled discrete systems, such as Rulkov [24–31] or Izhikevich neuron maps [32,33], but this has not been complemented by an appropriate MF theory. The latter has likely been the consequence of inability to implement the Fokker-Planck formalism to discrete-time systems. In the present paper, we obtain for the first time the MF theory for a population of coupled stochastic neuronal maps. The derivation relies on Gaussian approximation, which is introduced within the framework of Gaussian closure hypothesis [34–40].

We apply the MF approach to systematically analyze the emergent behavior and the stimulus-response relationship of a population of stochastic map neurons, where the local dynamics can exhibit a variety of regimes, including excitability, subthreshold oscillations, regular and chaotic spiking or bursting, as well as mixed spiking-bursting oscillations [41–44]. The particular set of issues we address consists in establishing whether and how the MF model can be used to (i) qualitatively analyze the network stability and bifurcations of the exact system associated to emergence of generic collective regimes; (ii) provide adequate quantitative predictions in terms of bifurcation thresholds, and the average interspike intervals or bursting cycles of the exact system; as well as (iii) accurately anticipate the population's response

*franovic@ipb.ac.rs

†olmaov@ipfran.ru

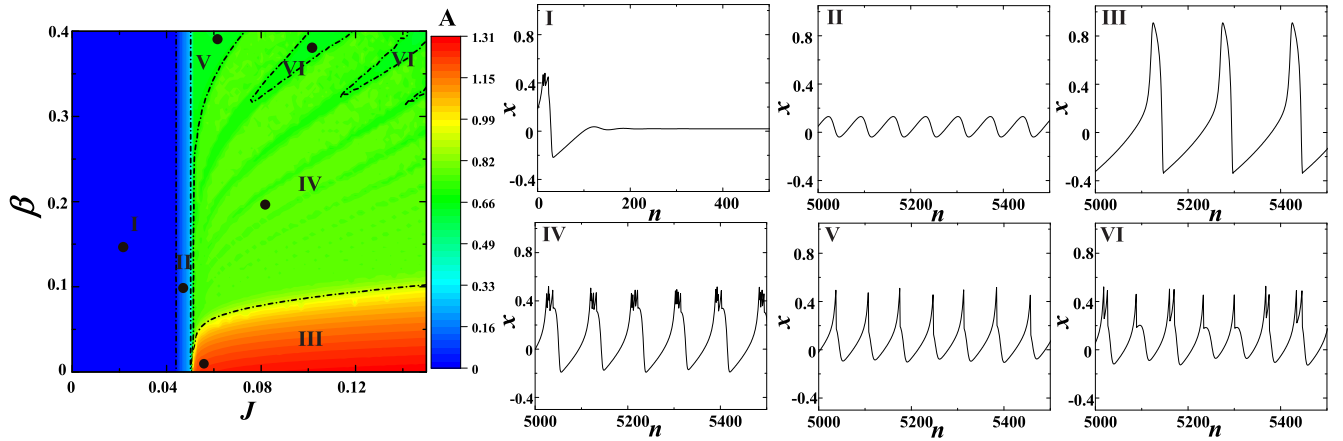


FIG. 1. Dynamical regimes exhibited by model (1). The heat map refers to variation of the amplitude of oscillations A of the x time series in the J - β plane. The wave forms shown in subfigures I–VI illustrate the different forms of neuron’s behavior, including excitability (I), subthreshold oscillations (II), regular spiking (III), chaotic bursting (IV), chaotic spiking (V), as well as the mixed spike-burst activity (VI). The dots in the heat map indicate the particular (J, β) values where the representative wave forms are obtained.

to different forms of external stimuli. Within this context, it will be examined whether the effective model is capable of reproducing the properties of noise-activated, noise-induced, and noise-perturbed modes of collective behavior.

The paper is organized as follows. In Sec. II, we make an overview of the local map dynamics and introduce the population model. Section III outlines the ingredients most relevant for the derivation of the MF system, with the remaining technical details left for the Appendix. In Sec. IV, the qualitative and quantitative agreement between the dynamics of the exact and the MF model is illustrated by the appropriate bifurcation diagrams, as well as by comparing the characteristic features of the associated regimes. Section V concerns the assembly’s stimulus-response relationship, first investigating the analogy between the respective phase-response curves (PRCs) of the exact system and the effective model in spiking and bursting regimes and then considering the extent to which the MF model reproduces the population’s response to rectangular pulses of finite amplitude and duration. In Sec. VI, we provide a summary of our main results.

II. MAP NEURON DYNAMICS AND THE POPULATION MODEL

The dynamics of an isolated neuron conforms to a map model first introduced in Refs. [45,46], which is given by

$$\begin{aligned} x_{n+1} &= x_n + G(x_n) - \beta H(x_n - d) - y_n, \\ y_{n+1} &= y_n + \epsilon(x_n - J), \end{aligned} \quad (1)$$

where n denotes the iteration step. The variable x_n qualitatively accounts for the membrane potential, whereas the recovery variable y_n , whose rate of change is set by a small parameter $\epsilon = 10^{-2}$, mimics the behavior of ion-gating channels. The parameters a , β , and d modify the profile of the ensuing oscillations, while J crucially influences the neural excitability, viz. the transitions from silence to active regimes.

The x_n evolution features two nonlinear terms, one being a FitzHugh-Nagumo-like cubic nonlinearity

$G(x_n) = x_n(x_n - a)(1 - x_n)$, which is complemented by a discontinuity term $-\beta H(x_n - d)$, where H stands for the Heaviside step function. The parameters $a = 0.1$ and $d = 0.45$ are kept fixed throughout the paper. The impact of discontinuity consists in making the fast subsystem [Eq. (1) with $\epsilon = 0$] a Lorenz-type map within certain parameter domains [46,47], which endows the model with the ability to generate chaotic spike or burst oscillations, otherwise lacking in the FitzHugh-Nagumo type of systems.

Under variation of J and β , the map (1) may reproduce a rich repertoire of generic regimes displayed by the real neurons, as demonstrated in Fig. 1. In particular, the main frame shows amplitudes of the corresponding x time series for the given (J, β) , while the remaining subfigures illustrate the characteristic wave forms pertaining to excitable regime (region I), subthreshold oscillations II, regular (III) or chaotic spiking (I), chaotic bursting (V), as well as the mixed chaotic spike-burst activity (VI). Some of the indicated boundaries, such as those involving domains IV, V, and VI should be understood as tentative, since the associated transitions are smooth and therefore difficult to discern.

The detailed phase plane analysis concerning the relevant unstable invariant curves and the mechanisms underlying transitions between the different dynamical regimes can be found in Ref. [48]. Here we briefly mention that under increasing J , the equilibrium loses stability via the Neimark-Sacker bifurcation, which gives rise to subthreshold oscillations. Note that the latter may be considered an excitable state, in the sense that a strong-enough perturbation can elicit genuine spike, though the phase point does not relax to the equilibrium but rather to a closed invariant curve.

Adopting model (1) for local dynamics, we focus on an assembly of N stochastic neurons coupled in the all-to-all fashion via electrical synapses (diffusive couplings). Each neuron receives input from the units within the assembly and is further influenced by synaptic noise from the embedding environment. Note that it is quite common in two-dimensional neuron models with sharp separation of characteristic time scales to interpret the stochastic perturbation acting on the fast

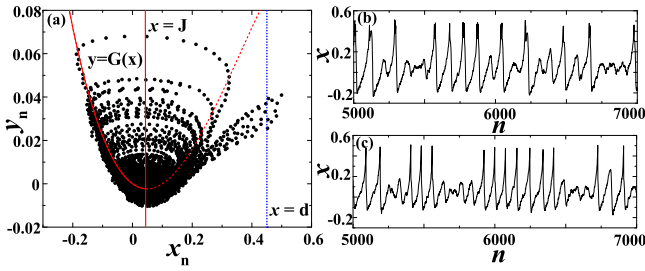


FIG. 2. Impact of noise on a single map neuron in the excitable regime. (a) The mechanism behind noise-induced spiking. The data are obtained for $J = 0.046$, $\beta = 0.4$, $\sigma = 0.005$. The equilibrium is deterministically stable given that the line $x = J$ intersects the invariant curve $y = G(x)$ below the curve's minimum. (b) The x_n series corresponding to noise-induced bursting ($J = 0.042$, $\beta = 0.2$, $\sigma = 0.008$), whereas (c) demonstrates stochastic spiking superimposed on subthreshold oscillations ($J = 0.048$, $\beta = 0.4$, $\sigma = 0.008$).

(slow) time scale as synaptic (intrinsic) noise [49–51]. The population activity is then described by the following system:

$$\begin{aligned} x_{i,n+1} &= x_{i,n} + G(x_{i,n}) - \beta H(x_{i,n} - d) - y_{i,n} + I_{i,n}^{\text{syn}}, \\ y_{i,n+1} &= y_{i,n} + \epsilon(x_{i,n} - J), \end{aligned} \quad (2)$$

$$I_{i,n}^{\text{syn}} = I_{i,n}^{\text{coup}} + I_{i,n}^{\text{rand}} = \frac{c}{N} \sum_{j=1, j \neq i}^N (x_{j,n} - x_{i,n}) + \sigma \xi_{i,n},$$

where i specifies the particular neuron. The synaptic currents $I_{i,n}^{\text{syn}}$ comprise two types of terms. The diffusive couplings $I_{i,n}^{\text{coup}}$ are characterized by the strength c , which is assumed to be uniform over the network and is set to $c = 1$ in the remainder of the paper. The random inputs $I_{i,n}^{\text{rand}}$ involve uncorrelated white noise [$E[\xi_{i,n}] = 0$, $E[\xi_{i,n}\xi_{j,n'}] = \delta_{ij}\delta(n - n')$] of intensity σ .

Confined to a single unit, the stochastic component may influence its dynamics either by perturbing the deterministic oscillatory regimes or by inducing oscillations in the excitable regime, cf. Fig. 2(b). The onset of noise-induced spiking or bursting within the parameter domain where the fixed point is deterministically stable (domain I in Fig. 1) corresponds to a phenomenon of stochastic bifurcation [39,52–55]. The latter are typically described phenomenologically, in a sense that certain time-averaged quantities, such as the asymptotic probability distributions of relevant variables or the associated power spectra, exhibit a qualitative change under variation of noise intensity. For instance, in continuous-time systems, it has been shown that the stochastic Hopf bifurcation from a stochastically stable fixed point to a stochastically stable limit cycle is accompanied by the loss of Gaussian property for the asymptotic distributions of the appropriate variables [56]. At variance with standard deterministic bifurcations, where one clearly observes a critical value of the control parameter, the change of system's behavior in noise-induced transitions is gradual [39]. Note that noise can also play an important part in the (J, β) region II where the deterministic map shows subthreshold oscillations. Here noise can give rise to a form of dynamics reminiscent of mixed-mode oscillations, cf. Fig. 2(c).

So far, models similar to (2) have been applied to address a number of problems associated to collective phenomena in

networks of coupled neurons, including synchronization of electrically coupled units with spike-burst activity [57,58], pattern formation in complex networks with modular architecture [41,42,59], transient cluster activity in evolving dynamical networks [44], as well as the basin stability of synchronization regimes in small-world networks [43]. Within this paper, the collective motion will be described in terms of the global variables $X_n = \frac{1}{N} \sum_{i=1}^N x_{i,n}$ and $Y_n = \frac{1}{N} \sum_{i=1}^N y_{i,n}$.

III. DERIVATION OF THE MEAN-FIELD MODEL

Considering a MF approximation, our main goal lies in deriving a reduced low-dimensional deterministic set of nonlinear difference equations whose dynamics is qualitatively analogous to the collective motion of the original system (2) composed of $2N$ coupled stochastic maps. In particular, the MF model should be able to generate all the regimes exhibited by the exact system, qualitatively reproducing the bifurcations that the latter undergoes. Also, applying the effective model, one should be capable of inferring with sufficient accuracy the parameter domains which admit the different collective states of the exact system, with the corresponding time series exhibiting similar characteristic quantitative features. Regarding the explicit effects of noise, the MF model is expected to account for the onset or suppression of different types of collective modes associated to macroscopic spiking or bursting activity, which are mediated by synchronization or desynchronization of individual neuron dynamics, respectively. The synchronization processes may be influenced by noise in a variety of ways, including the scenarios where noise acts as a perturbation to mainly deterministic (and chaotic) local oscillations, or the ones where noise plays a facilitatory role, in the sense that the collective mode emerges via synchronization of noise-induced local dynamics.

Given that we consider a system of discrete-time equations, one cannot adopt the usual method of deriving the MF model via Fokker-Planck formalism [40]. Nevertheless, an analytically tractable MF model may still be built by focusing on the evolution of cumulants [34–36,39], whereby the full density of states is factorized into a series of marginal densities. The advantage of such an approach is that the simplifying approximations aimed at truncating the underlying cumulant series can be introduced in a controlled fashion. Such approximations, stated in a form of closure hypothesis [34], are required due to nonlinearity of the original system, which causes the dynamics of cumulants of the given order to be coupled to those of the higher order.

In our case, the derivation of the effective model incorporates an explicit Gaussian closure hypothesis [34–36,39], by which all the cumulants above second order are assumed to vanish. The collective dynamics is then described by a set of five variables (the first- and second-order cumulants), including

- (i) the means, given by $m_{x,n} = \lim_{N \rightarrow \infty} \frac{1}{N} \sum_{i=1}^N x_{i,n} \equiv \langle x_{i,n} \rangle$, $m_{y,n} = \lim_{N \rightarrow \infty} \frac{1}{N} \sum_{i=1}^N y_{i,n} \equiv \langle y_{i,n} \rangle$;
- (ii) the variances, defined as $S_{x,n} = \langle x_{i,n}^2 \rangle - \langle x_{i,n} \rangle^2 = \langle x_{i,n}^2 \rangle - m_{x,n}^2$ and $S_{y,n} = \langle y_{i,n}^2 \rangle - \langle y_{i,n} \rangle^2 = \langle y_{i,n}^2 \rangle - m_{y,n}^2$;
- (iii) the covariance $U_n = \langle x_{i,n} y_{i,n} \rangle - m_{x,n} m_{y,n}$.

The expressions for higher-order moments $\langle x_{i,n}^k \rangle$ in terms of the first- and second-order cumulants [60], such as

$$\begin{aligned} \langle x_i^3 \rangle &= m_x^3 + 3m_x S_x \\ \langle x_i^4 \rangle &= m_x^4 + 6m_x^2 S_x + 3S_x^2 \\ \langle x_i^2 y_i \rangle &= m_y S_x + m_y m_x^2 + 2m_x U \\ \langle x_i^3 y_i \rangle &= 3S_x U + 3S_x m_x m_y + 3m_x^2 U + m_y m_x^3 \\ \langle x_i^5 \rangle &= m_x^5 + 15m_x S_x^2 + 10m_x^3 S_x \\ \langle x_i^6 \rangle &= m_x^6 + 15S_x^3 + 15m_x^4 S_x + 45m_x^2 S_x^2, \end{aligned} \quad (3)$$

can be derived using the closure hypothesis.

The Gaussian approximation effectively amounts to an assumption that the relation

$$\lim_{N \rightarrow \infty} \frac{1}{N} \sum_{i=1}^N x_{i,n}^k \approx E[x_{i,n}^k], \quad (4)$$

holds, whereby E refers to expectation value obtained by averaging over an ensemble of different stochastic realizations. In other words, one supposes that the local variables are independent and are drawn from a normal distribution $\mathcal{N}(m_x, S_x)$. We do not know *a priori* whether such an assumption is fulfilled but can only judge on its validity by verifying the correctness of the predictions on the population dynamics provided by the MF model. Also note that the effective model concerns the assembly dynamics in the thermodynamic limit

$N \rightarrow \infty$. The stochastic terms in this case can be neglected, as one may show them to contribute to finite-size effects which scale as $1/N$. This means that the influence of noise in our MF model is felt only via the noise intensity, which assumes the role of an additional bifurcation parameter.

Let us illustrate the main technical points required for the derivation of the MF model. Our focus will lie with a couple of relevant examples, whereas the remaining details are provided in the Appendix. We begin by considering the dynamics of m_x , which is given by

$$m_{x,n+1} = m_{x,n} - m_{y,n} + \langle G(x_{i,n}) \rangle - \beta \langle H(x_{j,n} - d) \rangle. \quad (5)$$

It is easy to see that there is no contribution from the coupling term. As far as the third term on the right-hand side of Eq. (5) is concerned, using Eq. (3), one arrives at

$$\begin{aligned} \langle G(x_i) \rangle &= \langle -x_i^3 + (1+a)x_i^2 - ax_i \rangle \\ &= G(m_x) + S_x(1+a-3m_x). \end{aligned} \quad (6)$$

In the last expression, we have dropped the time index for simplicity and have introduced the shorthand notation $G(m_x) \equiv -m_x^3 + (1+a)(m_x^2 + S_x)$.

The key problem is how to treat the final term in the right-hand side of Eq. (5). Our approach consists in replacing the assembly average by the expectation value ($\langle H(x_i - d) \rangle \approx E[H(x_i - d)]$), obtained by assuming that the local variables at an arbitrary time moment are normally distributed according to $P(x_i) \sim \mathcal{N}(m_x, S_x)$. The expectation may then be evaluated as

$$\begin{aligned} E[-\beta \langle H(x_i - d) \rangle] &= \int dx_1 \int dx_2 \dots \int dx_N \left(-\frac{\beta}{N} \sum_i H(x_i - d) \right) p(x_1, x_2, \dots, x_N) \\ &= -\beta \int_{-\infty}^{\infty} dx_1 H(x_1 - d) p(x_1) = -\beta \int_d^{\infty} \frac{1}{\sqrt{2\pi S_x}} e^{-\frac{(x_1 - m_x)^2}{2S_x}} = -\frac{\beta}{2} \left(1 - \text{Erf} \left[\frac{d - m_x}{\sqrt{2S_x}} \right] \right), \end{aligned} \quad (7)$$

with the error function $\text{Erf}(x) = \frac{2}{\sqrt{\pi}} \int_0^x e^{-t^2} dt$. In the above calculation, we have explicitly used the assumption on the independence of distributions of local variables at any given moment of time.

In a similar fashion, one may consider the S_x dynamics, which constitutes the most demanding part of the derivation. In particular, proceeding from the S_x definition, we obtain

$$\begin{aligned} S_{x,n+1} &= \langle x_{i,n+1}^2 \rangle - \langle x_{i,n+1} \rangle^2 \\ &= \langle [(1-c)x_{i,n} + G(x_{i,n}) - \beta H(x_{i,n} - d) - y_{i,n} + \xi_{i,n} + cm_{x,n}]^2 \rangle - [m_{x,n} - m_{y,n} + G(m_{x,n}) + S_{x,n}(1+a-3m_{x,n}) \\ &\quad - \beta \langle H(x_{i,n} - d) \rangle]^2. \end{aligned} \quad (8)$$

As an illustration, let us evaluate one of the terms containing an average over the threshold function:

$$\begin{aligned} -2\beta E[\langle G(x_i) H(x_i - d) \rangle] &= -2\beta \left[\int dx_1 G(x_1) H(x_1 - d) p(x_1) - \int dx_1 H(x_1 - d) p(x_1) [G(m_x) + S_x(1+a-3m_x)] \right] \\ &\approx -2\beta \left[\int dx_1 [G(m_x) + G'(m_x)(x_1 - m_x) + \frac{1}{2} G''(m_x)(x_1 - m_x)^2] H(x_1 - d) p(x_1) \right. \\ &\quad \left. - \int dx_1 H(x_1 - d) p(x_1) [G(m_x) + S_x(1+a-3m_x)] \right] = \dots \\ &= -2\beta [(1+a)(m_x + d) - a - 3m_x d] \sqrt{\frac{S_x}{2\pi}} \exp \left[-\frac{(d - m_x)^2}{2S_x} \right]. \end{aligned} \quad (9)$$

Again, the time indexes have been suppressed to simplify the notation.

Leaving the remaining elements of the derivation for the Appendix, we now state the final equations of the MF model in the thermodynamic limit

$$\begin{aligned}
 m_{x,n+1} &= m_{x,n} - m_{y,n} + G(m_{x,n}) + S_{x,n}(1 + a - 3m_{x,n}) - \frac{\beta}{2} \left(1 - \operatorname{Erf} \left[\frac{d - m_{x,n}}{\sqrt{2S_{x,n}}} \right] \right) \\
 m_{y,n+1} &= m_{y,n} + \epsilon(m_{x,n} - J) \\
 S_{x,n+1} &= (1 - c)^2 S_{x,n} + S_{y,n} + \sigma^2 - 2(1 - c)U_n + S_{x,n}(-3m_{x,n}^2 + 2(1 + a)m_{x,n} - a)^2 \\
 &\quad - 2(1 - c)(3m_{x,n}^2 S_{x,n} + 3S_{x,n}^2 - 2(1 + a)m_{x,n} S_{x,n} + aS_{x,n}) + 2(3S_{x,n}U_n + 3m_{x,n}^2 U_n - 2(1 + a)m_{x,n} U_n) \\
 &\quad - 2\beta[(1 + a)(m_{x,n} + d) - a - 3dm_{x,n}] \sqrt{\frac{S_{x,n}}{2\pi}} \exp \left[-\frac{(d - m_{x,n})^2}{2S_{x,n}} \right] - 2\beta(1 - c) \sqrt{\frac{S_{x,n}}{2\pi}} \exp \left[-\frac{(d - m_{x,n})^2}{2S_{x,n}} \right] \\
 &\quad + S_{x,n}^2 [36m_{x,n}^2 - 24(1 + a)m_{x,n} + 2(1 + a)^2 + 6a] + 15S_{x,n}^3 \\
 S_{y,n+1} &= S_{y,n} + \epsilon^2 S_{x,n} + 2\epsilon U_n \\
 U_{n+1} &= U_n - (a + c + \epsilon)U_n + \epsilon(1 - c - a)S_{x,n} - S_{y,n} - (U_n + \epsilon S_{x,n})[3S_{x,n} + 3m_{x,n}^2 - 2(1 + a)m_{x,n}] \\
 &\quad - \beta\epsilon \sqrt{\frac{S_{x,n}}{2\pi}} \exp \left[-\frac{(d - m_{x,n})^2}{2S_{x,n}} \right].
 \end{aligned} \tag{10}$$

IV. ANALYSIS OF STABILITY AND BIFURCATIONS

In this section, our goal is to demonstrate the qualitative and quantitative analogies between the dynamics of the exact system and the MF model. To this end, we first examine the succession of macroscopic regimes in the J - β parameter plane for σ fixed at an intermediate value $\sigma = 0.002$, see Fig. 3. As in case of a single unit, changing J is relevant for the system's excitability, viz. the transitions from silent to active regimes, while β influences the wave forms of the active states (spiking, bursting, or mixed spike-bursting activity). The assembly is found to exhibit the collective modes which qualitatively correspond to the dynamics of a single unit illustrated in plates

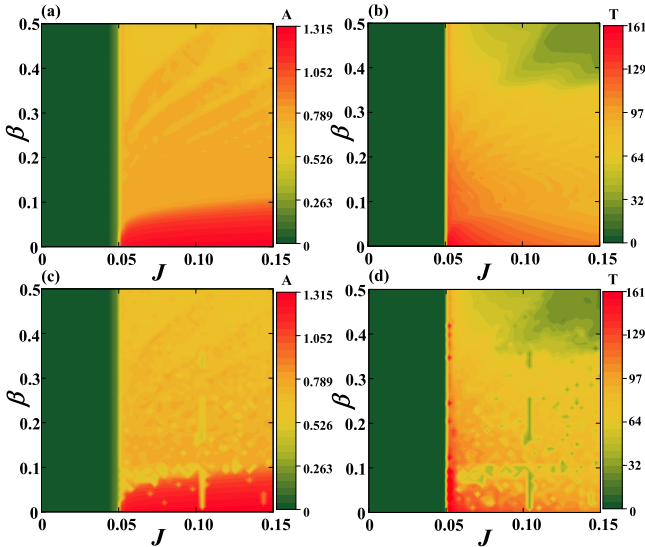


FIG. 3. Heat maps in (a) and (b) show the dependencies $A(J, \beta)$ and $T(J, \beta)$ obtained by stochastic averaging for a network of $N = 100$ neurons, respectively. Panels (c) and (d) illustrate the analogous results for the MF model. The noise intensity in all instances is $\sigma = 0.001$.

III and VI of Fig. 1. The heat maps in the left column of Fig. 3 provide a comparison between the oscillation amplitudes A of the global variable X (top row) and the MF variable m_x (bottom row) for the given (J, β) . The right column indicates how well are matched the average interspike interval (or the average bursting cycle) T of the exact system with the corresponding characteristics of the dynamics of the MF model (A1). In the given instances, exact system comprises an assembly of $N = 100$ neurons, having obtained A by averaging over a

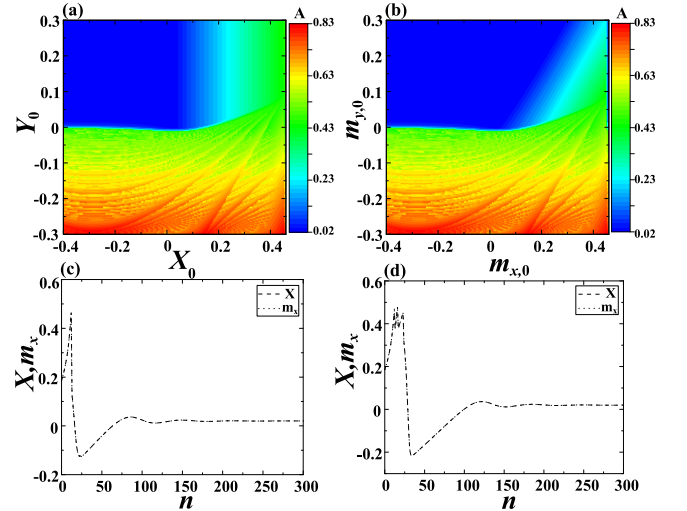


FIG. 4. Macroscopic excitability feature. In (a) and (b) are shown the maximum values of X and m_x reached within the time series of the exact and the MF system, starting from the analogous initial conditions (X_0, Y_0) and $(m_{x,0}, m_{y,0})$, respectively. The parameters are $J = 0.02, \beta = 0.4$. (c) Illustrates the case where a strong-enough perturbation elicits a single-spike response ($J = 0.02, \beta = 0.4$), whereas (d) corresponds to a bursting response made up of three spikes ($J = 0.02, \beta = 0.15$). In both instances, the time series of the MF model (dotted line) is indistinguishable from that of the exact system (dashed line).

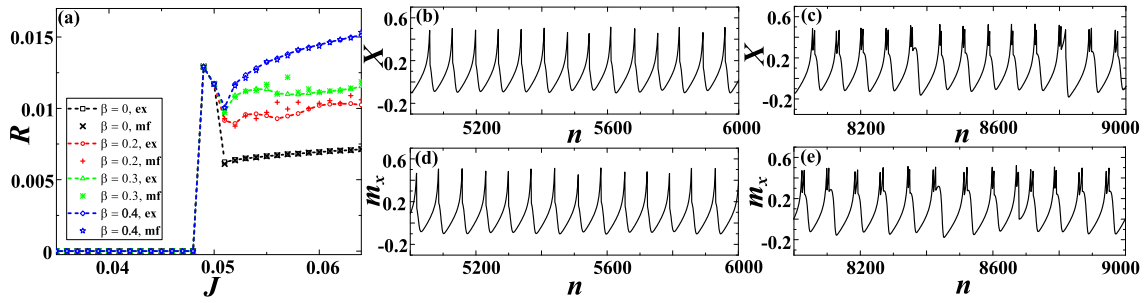


FIG. 5. (a) A family of $R(J)$ curves over β for a network of size $N = 100$ under fixed $\sigma = 0.001$. Superimposed are the results for the MF model, whereby the symbols \times , $+$, $*$, \star correspond to cases $\beta = 0, 0.2, 0.3$, and 0.4 , respectively. Panels (b) and (c) illustrate the X series associated to the spiking and the bursting collective modes. The considered network is made up of $N = 100$ neurons, with the parameters set to $J = 0.06$, $\beta = 0.4$, $\sigma = 0.001$ in (b), and $J = 0.08$, $\beta = 0.2$, $\sigma = 0.001$ in (c). In (d) and (e) are provided the m_x series obtained for parameters from (b) and (c).

sufficiently long time series, whereas T is determined by taking average over an ensemble of 20 different stochastic realizations. With regard to T , we have selected a convenient threshold $\theta = 0.2$, which allows a clear detection of individual spikes and enables one to unambiguously discern the initiation stage of bursts, as required for calculating the length of the bursting cycle.

Let us begin the analysis by focusing on the domain of J values where the exact system exhibits the stochastically stable equilibrium, while the MF model has a stable stationary state. The stochastic stability physically implies that fluctuations around the deterministic fixed point are typically of the order of noise, though some rare spikes may still be evoked. For J sufficiently close to the region admitting the sub-threshold oscillations, the population manifests macroscopic excitability. The term “macroscopic” here refers to a form of emergent assembly behavior rather than the characteristic spatial scale. To properly illustrate this feature, we have analyzed the assembly dynamics in the limit $\sigma = 0$, cf. Fig. 4. In particular, Figs. 4(a) and 4(b) show the maximum X and m_x values reached in the corresponding time series obtained for sets of different initial conditions (X_0, Y_0) and $(m_{x,0}, m_{y,0})$, respectively. The comparison between the two plots clearly corroborates that the boundary defining the domain of spiking response is appropriately anticipated by the MF model. An important remark is that for the given J , the assembly may exhibit different forms of macroscopic excitability, generating a single spike or a burst of spikes, as dependent on the value of β . This is demonstrated by the time series in Figs. 4(c) and 4(d). The former refers to a one-spike response in case of $\beta = 0.4$. For smaller β , one observes responses comprising two or more closely packed spikes, with Fig. 4(d) illustrating a three-spike burst encountered for $\beta = 0.25$. Note that the time series of the full system and the MF model are exactly matched in the limit $\sigma = 0$.

Next we address the noise-influenced transitions from silence to active regimes observed under increasing J . To do so, in Fig. 5(a) we have plotted the change of the firing (spiking or bursting) frequency R for an assembly consisting of $N = 100$ neurons. The average frequency is determined by considering an ensemble of 20 different stochastic realizations, having σ fixed to the moderate value from Fig. 4. The results from simulations of the full system (2) are compared against

the data obtained for the MF model. In this context, two points should be stressed. First, for moderate σ , note that the firing frequencies of the MF model lie in close agreement to those of the exact system. As a second point, one finds that such quantitative agreement extends to different forms of collective behavior, viz. it holds for different types of transitions from silent to active regimes. As already indicated, the wave forms pertaining to the active states depend on β , such that the associated transitions are mediated by the distinct synchronization processes. For instance, at $\beta = 0$, synchronization involves time series of single units that conform to spiking activity of type III from Fig. 1, which are quite resilient to impact of noise. On the other hand, for $\beta = 0.3$ or $\beta = 0.4$, the individual units exhibit chaotic bursting or spiking activity, respectively, such that the underlying synchronization process may be more susceptible to stochastic effects. The typical X time series illustrating the different collective modes are compared to the corresponding m_x series in Figs. 5(b)–5(e). The top (bottom) row concerns the data for the exact system (MF model).

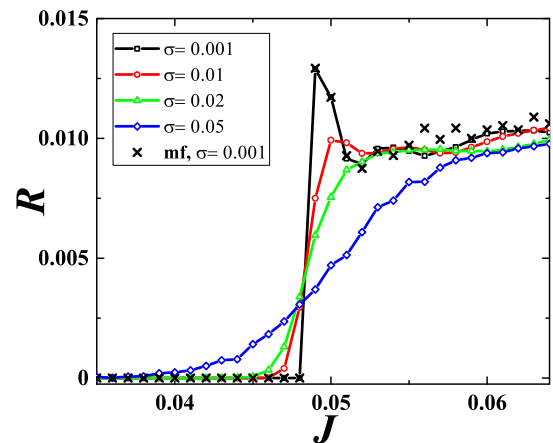


FIG. 6. Family of $R(J)$ curves over σ obtained for a network of $N = 100$ neurons under fixed $\beta = 0.2$. The different symbols correspond to cases $\sigma = 0.001$ (squares), $\sigma = 0.01$ (circles), $\sigma = 0.02$ (triangles), and $\sigma = 0.05$ (diamonds). The crosses connected by the dashed line highlight the $R(J)$ curve for the MF model at $\sigma = 0.001$.

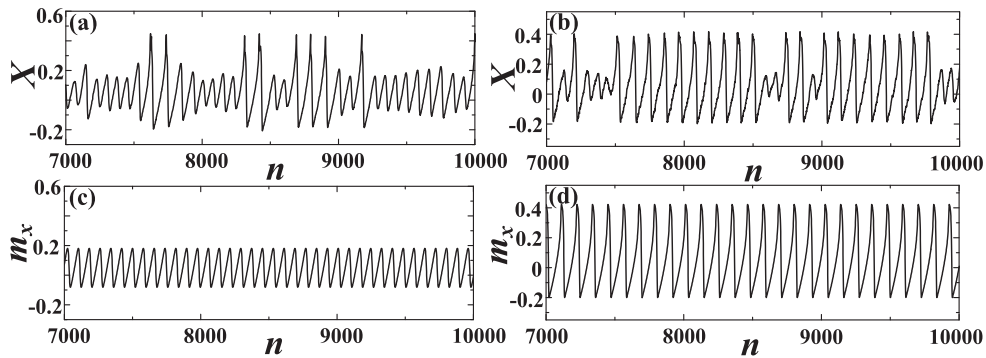


FIG. 7. Noise-induced phenomena within the J interval in vicinity of the deterministic threshold. X series in (a) shows the noise-induced spike-bursting activity on top of subthreshold oscillations ($J = 0.047$, $\beta = 0.2$, $\sigma = 0.02$). (b) Illustrates the “skipping” phenomenon where the stochastic effects occasionally suppress the large-amplitude oscillations of the X variable ($J = 0.058$, $\beta = 0.2$, $\sigma = 0.01$). In (c) and (d) are provided the m_x series corresponding to parameter sets from (a) and (b), respectively.

In order to investigate more closely the influence of noise for J interval in vicinity of the transition from silence to active regimes, we examine how the profiles of $R(J)$ curves change under increasing σ . The results shown in Fig. 6 refer to $\beta = 0.2$ and a population comprised of $N = 100$ neurons. As expected, the transition appears quite sharp for moderate noise $\sigma = 0.001$ but is considerably flattened for larger σ , e.g., $\sigma = 0.05$. The crosses indicate the firing frequencies predicted by the MF model for $\sigma = 0.001$.

For larger σ , the MF model fails to reproduce the behavior of the exact system in vicinity of threshold J , in the sense that it overestimates the maximal R value, as well as the actual critical J characterizing the transition. Viewed from another angle, one may infer that for sufficiently large σ and J below the threshold given by the MF model, the latter fails to capture the impact of synchronization processes taking place between the noise-induced oscillations of individual units. This especially refers to J interval where the spikes or bursts (depending on the given β) are superimposed on the background of subthreshold oscillations. An example of such a discrepancy between the behavior of the exact and the effective system is provided in Fig. 7, cf. Fig. 7(a) and Fig. 7(c). Also, for strong σ and J values above the transition, the firing frequencies anticipated by the effective model are typically higher than those of the exact system (not shown). Within this region, the stochastic effects suppress synchronization between the chaotic oscillations of single neurons, thereby reducing the corresponding R value. This is not accounted for with sufficient accuracy by the MF system. Note that such suppression of synchronization is reflected in the corresponding X series by the spike (burst) “skipping” mechanism, where the large-amplitude oscillations are occasionally replaced with subthreshold oscillations. For the associated J and σ values, such a phenomenon is absent in the dynamics of the effective model, cf. Fig. 7(b) and Fig. 7(d). In both of the scenarios illustrated in Fig. 7, the reason for the failure of MF model is that the Gaussian approximation breaks down due to large stochastic fluctuations.

The fashion in which the validity of the effective model’s predictions deteriorates with increasing σ is made more explicit in Fig. 8, which shows the $A(J, \sigma)$ and $T(J, \sigma)$ dependencies for the exact and the approximate system at

fixed $\beta = 0.4$. The considered size of the network is $N = 100$. Comparison between the respective A (left column) and T plots (right column) suggests that the range of σ values where the MF approximation applies is contingent on J . For instance, in the J region below the deterministic threshold, one may estimate this range by noting that the effective bifurcation diagram in Fig. 8(a) indicates that noise-induced macroscopic oscillations emerge for $\sigma \approx 0.003$. Since this point is not adequately represented by the effective model, cf. Fig. 8(c), one may state that the Gaussian approximation breaks down around $\sigma \approx 0.003$ within the given J region. Nevertheless, for J above the deterministic threshold, the validity of the MF model appears to depend rather strongly on particular J , with the σ values where the Gaussian approximation effectively fails spanning the range $\sigma \in (0.002, 0.006)$.

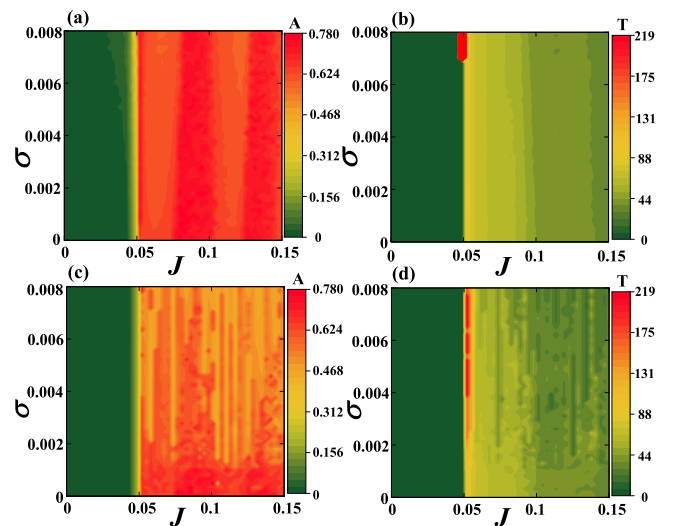


FIG. 8. Panels (a) and (b), respectively, refer to $A(J, \sigma)$ and $T(J, \sigma)$ dependencies for the network of $N = 100$ neurons under fixed $\beta = 0.4$. The results in (a) are obtained by averaging over a sufficiently long time series, whereas data in (b) derive from averaging over an ensemble of 20 different stochastic realizations. In (c) and (d) are provided the $A(J, \sigma)$ and $T(J, \sigma)$ dependencies determined by numerical simulations of the MF model.

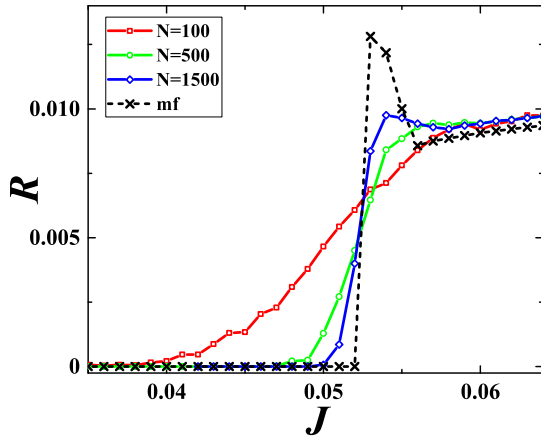


FIG. 9. $R(J)$ dependencies for increasing N under fixed $(\beta, \sigma) = (0.2, 0.05)$. The squares, circles, and diamonds correspond to cases $N = 100$, $N = 500$, and $N = 1500$, respectively. The results predicted by the MF model are indicated by crosses connected via dashed line.

So far, we have investigated the impact of noise by comparing the results for the network of size $N = 100$ to those obtained for the effective system. Nevertheless, within Sec. III, it has already been emphasized that the MF model, deterministic in character, refers to the system's behavior in the thermodynamic limit $N \rightarrow \infty$, whereas the explicitly stochastic terms could only be incorporated as finite-size effects. This makes it relevant to examine how the behavior of the exact system within the J domain around deterministic threshold changes for large and fixed σ under increasing N . To this end, we have plotted in Fig. 9 the $R(J)$ curves calculated for $N = 100$ (squares), $N = 500$ (circles), and $N = 1500$ (diamonds) at fixed $\beta = 0.2, \sigma = 0.05$. The curve for $N = 100$ evinces that the given σ value is quite large in a sense of being sufficient to induce collective oscillations within the excitable regime. Apart from the dependencies for the full system, we also show the $R(J)$ curve associated to the MF model (dashed line with crosses). An interesting point regarding the latter is that the J threshold for the emergence of the collective mode is shifted toward a larger value compared to the case $\sigma \approx 0.01$. While the given transition itself appears quite sharp, the curves corresponding to the exact system approach it with increasing N , both in terms of the J threshold and the R values above the transition. This corroborates that the (J, σ) domain where the Gaussian approximation behind the MF model fails expectedly reduces with the increasing system size.

V. RESPONSE TO EXTERNAL STIMULI

The aim of this section is to investigate the extent to which the MF model can be used to predict the stimulus-response relationship of an assembly exhibiting different macroscopic regimes, including the excitable state, as well as the spiking and bursting collective modes. Let us first focus on the two latter instances and examine the sensitivity of a population to an external pulse perturbation within the framework of phase resetting theory [61–64]. In order to compare the behavior of the exact system and the effective model, we determine

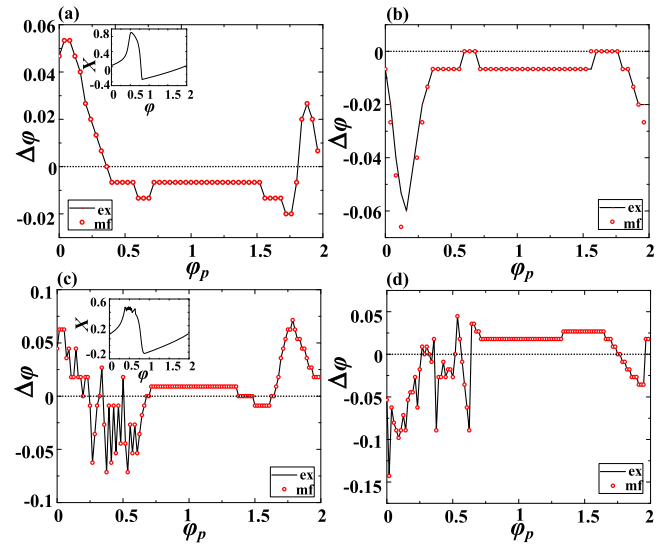


FIG. 10. Assembly phase resetting. Panels (a) and (b) show the PRCs for a population in spiking regime ($J = 0.055$, $\beta = 0$) under excitatory ($a = 0.008$) and inhibitory stimulation ($a = -0.008$), respectively. Results for the exact system ($N = 500$) are indicated by the solid line, whereas the data for the MF model are denoted by circles. The bottom row illustrates the PRCs for an assembly exhibiting macroscopic bursting ($J = 0.06$, $\beta = 0.1$), whereby (c) describes the effect of an excitatory ($a = 0.01$) and (d) of an inhibitory pulse perturbation ($a = -0.01$). The insets in (a) and (c) demonstrate how the phases are assigned to the points within the spiking and bursting cycles, respectively. Phase is expressed in units of π .

the corresponding PRCs, which describe the phase shift $\Delta\phi$, induced by the perturbation, in terms of the phase ϕ_p when the perturbation is applied. The considered stimulus has a form of a short pulse current $I_p = a_p H(n - n_i) H(n - n_f)$, whose magnitude a_p and width $\Delta = n_i - n_f$ are small compared to the amplitude and duration of the spiking (or bursting) cycle T_0 , respectively. In case of the exact system, the same pulse current is delivered to each neuron i , adding the term I_p to x_i dynamics, whereas in the effective model, stimulation is administered via the m_x variable. The phase ϕ_p is defined in reference to T_0 by $\phi_p = n_p / T_0$. The associated phase difference following the reset is calculated as $\Delta\phi = 1 - T_1 / T_0$, where T_1 denotes the duration of the perturbed spiking or bursting cycle.

The PRCs characterizing the assembly response in the spiking regime are provided in Fig. 10(a) and Fig. 10(b), whereby the former is obtained under the action of an excitatory ($a_p > 0$), and the latter under the influence of inhibitory stimulation ($a_p < 0$). We stress that, in both instances, the results derived from the effective model, denoted by circles, show excellent agreement with the data for the exact system (solid lines). In qualitative terms, one observes that excitatory stimulation may advance the phase of the spiking cycle if it arrives sufficiently close to the spike but still before the sharp rising stage. However, an excitatory perturbation acting during the spike or within the effective refractory period has a suppression effect, reflected in delaying of the next spike. In contrast to excitatory stimulation, the inhibitory pulse postpones the next firing time if it is introduced within the interval close to the rising stage of spike.

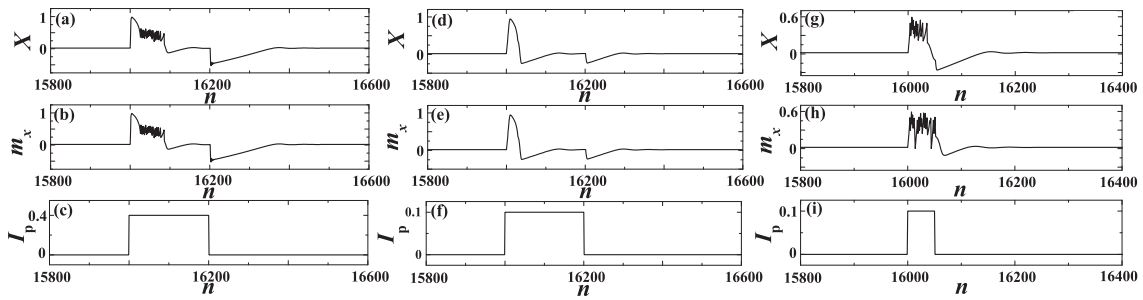


FIG. 11. Stimulus-response relationship in the excitable regime ($J = 0.02$). The top (middle) row refers to the response of the full system (MF model), whereas the bottom row shows the profile of the external stimulation. In panels (a)–(c), the system parameters are $\beta = 0.4$, $\sigma = 0$, while the perturbation is characterized by $a_p = 0.4$, $\Delta = 200$. Panels (d)–(f) concern the response of an assembly ($\beta = 0.1$, $\sigma = 0.001$) subjected to a rectangular pulse $a_p = 0.4$, $\Delta = 200$. Panels (g)–(i) illustrate the response of a population ($\beta = 0.4$, $\sigma = 0.001$) influenced by the external stimulation $a_p = 0.1$, $\Delta = 50$. The considered network is of size $N = 500$.

The PRCs determined for an assembly exhibiting collective bursting show qualitatively analogous effects to those described so far, see Fig. 10(c) and Fig. 10(d). This especially refers to impact of perturbation delivered sufficiently close to a moment of burst initiation. An apparent difference compared to Fig. 10(a) and Fig. 10(b) emerges during the bursting stage itself, where the associated PRCs expectedly exhibit strong fluctuations. Apart from that, one finds an interesting effect that both the excitatory and the inhibitory stimulation have a facilitatory role, i.e., cause phase advancement during the relaxation stage of the bursting cycle.

For a population in the excitable state, we consider scenarios where the system is influenced by a rectangular pulse perturbation of finite magnitude and duration, in a sense that the latter are comparable to corresponding features of typical spiking or bursting cycles. Note that the selected J value $J = 0.02$ lies sufficiently away from the interval admitting the subthreshold oscillations. Again, our objective is to determine whether the MF model correctly anticipates the response of the exact system, now in the presence of small to moderate noise. Some of the illustrative examples concerning the stimulus-response relationship under the finite perturbation are provided in Fig. 11. The top and the middle rows refer to X and corresponding m_x time series, respectively, while the bottom row shows the profile of the applied stimulus. We find that in the absence of noise or for sufficiently small σ , the effective model reproduces the evoked behavior of the full system quite accurately. This also refers to some highly complex forms of responses, as corroborated in Figs. 11(a)–11(c), which concern relatively large a_p and Δ . Under increasing σ , the ability of the MF model to predict the dynamics of the exact system gradually reduces but in a fashion that involves a nontrivial dependence on β . In particular, for smaller $\beta \approx 0.1$, which would facilitate macroscopic spiking mode for supercritical J , it turns out that the dynamics of the MF model lies in close agreement to the one of the exact system even for moderate noise $\sigma = 0.001$, cf. Figs. 11(d)–11(f). However, for higher β , such an analogy between the responses of the exact and the MF system is lost, see Figs. 11(g)–11(i). Naturally, the validity of the predictions given by the MF model deteriorates if the stimulation amplitude a_p and the duration Δ are large, especially in the presence of non-negligible noise.

VI. SUMMARY AND DISCUSSION

We have developed an MF approach in order to systematically analyze the emergent dynamics and the input-output relationship of a population of stochastic map neurons. The reduced low-dimensional model has been derived within the framework of Gaussian approximation, formally introduced in a form of a closure hypothesis. In physical terms, such an approximation suggests that the local variables at an arbitrary moment of time are independent and conform to a normal distribution centered about the assembly mean and characterized by the associated assembly variance. Validity of such an approximation cannot be established *a priori*, but has been systematically verified by numerically corroborating that the MF model reproduces the behavior of the exact system with sufficient accuracy.

In particular, we have first demonstrated that the effective model can qualitatively capture all the bifurcations of the exact system leading to the onset of different generic regimes of collective behavior. As far as the quantitative agreement is concerned, we have established substantial matching between the parameter domains admitting the respective dynamical regimes for the exact and the approximate system. Moreover, the typical features of the associated regimes, such as the average interspike interval or the average bursting cycle, exhibit analogous changes with parameter variation and in many parameter domains display numerically similar values.

An important issue has been to explicitly examine how the effects of noise are reflected in the behavior of the MF model. For the noise-perturbed activity, where the sufficiently small noise weakly influences the deterministic attractors of the system, the obtained results indicate that the Gaussian approximation holds. Nevertheless, the physical picture changes in case of noise-induced collective behavior. In particular, for different scenarios of stochastic bifurcations, typically corresponding to transitions from subthreshold oscillations, which involve generalized excitability feature, to spiking or bursting regimes, the exact system undergoes a gradual (smooth) change of collective dynamics, whereas the MF model exhibits a standard deterministic bifurcation with a sharp bifurcation threshold. In such instances, the collective variables of exact system manifest large fluctuations, which

explicitly violate the Gaussian approximation behind the effective model. Note that the loss of Gaussianity property for asymptotic distribution of relevant variables, which accompanies the described stochastic bifurcations, does not imply per se that our Gaussian approximation fails in the supercritical state. This point is evinced by the fact that the dynamics of the effective model shows qualitatively and quantitatively similar features to those of the exact system if the considered parameters lie sufficiently above the stochastic bifurcation. In fact, the Gaussian approximation applied in the derivation of the MF model breaks down only in vicinity of such transitions, where the finite-size effects neglected in Eq. (A1) become most prominent. We have numerically verified the prevalence of finite-size effects in these parameter domains, showing that the change of the appropriate order parameter, such as the spiking frequency, becomes sharper as the size of the neural assembly is increased. Nevertheless, the validity of Gaussian approximation is regained once the system is sufficiently above the bifurcation.

Apart from considering asymptotic dynamics, we have verified that the MF model is capable of capturing the stimulus-response features of the exact system. For short pulse-like perturbations, it has been found that the approximate system reproduces the PRCs of the exact system for both the spiking and bursting regimes of collective activity with high

accuracy. Substantial analogies have also been observed in case of macroscopic excitable regime for scenarios where the assembly is stimulated by rectangular pulse perturbations of finite amplitude and duration.

Having developed a viable MF approach, the present research has set the stage for a more systematic exploration of collective dynamics of assemblies of map neurons by analytical means. We believe that the introduced techniques can be successfully applied for treating the emergent behavior of populations in case of chemically and delay-coupled neurons [41]. Moreover, the method may likely be used to explore the effects of parameter inhomogeneity, as well as to study the impact of complex network topologies [41,43]. Our ultimate goal will be to extend the MF approach to account for collective behavior of interacting populations of map neurons [41,42].

ACKNOWLEDGMENTS

This work is supported by the Ministry of Education, Science and Technological Development of Republic of Serbia under Project No. 171017 and by the Russian Foundation for Basic Research under Project No. 15-02-04245. Numerical experiments are supported by the Russian Science Foundation under Project No. 14-12-01358.

APPENDIX

In the following, we provide the remaining details concerning the calculation of the S_x dynamics, which is the most complex part of the derivation of the effective model. Following some algebra, Eq. (9) can be transformed to

$$\begin{aligned} S_{x,n+1} = & (1-c)^2 S_{x,n} + S_{y,n} + \sigma^2 - 2(1-c)U_n + \underbrace{(\langle G(x_{i,n})^2 \rangle - \langle G(x_{i,n}) \rangle^2)}_{\text{Var}(G(x_{i,n}))} + 2(1-c)(\langle x_{i,n} G(x_{i,n}) \rangle - m_{x,n} \langle G(x_{i,n}) \rangle) \\ & - 2(\langle y_{i,n} G(x_{i,n}) \rangle - m_{y,n} \langle G(x_{i,n}) \rangle) - 2\beta(1-c)[\langle x_{i,n} H(x_{i,n}-d) \rangle - m_{x,n} \langle H(x_{i,n}-d) \rangle] - 2\beta(\langle G(x_{i,n}) H(x_{i,n}-d) \rangle \\ & - \langle G(x_{i,n}) \rangle \langle H(x_{i,n}-d) \rangle) + \beta^2 \underbrace{(\langle H(x_{i,n}-d)^2 \rangle - \langle H(x_{i,n}-d) \rangle^2)}_{\text{Var}(H(x_{i,n}-d))}. \end{aligned} \quad (\text{A1})$$

The partial results required for completing the calculation are given by

$$\begin{aligned} \langle x_i G(x_i) \rangle - m_x \langle G(x_i) \rangle &= G'(m_x) S_x - 3S_x^2 \\ \langle y_i G(x_i) \rangle - m_y \langle G(x_i) \rangle &= -3S_x U_{xy} - 3m_x^2 U_{xy} + 2(1+a)m_x U_{xy}, \end{aligned} \quad (\text{A2})$$

where $G'(m_x) \equiv -3m_x^2 + 2(1+a)m_x - a$. Note that the time indexes have been omitted for simplicity. After some tedious work, it may also be shown that the expression for variance $\text{Var}(G(x_i))$ reads

$$\text{Var}(G(x_i)) = G'^2(m_x) S_x + S_x^2 [36m_x^2 - 24(1+a)m_x + 2(1+a)^2 + 6a] + 15S_x^3. \quad (\text{A3})$$

Let us now explicitly calculate the terms containing the threshold function. First, we have

$$\begin{aligned} & -2\beta(1-c)[\langle x_i H(x_i-d) \rangle - \langle x_i \rangle \langle H(x_i-d) \rangle] \\ &= -2\beta(1-c) \left[\int dx_1 dx_2 \dots dx_N \frac{1}{N} \sum_i x_i H(x_i-d) p(x_1, \dots, x_N) - m_x \int dx_1 dx_2 \dots dx_N \frac{1}{N} \sum_i H(x_i-d) p(x_1, \dots, x_N) \right] = \dots \\ &= -2\beta(1-c) \left[\int dx_1 (x_1 - m_x) H(x_1-d) p(x_1) \right] = -2\beta(1-c) \sqrt{\frac{S_x}{2\pi}} \exp \left[-\frac{(d-m_x)^2}{2S_x} \right]. \end{aligned} \quad (\text{A4})$$

Note that the second term containing the threshold function has been evaluated in the main text, cf. Eq. (10).

Finally, let us address the term $\beta^2 \text{Var}[H(x_i - d)]$, which can be estimated by considering the associated expectation $\beta^2 \text{Var}[H(x_i - d)] \approx \beta^2 [\langle H(x_i - d)^2 \rangle - \langle H(x_i - d) \rangle^2]$. Applying the technique introduced in Sec. III, we obtain

$$\begin{aligned} E[\beta^2 H(x_i - d)^2] &= \beta^2 \int dx_1 \int dx_2 \dots \int dx_N \left[\frac{1}{N^2} \sum_i \sum_j H(x_i - d) H(x_j - d) \right] p(x_1, x_2, \dots, x_N) \\ &= \underbrace{\frac{\beta^2}{N^2} N \int dx_1 H(x_1 - d) p(x_1)}_{N \text{ cases where } i=j} + \underbrace{\frac{\beta^2}{N^2} N(N-1) \int dx_1 \int dx_2 H(x_1 - d) H(x_2 - d) p(x_1) p(x_2)}_{N(N-1) \text{ cases where } i \neq j} \\ &= \frac{\beta^2}{2N} \left[1 - \text{Erf} \left(\frac{d - m_x}{\sqrt{2S_x}} \right) \right] + \frac{\beta^2}{4N^2} N(N-1) \left[1 - \text{Erf} \left(\frac{d - m_x}{\sqrt{2S_x}} \right) \right]^2. \end{aligned} \quad (\text{A5})$$

Given that $\beta^2 \langle H(x_i - d) \rangle^2 = \frac{\beta^2}{4} [1 - \text{Erf}(\frac{d - m_x}{\sqrt{2S_x}})]^2$, one arrives at

$$\beta^2 \text{Var}[H(x_i - d)] = \frac{\beta^2}{4N} \left[1 - \text{Erf} \left(\frac{d - m_x}{\sqrt{2S_x}} \right) \right] \left[1 + \text{Erf} \left(\frac{d - m_x}{\sqrt{2S_x}} \right) \right]. \quad (\text{A6})$$

This shows that the variance of the threshold function ultimately contributes to a finite-size effect which can be neglected in the thermodynamic limit.

-
- [1] G. Buzsáki, *Rhythms of the Brain* (Oxford University Press, Oxford, 2009).
- [2] A. Destexhe and D. Contreras, *Science* **314**, 85 (2006).
- [3] C. Zhou, L. Zemanová, G. Zamora, C. C. Hilgetag, and J. Kurths, *Phys. Rev. Lett.* **97**, 238103 (2006).
- [4] E. Bullmore and O. Sporns, *Nat. Rev. Neurosci.* **10**, 186 (2009).
- [5] O. Sporns, D. Chialvo, M. Kaiser, and C. C. Hilgetag, *Trends Cogn. Sci.* **8**, 418 (2004).
- [6] W. J. Freeman, *Neurodynamics: An Exploration in Mesoscopic Brain Dynamics* (Springer-Verlag, London, 2000).
- [7] H. Liljenström, *Scholarpedia* **7**, 4601 (2012).
- [8] G. Deco, V. K. Jirsa, P. A. Robinson, M. Breakspear, and K. Friston, *PLoS Comput. Biol.* **4**, e1000092 (2008).
- [9] J. L. P. Velazquez and R. Wennberg, *Coordinated Activity in the Brain: Measurements and Relevance to Brain Function and Behavior* (Springer, New York, 2009).
- [10] Y. Baibolatov, M. Rosenblum, Z. Z. Zhanabaev, M. Kyzgarina, and A. Pikovsky, *Phys. Rev. E* **80**, 046211 (2009).
- [11] W. Gerstner, H. Sprekeler, and G. Deco, *Science* **338**, 60 (2012).
- [12] *Lectures in Supercomputational Neuroscience: Dynamics in Complex Brain Networks*, edited by P. beim Graben, C. Zhou, M. Thiel, and J. Kurths (Springer-Verlag, Berlin, 2008).
- [13] M. Breakspear, *Nat. Neurosci.* **20**, 340 (2017).
- [14] W. J. Freeman, *Mass Action in the Nervous System: Examination of the Neurophysiological Basis of Adaptive Behavior through the EEG* (Academic Press, London, 1975).
- [15] N. Fourcaud and N. Brunel, *Neural Comput.* **14**, 2057 (2002).
- [16] S. El Boustani, and A. Destexhe, *Neural Comput.* **21**, 46 (2009).
- [17] S. E. Folias and P. C. Bressloff, *Phys. Rev. Lett.* **95**, 208107 (2005).
- [18] S. E. Folias and P. C. Bressloff, *SIAM J. Appl. Math.* **65**, 2067 (2005).
- [19] C. R. Laing, W. C. Troy, B. Gutkin, and G. B. Ermentrout, *SIAM J. Appl. Math.* **63**, 62 (2002).
- [20] P. C. Bressloff, *Phys. Rev. E* **82**, 051903 (2010).
- [21] M. A. Buice and J. D. Cowan, *Phys. Rev. E* **75**, 051919 (2007).
- [22] N. Brunel and V. Hakim, *Neural Comput.* **11**, 1621 (1999).
- [23] H. Hasegawa, *Phys. Rev. E* **67**, 041903 (2003).
- [24] N. F. Rulkov, *Phys. Rev. E* **65**, 041922 (2002).
- [25] N. F. Rulkov, I. Timofeev, and M. Bazhenov, *J. Comput. Neurosci.* **17**, 203 (2004).
- [26] D. Q. Wei and X. S. Luo, *Europhys. Lett.* **78**, 68004 (2007).
- [27] Q. Y. Wang, Z. Duan, M. Perc, and G. Chen, *Europhys. Lett.* **83**, 50008 (2008).
- [28] C. A. S. Batista, A. M. Batista, J. A. C. de Pontes, R. L. Viana, and S. R. Lopes, *Phys. Rev. E* **76**, 016218 (2007).
- [29] B. Ibarz, J. M. Casado, and M. A. F. Sanjuán, *Phys. Rep.* **501**, 1 (2011).
- [30] I. Franović and V. Miljković, *Europhys. Lett.* **92**, 68007 (2010).
- [31] I. Franović and V. Miljković, *Commun. Nonlinear Sci. Numer. Simul.* **16**, 623 (2011).
- [32] E. M. Izhikevich, *Neural Comput.* **18**, 245 (2006).
- [33] E. M. Izhikevich and G. M. Edelman, *Proc. Natl. Acad. Sci. U.S.A.* **105**, 3593 (2008).
- [34] B. Lindner, J. Garcia-Ojalvo, A. Neiman, and L. Schimansky-Geier, *Phys. Rep.* **392**, 321 (2004).
- [35] I. Franović, K. Todorović, N. Vasović, and N. Burić, *Phys. Rev. E* **89**, 022926 (2014).
- [36] I. Franović, K. Todorović, N. Vasović, and N. Burić, *Phys. Rev. E* **87**, 012922 (2013).
- [37] I. Franović, K. Todorović, N. Vasović, and N. Burić, *Chaos* **22**, 033147 (2012).
- [38] V. Klinshov and I. Franović, *Phys. Rev. E* **92**, 062813 (2015).
- [39] M. A. Zaks, X. Sailer, L. Schimansky-Geier, and A. B. Neiman, *Chaos* **15**, 026117 (2005).
- [40] B. Sonnenschein, M. A. Zaks, A. B. Neiman, and L. Schimansky-Geier, *Eur. Phys. J. Special Topics* **222**, 2517 (2013).
- [41] O. V. Maslennikov and V. I. Nekorkin, *Phys. Rev. E* **90**, 012901 (2014).

- [42] O. V. Maslennikov, D. V. Kasatkin, N. F. Rulkov, and V. I. Nekorkin, *Phys. Rev. E* **88**, 042907 (2013).
- [43] O. V. Maslennikov, V. I. Nekorkin, and J. Kurths, *Phys. Rev. E* **92**, 042803 (2015).
- [44] O. V. Maslennikov and V. I. Nekorkin, *Commun. Nonlinear Sci. Numer. Simul.* **23**, 10 (2015).
- [45] V. I. Nekorkin and L. V. Vdovin, *Izv. Vyssh. Uchebn. Zaved. Prikladn. Nelinejn. Din.* **15**, 36 (2007).
- [46] M. Courbage, V. I. Nekorkin, and L. V. Vdovin, *Chaos* **17**, 043109 (2007).
- [47] O. V. Maslennikov and V. I. Nekorkin, *Chaos* **23**, 023129 (2013).
- [48] O. V. Maslennikov and V. I. Nekorkin, Map-based approach to problems of spiking neural network dynamics, in *Nonlinear Dynamics and Complexity*, edited by V. Afraimovich, A. C. J. Luo, and X. Fu (Springer International, Switzerland, 2014), pp. 143–161.
- [49] A. Destexhe and M. Rudolph-Lilith, *Neuronal Noise* (Springer, New York, 2012).
- [50] I. A. Khovanov, A. V. Polovinkin, D. G. Luchinsky, and P. V. E. McClintock, *Phys. Rev. E* **87**, 032116 (2013).
- [51] I. Franović, K. Todorović, M. Perc, N. Vasović, and N. Burić, *Phys. Rev. E* **92**, 062911 (2015).
- [52] L. Arnold, *Random Dynamical Systems* (Springer Verlag, Berlin, 1999).
- [53] J. A. Acebrón, A. R. Bulsara, and W.-J. Rappel, *Phys. Rev. E* **69**, 026202 (2004).
- [54] M. Gaudreault, J. M. Berbert, and J. Viñals, *Phys. Rev. E* **83**, 011903 (2011).
- [55] P. Kaluza, C. Strege, and H. Meyer-Ortmanns, *Phys. Rev. E* **82**, 036104 (2010).
- [56] S. Tanabe and K. Pakdaman, *Phys. Rev. E* **63**, 031911 (2001).
- [57] V. I. Nekorkin and O. V. Maslennikov, *Radiophys. Quantum Electron. (Engl. Transl.)* **54**, 56 (2011).
- [58] M. Courbage, O. V. Maslennikov, and V. I. Nekorkin, *Chaos Soliton. Fract.* **45**, 645 (2012).
- [59] O. V. Maslennikov and V. I. Nekorkin, *Radiophys. Quantum Electron. (Engl. Transl.)* **55**, 198 (2012).
- [60] C. W. Gardiner, *Handbook of Stochastic Methods for Physics, Chemistry and the Natural Sciences*, 3rd ed. (Springer-Verlag, Berlin, 2004).
- [61] *Phase Response Curves in Neuroscience: Theory, Experiment, and Analysis*, edited by N. W. Schultheiss, A. A. Prinz, and R. J. Butera (Springer, New York, 2012).
- [62] P. A. Tass, *Phase Resetting in Medicine and Biology: Stochastic Modeling and Data Analysis* (Springer, Berlin, 2007).
- [63] E. M. Izhikevich, *Dynamical Systems in Neuroscience: The Geometry of Excitability and Bursting* (MIT Press, Cambridge, 2007), Chap. 10.
- [64] C. C. Canavier, *Scholarpedia* **1**, 1332 (2006).

Disordered configurations of the Glauber model in two-dimensional networks

IVA BAČIĆ¹, IGOR FRANOVIĆ¹ and MATJAŽ PERC^{2,3,4}

¹ *Scientific Computing Laboratory, Center for the Study of Complex Systems, Institute of Physics Belgrade, University of Belgrade - Pregrevica 118, 11080 Belgrade, Serbia*

² *Faculty of Natural Sciences and Mathematics, University of Maribor - Koroška cesta 160, SI-2000 Maribor, Slovenia*

³ *CAMTP – Center for Applied Mathematics and Theoretical Physics, University of Maribor - Mladinska 3, SI-2000 Maribor, Slovenia*

⁴ *Complexity Science Hub - Josefstädterstraße 39, A-1080 Vienna, Austria*

received 31 January 2018; accepted 13 February 2018

published online 28 February 2018

PACS 89.75.Fb – Structures and organization in complex systems

PACS 89.75.Hc – Networks and genealogical trees

Abstract – We analyze the ordering efficiency and the structure of disordered configurations for the zero-temperature Glauber model on Watts-Strogatz networks obtained by rewiring 2D regular square lattices. In the small-world regime, the dynamics fails to reach the ordered state in the thermodynamic limit. Due to the interplay of the perturbed regular topology and the energy neutral stochastic state transitions, the stationary state consists of two intertwined domains, manifested as multiclustered states on the original lattice. Moreover, for intermediate rewiring probabilities, one finds an additional source of disorder due to the low connectivity degree, which gives rise to small isolated droplets of spins. We also examine the ordering process in paradigmatic two-layer networks with heterogeneous rewiring probabilities. Comparing the cases of a multiplex network and the corresponding network with random inter-layer connectivity, we demonstrate that the character of the final state qualitatively depends on the type of inter-layer connections.

Copyright © EPLA, 2018

The interplay of local dynamics and the underlying network topology has been in the focus of research in physics and various interdisciplinary fields [1–3], having recently attracted considerable interest in the context of phase ordering processes [4–6]. The Ising-Glauber model [7] constitutes one of the paradigmatic models for analyzing such processes [8]. While it has been introduced to describe the nonequilibrium dynamical behavior of magnetic systems consisting of a large number of interacting particles, it has since been applied to a variety of other problems, including those in social sciences [9], geology [10], and electrochemistry [11].

Within the Glauber model, the spin variables can assume two discrete values, having the states of nodes evolve according to the local majority rule. The Glauber model was initially defined on a regular lattice [7]. Nevertheless, given that non-lattice topologies including random, scale-free [12] and small-world [13] networks are often better suited to describe real-world systems, the issue of Glauber dynamics on complex networks has been gaining

increasing attention [8,14–16]. Apart from such models, complexity of interactions in many real-world systems may also involve “networks of networks” featuring modular or multilayer architecture [17], the scenarios which have been much less explored in the framework of Glauber dynamics.

Our work addresses two problems of ordering in complex networks: i) the disordered states of the zero-temperature Glauber model on monolayer rewired networks, where we identify two types of disordered configurations, and ii) the ordering process on two-layer rewired networks, where we find that the ordering process is strongly affected by the type of inter-layer connections.

In case of the two-dimensional square lattice, when only interactions between four nearest neighbors are taken into account, see fig. 1(a), the zero-temperature Glauber dynamics is multistable [18]. In particular, the system either reaches the ground state for $\approx 2/3$ of all the process realizations, or ends up in the frozen striped state with probability $p_f \approx 1/3$. Concerning rewired square lattices with coordination number $\langle k \rangle = 4$, it has been shown that

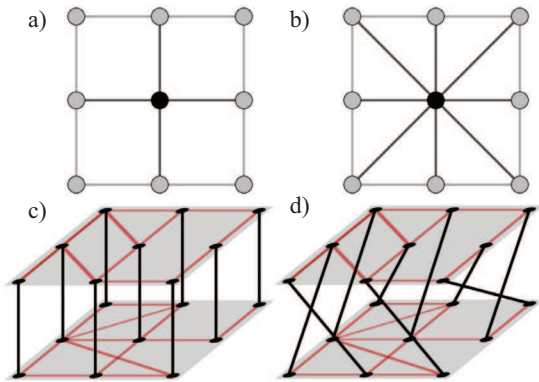


Fig. 1: (Color online) Considered network topologies. Panel (a) shows the scenario of a monolayer network with nearest-neighbor interactions ($k = 4$), whereas panel (b) shows the case where the next-nearest neighbor interactions are also included ($k = 8$). Panel (c) shows results for the multiplex two-layer network, whereas panel (d) shows results when there is random connectivity between the two layers.

the dynamics fails to reach the ground state [15,19], but little is known about the nature of the associated disordered configurations.

Our immediate goals are to understand why the Glauber model on small-world networks fails to reach ground state and to gain insight into the character of the disordered states on rewired networks with $\langle k \rangle = 4$ and $\langle k \rangle = 8$. We also study the ordering process on two-layer rewired networks with $\langle k \rangle = 4$, comparing the effects of different types of inter-layer connectivity, including multiplexing, see fig. 1(c), and the scenario with connections distributed between randomly selected pairs of nodes, cf. fig. 1(d).

Model. – In the Glauber model, the interactions are usually confined (but not necessarily restricted) to nearest-neighbor units. Incorporating higher-order competing (frustrated) interactions is one of the classical scenarios for the onset of new phases and potentially new types of phase transitions lying outside of Ising universality class. While the ferromagnetic interactions imposed by the model favor parallel alignment of spins, thermal noise prevents the system from reaching the ground state at any nonzero value of temperature. To avoid such stochastic effects which prevent full ordering, we consider systems quenched from an infinitely high temperature to absolute zero, in which spin states are initially uncorrelated and the net magnetization is vanishing. The Hamiltonian of the system is given by $H = -\sum_{\langle ij \rangle} J_{ij} S_i S_j$ where $S_i = \pm 1$ are Ising spin variables, the sum $\langle ij \rangle$ is over pairs of neighbors, and $J_{ij} > 0$ are ferromagnetic coupling constants, assumed to be uniform in our paper ($J_{ij} = J$). Each pair of parallel neighboring spins contributes $-J$ to the energy, while the contribution of antiparallel pairs is $+J$. Without loss of generality, we set $J = 1$ in the present study.

The state of the system evolves according to the majority rule applied to spins sequentially selected at random in each time step. This dynamical rule allows only energy

lowering or the energy neutral state transitions. The former correspond to events where the spin variable is updated to the state prevalent in its local neighborhood, while the latter conform to scenario without a local majority, such that the given spin evolves stochastically with both orientations being equally likely.

Watts and Strogatz [13] have introduced an algorithm for generating small-world and random graphs by gradually rewiring a regular lattice. In their model, links from the regular lattice are chosen at random and replaced with new ones until a desired fraction of links p is rewired. Rewiring effectively introduces shortcuts between distant nodes, thereby drastically reducing the mean shortest path even in the limit $p \rightarrow 0$. By increasing the amount of disorder ($p \rightarrow 1$) one obtains a random network with the mean connectivity conserved. Small-world networks are generated by introducing an intermediate level of disorder ($0 < p \ll 1$), and are characterized by the high clustering coefficient and the short average path length. The former implies that neighboring nodes tend to group in well connected clusters, whereas the latter means that an arbitrary distant node can be reached by a small number of intermediate links.

We simulate Glauber dynamics of Ising spins on Watts-Strogatz rewired networks generated from two-dimensional regular $L \times L$ lattices with periodic boundary conditions. To understand the interplay between topological effects and the local majority dynamical rule, we vary several parameters in addition to L and the rewiring probability p , including the mean connectivity degree $\langle k \rangle$ and the initial magnetization m_0 . As an additional ingredient, we also examine how the ordering process is affected by whether the Glauber dynamical rule allows for stochastic flipping or not. We refer to the rule without stochastic flipping as the modified Glauber rule.

To distinguish the influence of rewiring itself from the effect of connectivity of the network, we compare the results of simulations on networks with $\langle k \rangle = 4$ and $\langle k \rangle = 8$ in the small-world regime. We regard the next nearest neighbors as first neighbors in the topological sense by setting all interactions to be of equal strength. Assigning a finite value to the initial magnetization $m_0 \neq 0$ can be understood as introducing an initial bias toward local state clustering in the network. Modifying the Glauber dynamical rule by allowing state transitions only in the case of a strong local majority allows us to understand the effect of energy neutral processes on ordering in disordered topologies. In this scenario, nodes with an equal number of neighbors in both states are ignored when encountered during a trial rather than having their state determined stochastically. It turns out that the ground state is always reached on regular square lattices when a strong majority is necessary for state transition, *i.e.*, the striped state turns out to be the consequence of energy neutral stochastic flips.

To gain a more comprehensive insight into structure of the disordered configurations, we make a distinction between the domains comprised of topologically connected

nodes in the same state, and the clusters with respect to positions of the nodes on the original regular lattice. The lattice and the graph neighborhoods are always identical for spins placed on regular lattices. However, as the lattice structure is modified such that the links between neighbors are replaced by links to distant nodes, the lattice and the topological neighbors may not necessarily coincide, which results in rich patterns on the lattice. In order to investigate the crossover from frozen striped configurations occurring in regular lattices to disordered states occurring in the rewired lattices, we compare the correlation length ξ to characteristic graph length measures, namely the radius R , diameter D and the mean shortest path $\langle s \rangle$. The correlation length is defined as the decay rate of the two-point correlation function $G(l) = \langle S_i S_j \rangle - \langle S_i \rangle \langle S_j \rangle$ which measures the correlation of states as a function of the Manhattan distance l between the nodes. Note that ξ characterizes the competition between topology and dynamics on the state of distant nodes, while R , D and $\langle s \rangle$ are purely topological measures.

We also address the issue of how connecting two networks of the same size with different rewiring probabilities affects the ordering process. To do so, we compare the results obtained for the two-layer multiplex network (N bonds connecting nodes of two layers in one-to-one fashion) with the results for the case where the same number of inter-layer connections is distributed between randomly chosen pairs of nodes.

The main quantity of interest is the fraction of configurations that have not reached the ground state (“active configurations”) f_a after a given simulation time T as a function of p . The absolute value of net magnetization $|m|$ is an order parameter for individual systems: $|m| = 1$ corresponds to the ground case, whereas $|m| = 0$ corresponds to the case in which there is an equal number of spins in both states. Thus, we measure the dependence of the final value of the magnetization $|m_f|$ in disordered configurations on p . However, $|m_f|$ contains no information about clustering in the network.

We simulate the dynamics on networks consisting of 50×50 , 80×80 and 150×150 nodes for fixed values of N , $\langle k \rangle$, p and m_0 . The total number of trials in each particular case is set to 1000. In summary, our numerical algorithm consists of the following steps:

- I) *Regular network initialization.* Construct lattices with $k = 4$ or $k = 8$ as in fig. 1.
- II) *Rewiring.* Following the method described in [15], our rewiring process ensures that there are no self-loops or multiple links between pairs of nodes, and that the minimal connectivity degree is 2. Bonds are sequentially selected at random and rewired with probability p until a desired fraction p of the total number of bonds is rewired.
- III) *Spin state initialization.* The initial state is set by randomly putting each of the N spins into one of the

possible states. If the initial magnetization is m_0 , the state of each spin is set to $+1$ with the probability $p_{spin} = \frac{1+m_0}{2}$ and to -1 with probability $1 - p_{spin}$.

- IV) *Glauber dynamics.* The evolution of the system is governed by the original or the modified (non-stochastic) Glauber dynamical rule, proceeding either until it reaches the ground state or until it fails to do so after a predetermined number of steps. We choose this value to be $T = 5000N$ (5000 attempted spin flips per node).

In what follows, we first analyze the case of a monolayer Watts-Strogatz network, and then consider the ordering process in paradigmatic two-layer networks with two types of inter-layer connections.

Monolayer networks. – Figure 2(a) shows how the fraction of active configurations f_a depends on p for Watts-Strogatz networks with local Glauber dynamics following a zero-temperature quench ($m_0 = 0$). The nonlinear dependence of f_a on p is observed regardless of $\langle k \rangle$, but turns out to be qualitatively different for the cases $\langle k \rangle = 4$ and $\langle k \rangle = 8$. When $\langle k \rangle = 8$, with increasing randomness ($p \gtrsim 0.5$), the dynamics leads to almost complete ordering. Nevertheless, when $\langle k \rangle = 4$, a finite fraction of configurations fails to reach the ground state in the thermodynamic limit over the whole range of p values. In the small-world regime, however, the ground state is not reached in the thermodynamic limit in either case. The result that ordering cannot be attained in small worlds when state transitions are governed by Glauber dynamics has been previously demonstrated for rewired rings ($d = 1$) and rewired square lattices ($d = 2$) with $\langle k \rangle = 4$ [15,19].

One infers that the local neighborhood majority rule with stochastic spin flips cannot lead to an ordered state on graphs with a perturbed regular topology. While the neighborhood from the regular lattice is mostly conserved in the small-world limit, R , D and $\langle s \rangle$ on the other hand monotonically decrease with p due to the presence of shortcuts (see fig. 3). Thus, it follows that perturbing the local neighborhood essentially leads to dynamical frustration of the local majority rule. A very small amount of topological disorder is sufficient to induce the critical slowing-down of dynamics, causing the disordered states to appear as deformed stripes on the lattice. Further deformation of the stripes leads to multiclustering on the lattice, which is reflected in the crossover effect [20]. We have established that this effect corresponds to the drop of ξ below the topological distances. At the same time, the low value of ξ indicates the absence of long-range ferromagnetic order. The two-point correlation function is found to satisfy an exponential scaling law $G(l) \propto e^{-\frac{l}{\xi}}$ over the whole range of p . Furthermore, depending on the p value, both ξ and R , D and $\langle s \rangle$ exhibit different scaling regimes.

In particular, in the small-world regime, R , D , $\langle s \rangle$ and ξ exhibit a power law dependence on p , $r \propto p^{-a}$ with $r \in \{R, D, \langle s \rangle, \xi\}$ and $a \in \{a_R, a_D, a_{\langle s \rangle}, a_\xi\}$. For 80×80

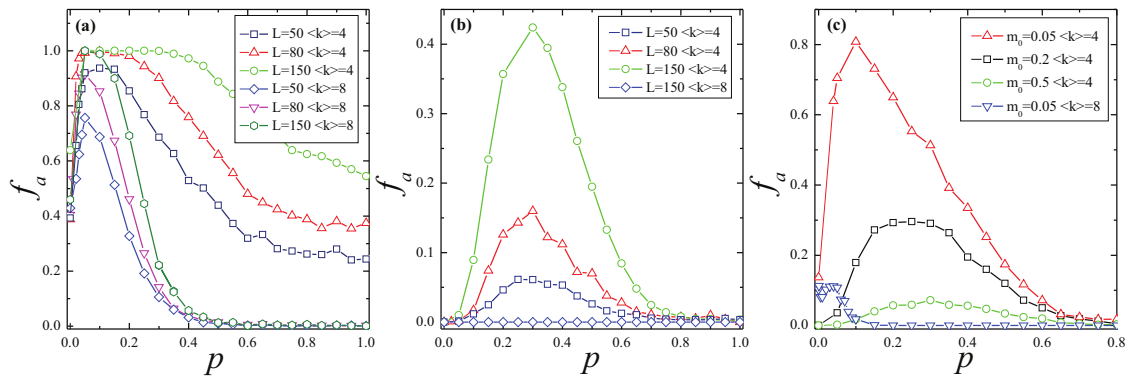


Fig. 2: (Color online) (a) Final fraction of active runs f_a in terms of rewiring probability p for the standard Glauber rule with $m_0 = 0$. The results are provided for networks with $\langle k \rangle = 4$ and $\langle k \rangle = 8$ neighbors and $L \in \{50, 80, 150\}$. Note that complete ordering is not observed in the small-world regime $0 < p \ll 1$ independent of $\langle k \rangle$. (b) Impact of modified Glauber rule: for $\langle k \rangle = 8$, the system reaches complete ordering (hence only the curve corresponding to $L = 150$ is shown), whereas for $\langle k \rangle = 4$, the frustration effect emerges at intermediate p , becoming more pronounced with the network size. Panel (c) displays f_a for systems governed by the standard Glauber rule starting from initial conditions $m_0 \neq 0$. The influence of small worldliness is such that it suppresses disorder regardless of $\langle k \rangle$ with increasing m_0 , while it still promotes disorder at intermediate p range for $\langle k \rangle = 4$.

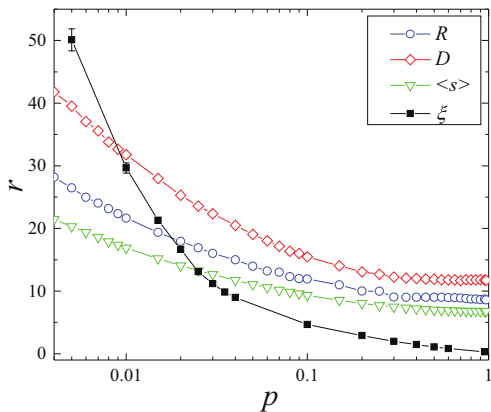


Fig. 3: (Color online) Correlation length ξ compared to graph distance measures (radius R , diameter D , and average path length $\langle s \rangle$) as functions of p . While ξ reflects the interplay between the dynamics and the network structure, the remaining quantities characterize purely topological features of the network. Crossing of $\xi(p)$ with other curves indicates the transition between the dynamics typical for the regular lattices and that for the rewired networks. Note that all four quantities exhibit a power law dependence $r \propto p^{-a}$ in the p region approximately coinciding with the small-world regime. The results refer to networks with 80×80 nodes and $\langle k \rangle = 4$.

networks, the following values for the exponent a are found: $a_R = -0.259 \pm 0.004$, $a_D = -0.296 \pm 0.005$, $a_{\langle s \rangle} = -0.25 \pm 0.003$ and $a_\xi = -0.77 \pm 0.01$. For larger values of p , the topological measures do not change significantly with increasing p indicating that topological effects remain the same after ≈ 0.5 . Nevertheless, ξ decays to zero as $p \rightarrow 1$, which implies that the dynamics is sensitive to rewiring over the whole range of p , as corroborated by the growing number of “clusters” of decreased sizes in disordered configurations for large p , see fig. 4.

Interestingly, a deeper understanding of the difference in ordering efficiency in terms of p may be gained by

considering f_a for configurations governed by the modified Glauber rule. Evidently, the difficulty in attaining order subsides when stochasticity is eliminated from the dynamics in the small-world limit regardless of $\langle k \rangle$, see fig. 2(b). In other words, the ground state is reached with probability one if energy-neutral state transitions are not allowed. This always holds for $\langle k \rangle = 8$, and also for networks with $\langle k \rangle = 4$ in the limits $p \rightarrow 0$ and $p \rightarrow 1$. For intermediate p , ordering remains suppressed to a certain degree.

The next objective is to demonstrate that varying initial magnetization m_0 allows one to interpolate between the influences of dynamics and topology. Figure 2(c) shows f_a as a function of p for $m_0 \neq 0$ under the standard Glauber rule. While initial bias towards local clustering promotes complete ordering for regular networks, the dynamical outcome is different for rewired networks. In case $\langle k \rangle = 8$, small values of $m_0 \neq 0$ significantly increase ordering, whereby the position of the peak of $f_a(p)$ coincides with the peak value of $f_a(p)$ at $m_0 = 0$. Perturbing the quenched initial state on graphs in the small-world regime increases the prevalence of the ground state. Nevertheless, the peaks of $f_a(p)$ curves for $\langle k \rangle = 4$ networks in fig. 2(c) shift toward the peak value from fig. 2(b) as m_0 is increased. A fraction of configurations still fails to reach the ground state for some values of p , even for high values of m_0 . The shift demonstrates that as the number of stochastic state transitions decreases due to the initial bias in clustering, the dynamical frustration is reduced. Nonetheless, the topological obstructions in networks with low $\langle k \rangle$ can suppress ordering even for high values of m_0 .

Further insight on this issue can be gained by observing how $|m_f|$ averaged over active configurations depends on p , see fig. 5. The initial increase in magnetization corresponds to the divergence of relaxation time in the limit $p \rightarrow 0$, *i.e.*, the crossover from large-world to small-world behavior. Expectedly, there is a qualitative difference in

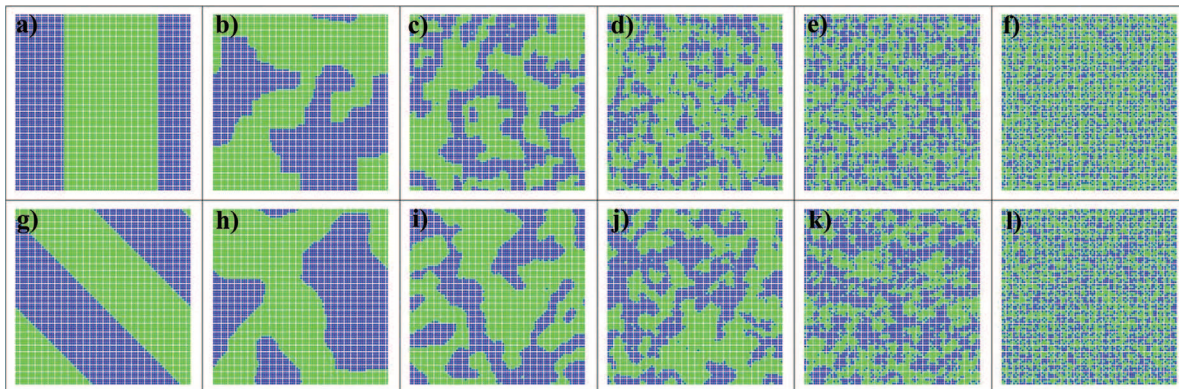


Fig. 4: (Color online) Snapshots of disordered configurations at $T = T_f$ on the lattice. The top (bottom) row refers to networks with $\langle k \rangle = 4$ ($\langle k \rangle = 8$). The rewiring probabilities are $p = 0$ in (a) and (g), $p = 0.02$ in (b) and (h), $p = 0.1$ in (c) and (i), $p = 0.3$ in (d) and (j), $p = 0.5$ in (e) and (k), as well as $p = 1$ in (f) and (l). The stripe structure is gradually lost with increasing p , giving way to the multiclustered states with respect to the original lattice. The number of domains increases with p as the network topology substantially departs from the lattice one. In terms of the network structure, each of the disordered configurations consists of two connected components. All the results are obtained for networks with 80×80 nodes.

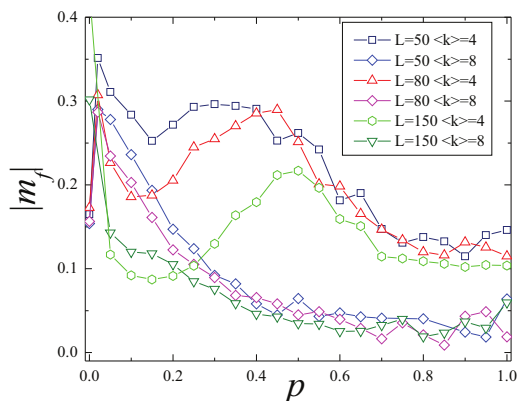


Fig. 5: (Color online) Final magnetization averaged over the ensemble of disordered configurations $|m_f|$ in dependence of p . For $\langle k \rangle = 8$, one finds approximately equal numbers of nodes in both states as $p \rightarrow 0$. For $\langle k \rangle = 4$, within the small-world regime, $|m_f|$ is reduced compared to the regular lattice, while for intermediate p , the droplet configurations lead to an increase of $|m_f|$. The peak of $|m_f|(p)$ gets shifted because the fraction of active runs is higher at a wider range of p values for larger networks, cf. fig. 2(a).

the $|m_f|(p)$ profile for different $\langle k \rangle$ under increasing p . The curves for $\langle k \rangle = 8$ monotonically decrease, indicating that the small number of configurations that does survive converges to a state consisting of a similar number of opposite spins in the limit $p \rightarrow 1$. In contrast, the initial decrease in $|m_f|$ for networks with $\langle k \rangle = 4$ is followed by the peak at intermediate values of p , associated to the presence of droplet configurations with $|m_f| \rightarrow 1$.

Moreover, we have verified that the disordered configurations in the small-world regime consist of two intertwined topological spin domains of almost similar size with stochastically fluctuating interfaces. An example of such a two-component state for $p = 0.1$ is provided in fig. 6, whereby the corresponding lattice domain configuration is shown in fig. 4(c). Blinkers that arise as a result of the

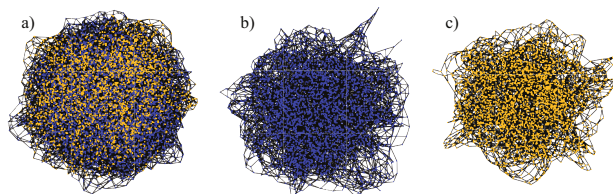


Fig. 6: (Color online) Example of a disordered configuration obtained for the network of size 80×80 , with $\langle k \rangle = 4$ neighbors on average and $p = 0.1$ rewired links. (a) refers to the full configuration, whereas (b) and (c) show the larger component (3637 nodes) and the smaller component (2763 nodes), respectively. The final magnetization is $|m_f| \approx 0.14$. The nodes are separated into two domains of similar size, forming a multi-domain state on the lattice, cf. fig. 5(c).

long-range connections can be present along with stochastic flipping of interfaces on the lattice. Increasing p corresponds to the formation of domains with decreasing size with respect to the lattice. Several examples of configurations with two topological components for different p are shown in fig. 4. The number of these domains counted on the lattice grows exponentially with p (not shown). In the random network limit, as the fraction of links belonging to the original lattice $1 - p$ decreases, clusters become indistinguishable when observed on the lattice. Topologically, the two-domain configuration is reminiscent of the disordered configurations of the voter model on small-world networks [8,21]. Once the dynamics cannot cause further decrease in energy, the interface length reaches a constant value, as interface diffusion is no longer possible. In this scenario, while a fraction of nodes with even connectivity degrees continues to flip indefinitely with no energy cost, the states of the odd-degree nodes become stationary.

Nevertheless, the disordered configurations associated to the increase of f_a in fig. 2(b) for $\langle k \rangle = 4$ are frozen at very high values of $|m_f|$, *viz.* $|m_f| \rightarrow 1$ in

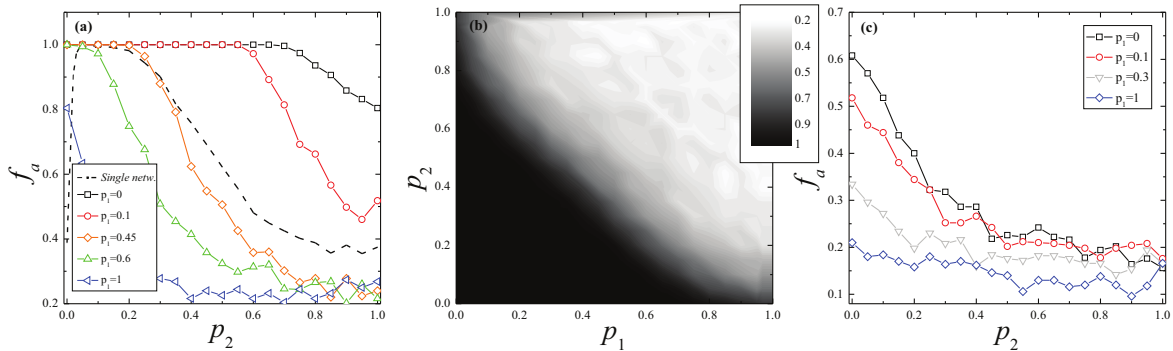


Fig. 7: (Color online) (a) Ordering in two-layer multiplex networks: f_a for the layer with rewiring probability p_1 (see the legend) in terms of the rewiring probability p_2 of the other layer. For comparison, the results for the single (monolayer) network are indicated by the dashed line. (b) f_a of a single layer of a multiplex network as a function of p_1 and p_2 . The states of two layers are strongly correlated, but the ordering is completely inhibited in the small-world regime. (c) f_a of a layer of the network with random inter-layer connectivity. Ordering is significantly improved for all values of p . All the results are obtained for networks with 80×80 nodes and $\langle k \rangle = 4$.

the thermodynamic limit, and correspond to *absorbing* states of the network. These configurations result from low connectivity and consist of a tiny fraction of spins isolated in small domains surrounded by the “sea” of nodes of the opposite orientation. In this scenario, nodes with small k form stable droplets of opposing magnetization which cannot be dynamically influenced by the nodes from the rest of the network, preventing the system from reaching the full order. These droplets may appear on the remnants of the regular lattice, such that their interior consists of nodes connected by links from the regular lattice ($k = 4$), whereas their boundary is mainly comprised of nodes with one removed link ($k = 3$), thereby trapping the “interior” in the same state. Even-degree nodes that appear on the boundaries have more links with nodes within the droplet than with other neighbors, such that their state cannot be changed either. With further rewiring of the lattice, stable droplets may still form as even smaller groups of interconnected nodes with small degrees ($k = 2$ or $k = 3$), likewise disconnected from the rest of the network. The larger the network, the more likely becomes such a scenario. Also, for larger network sizes, a larger number of droplets may be present, which is the reason why a larger fraction of configurations fails to reach order. This peculiar frustration on the remnants of a regular lattice also accounts for the incomplete ordering of systems governed by the standard Glauber dynamics in rewired networks with $\langle k \rangle = 4$, and explains for the difference in the behavior in the limit $p \rightarrow 1$. Final configurations in networks with $\langle k \rangle = 4$ can consist of two large components and a few isolated droplets for p above the small-world regime, similar to final configurations obtained for $m_0 \neq 0$.

Two-layer networks. – We now address the ordering process in multilayer networks, focussing on the paradigmatic example of two coupled $\langle k \rangle = 4$ networks with different rewiring probabilities p_1 and p_2 . By our

algorithm, the individual layers are rewired consecutively, after which N links are introduced between them, either at random or with the one-to-one correspondence between the layers’ nodes. The simulation is terminated after $2T$ steps if order is not reached. Note that introducing new links effectively generates a large network with $\langle k \rangle = 5$ and $5N$ bonds.

Our findings indicate that both cases lead to highly correlated states of layers, which are simultaneously ordered/disordered and have $m_{f_1} \approx m_{f_2}$. For this reason, f_a of a single layer presents an appropriate quantity to characterize the ordering process. We find that the dependence of f_a on rewiring probability changes qualitatively depending on the nature of the inter-layer bonds, cf. fig. 7(a) and fig. 7(c). The multiplex configuration turns out to suppress ordering of both networks in the small-world regime, as indicated in fig. 7(a) and fig. 7(b). However, fig. 7(a) shows that ordering efficiency can be increased if at least one of the networks is “sufficiently random”, with a smooth transition taking place at $0.35 \lesssim p \lesssim 0.45$. Interestingly, the other scenario, which involves placing the same number of bonds between randomly chosen pairs of nodes from both networks, promotes both ordering and correlation between the layer states. This is corroborated by fig. 7, suggesting that regardless of p_1 and p_2 , ordering in this case is significantly improved compared to that on a single network and the multiplex network.

The curves obtained for multiplex networks resemble the ones obtained for the single network even for p as large as 0.6, while those obtained for random inter-layer connections are monotonically decreasing as p_2 is increased over the whole range of p . Even though in both cases networks become correlated in terms of m_f and ordering, multiplexing seems to preserve the type of dynamics obtained on small-world structures of one network, while introducing random bonds between the layers destroys the small-worldliness effect.

Conclusions. – We have analyzed ordering efficiency of the Glauber model of Ising spin kinetics on the Watts-Strogatz networks obtained by rewiring from the two-dimensional square lattices with coordination numbers $\langle k \rangle = 4$ and $\langle k \rangle = 8$. We have extended the previous results concerning the failure of such systems to reach the ground state in the small-world regime $0 < p \ll 1$, gaining insight into the associated disordered configurations. The fraction of active configurations exhibits a nonlinear dependence on the rewiring probability. It is interesting that a similar type of dependence has been observed in relation to the synchronization process on small-world networks [22]. It is found that the Glauber dynamics on small-world networks becomes stuck in metastable stationary active configurations, which consist of two intertwined domains of opposite spins, whereby the fraction of nodes on the interfaces flips indefinitely. This effect is manifested as clustering patterns in the lattice representation. The size of domains on the lattice becomes smaller as p is increased. We have demonstrated that the limiting value of p at which the number of lattice and topological domains is equal (to two) corresponds to the value where the correlation length ξ becomes smaller than the average path length in the network.

Our analysis shows that the active configurations in the small-world regime emerge when the perturbed regular topology constrains the number of possible energy lowering processes, while the stochastic energy-neutral spin-flipping processes contribute to dynamical frustration and trap the system in a set of metastable states with the same energy. While the ground state is not accessible because energy lowering processes are not possible, the energy-neutral processes allow for the transitions between states of the same energy. This is similar to what has been reported for Glauber dynamics on 3D regular lattices [23], Glauber dynamics on random graphs [8], and the voter model on small-world networks [21].

We have further demonstrated that there exists a finite probability of finding another type of disordered configuration in networks with low connectivity for intermediate values of p . These are frozen, almost completely ordered states with a few isolated droplets of opposing magnetization. For $\langle k \rangle = 8$, such configurations become unlikely due to the high average connectivity degree in the network, giving way to fully ordered states if p is sufficiently increased ($p > 0.5$). In networks with $\langle k \rangle = 4$, a certain fraction of configurations exists as a combination of these states, especially if an initial bias towards clustering ($m_0 \neq 0$) is introduced.

We have also examined the features of the ordering process in paradigmatic two-layer networks. It has been found that the structure of inter-layer connections strongly affects the ordering process. In particular, multiplexing decreases ordering efficiency in the small-world regime $0 < p \ll 1$, but improves it if the rewiring probability in both layers is sufficiently high. Nevertheless, random connectivity between the layers always promotes ordering,

regardless of layer topology. In all the considered scenarios, the layers typically end up in highly correlated states.

We believe that the future research may be directed towards extending our findings on the dynamics of interacting rewired networks. In particular, it could be interesting to modify inter-layer coupling strengths, vary the number of connections between the layers or consider hierarchical networks and networks with a large number of layers.

* * *

This research was supported by the Ministry of Education, Science and Technological Development of Republic of Serbia (Grant 171017) and by the Slovenian Research Agency (Grants J1-7009 and P5-0027).

REFERENCES

- [1] STROGATZ S., *Nature*, **410** (2001) 268.
- [2] ALBERT R. and BARABÁSI A.-L., *Rev. Mod. Phys.*, **74** (2002) 47.
- [3] BOCCALETTI S., LATORA V., MORENO Y., CHAVEZ M. and HWANG D.-U., *Phys. Rep.*, **424** (2006) 175.
- [4] BRAY A. J., *Adv. Phys.*, **51** (2002) 481.
- [5] CASTELLANO C., *Rev. Mod. Phys.*, **81** (2009) 591.
- [6] PASTOR-SATORRAS R., CASTELLANO C., VAN MIEGHEM P. and VESPIGNANI A., *Rev. Mod. Phys.*, **87** (2015) 925.
- [7] KRAPIVSKY P. L., REDNER S. and BEN-NAIM E., *A Kinetic View of Statistical Physics* (Cambridge University Press, Cambridge) 2010.
- [8] CASTELLANO C., LORETO V., BARRAT A., CECCONI F. and PARISI D., *Phys. Rev. E*, **71** (2005) 066107.
- [9] STAUFFER D., *Am. J. Phys.*, **76** (2008) 470.
- [10] GANGULY J., *Advances in Physical Geochemistry: Diffusion, Atomic Ordering, and Mass Transport* (Springer, New York) 2012.
- [11] BOSCO E., *J. Electroanal. Chem.*, **346** (1993) 433.
- [12] BARABÁSI A.-L. and ALBERT R., *Science*, **286** (1999) 509.
- [13] WATTS D. J. and STROGATZ S. H., *Nature*, **393** (1998) 440.
- [14] CASTELLANO C. and PASTOR-SATORRAS R., *J. Stat. Mech.* (2006) P05001.
- [15] HERRERO C. P., *J. Phys. A: Math. Theor.*, **42** (2009) 415102.
- [16] BAEK Y., HA M. and JEONG H., *Phys. Rev. E*, **85** (2012) 031123.
- [17] BOCCALETTI S. *et al.*, *Phys. Rep.*, **544** (2014) 1.
- [18] SPIRIN V., KRAPIVSKY P. L. and REDNER S., *Phys. Rev. E*, **65** (2001) 016119.
- [19] BOYER D. and MIRAMONTES O., *Phys. Rev. E*, **67** (2003) 035102.
- [20] BARTHÉLÉMY M. and AMARAL L. A. N., *Phys. Rev. Lett.*, **82** (1999) 3180.
- [21] CASTELLANO C., VILONE D. and VESPIGNANI A., *Europhys. Lett.*, **63** (2003) 153.
- [22] GRABOW C., HILL S. M., GROSSKINSKY S. and TIMME M., *Europhys. Lett.*, **90** (2010) 48002.
- [23] SPIRIN V., KRAPIVSKY P. L. and REDNER S., *Phys. Rev. E*, **63** (2001) 036118.

Noise-induced switching in two adaptively coupled excitable systems

Iva Bačić¹, Serhiy Yanchuk², Matthias Wolfrum³, and Igor Franović^{1,a}

¹ Scientific Computing Laboratory, Center for the Study of Complex Systems, Institute of Physics Belgrade, University of Belgrade, Pregrevica 118, 11080 Belgrade, Serbia

² Institute of Mathematics, Technische Universität Berlin, Straße des 17. Juni 136, 10623 Berlin, Germany

³ Weierstrass Institute, Mohrenstrasse 39, 10117 Berlin, Germany

Received 30 April 2018 / Received in final form 19 June 2018
Published online 12 December 2018

Abstract. We demonstrate that the interplay of noise and plasticity gives rise to slow stochastic fluctuations in a system of two adaptively coupled active rotators with excitable local dynamics. Depending on the adaptation rate, two qualitatively different types of switching behavior are observed. For slower adaptation, one finds alternation between two modes of noise-induced oscillations, whereby the modes are distinguished by the different order of spiking between the units. In case of faster adaptation, the system switches between the metastable states derived from coexisting attractors of the corresponding deterministic system, whereby the phases exhibit a bursting-like behavior. The qualitative features of the switching dynamics are analyzed within the framework of fast-slow analysis.

1 Introduction

In many complex systems, ranging from biology, physics and chemistry to social sciences and engineering, the interaction patterns are not static, but are rather affected by the states of constituent units [1–4]. This gives rise to complex feedback mechanisms, where the coupling weights adapt to dynamical processes at the units, which in turn influences the evolution of units itself. Modeling of such systems is based on the paradigm of adaptive networks, where self-organization unfolds both at the level of coupling weights and the collective states of the units, typically involving a separation of characteristic timescales. The faster and the slower timescales are naturally associated to the dynamics of units and couplings, respectively, such that the short-term evolution of the units occurs on a quasi-static network, whereas the slow changes in coupling weights depend on the time-averaged dynamics of the units. An important example of adaptive connectivity is provided by neuronal systems, where the strength of synaptic couplings is adjusted to the underlying spiking activity via spike-time-dependent plasticity (STDP), a temporally asymmetric form of Hebbian learning [5],

^a e-mail: franovic@ipb.ac.rs

promoting causal relationship between the spikes of pre- and postsynaptic neurons [6–8].

Motivated by the research on neuronal systems, in the present paper we study a simplified model which incorporates the basic ingredients of neurodynamics, such as excitability, plasticity and noise. The considered system consists of two adaptively coupled active rotators, whose intrinsic dynamics is set to excitable regime and subjected to noise. The plasticity rule is introduced in such a way that one may continuously interpolate between the coupling dynamics characteristic to Hebbian learning and STDP. We demonstrate that the interplay of plasticity and noise may facilitate two qualitatively different forms of slow stochastic fluctuations, depending on the adaptation rate. While for slower adaptation the self-organized dynamics consists of switching between the two modes of noise-induced oscillations, in case of faster adaptation, the switching dynamics comprises metastable states associated to attractors of the deterministic system.

In the context of neuroscience, one may compare the considered system to a binary neuron motif. It is well known that the same structural motif, defined at the level of anatomy, can support multiple functional motifs [9–12], characterized by different weight configurations and potentially distinct directions of information flow. In these terms, our study will show that the co-effect of plasticity and noise may (i) contribute to the emergence of different functional motifs on top of the given structural one and (ii) trigger slow alternation between the functional motifs.

So far, the co-effects of noise and the STDP plasticity rule have been analyzed in systems of two coupled neural oscillators, as well as in networks of oscillators. In case of two units, multistability between different weight configurations has been found, surprisingly indicating that noise may stabilize configurations of strong bidirectional coupling absent in the deterministic system [13]. At variance with this, our study concerns excitable local dynamics and explicitly addresses the slow stochastic fluctuations between metastable states. For networks of adaptively coupled neural or phase oscillators, the previous research has mainly focused on the impact of plasticity on the synchronization behavior. In the absence of noise, several generic forms of macroscopic dynamics have been identified, including desynchronized or partially synchronized states with weak couplings, as well as cluster states [14–18]. In presence of noise, an interesting effect of self-organized noise resistance to desynchronization has been reported in the case of a network of neural oscillators [19]. In networks of excitable units, the STDP rule has been shown to give rise to oscillating coupling configurations that facilitate switching between strongly and weakly synchronized states [20–22].

The paper is organized as follows. The details of the model are introduced in Section 2. An overview of the underlying deterministic dynamics, characterizing the impact of plasticity on the stationary states and the onset of emergent oscillations, is provided in Section 3. Section 4 is dedicated to a fast–slow analysis of the deterministic dynamics, whereas in Section 5 are explained the features of the two generic types of switching behavior. In Section 6 we provide a summary of our main results.

2 Model

We consider a system of two stochastic active rotators interacting by adaptive couplings, where the dynamics of the phases $\{\varphi_1(t), \varphi_2(t)\}$ and the coupling weights $\{\kappa_1(t), \kappa_2(t)\}$ is given by

$$\begin{aligned}\dot{\varphi}_1 &= I_0 - \sin \varphi_1 + \kappa_1 \sin(\varphi_2 - \varphi_1) + \sqrt{D}\xi_1 \\ \dot{\varphi}_2 &= I_0 - \sin \varphi_2 + \kappa_2 \sin(\varphi_1 - \varphi_2) + \sqrt{D}\xi_2 \\ \dot{\kappa}_1 &= \epsilon(-\kappa_1 + \sin(\varphi_2 - \varphi_1 + \beta)) \\ \dot{\kappa}_2 &= \epsilon(-\kappa_2 + \sin(\varphi_1 - \varphi_2 + \beta)),\end{aligned}\tag{1}$$

where $\varphi_1, \varphi_2 \in S^1$, while κ_1 and κ_2 are real variables. The rotators are assumed to be identical, having their local dynamics governed by the excitability parameter I_0 , which gives rise to a SNIPER bifurcation at $I_0 = 1$. We focus on the excitable regime, such that $I_0 = 0.95$ is kept fixed throughout the paper. In this case, the uncoupled system always converges to a steady state, whereas the collective dynamics emerges due to interaction and noise. The parameter $\epsilon \ll 1$ defines the scale separation between the fast dynamics of the phases and the slow dynamics of adaptation. White noise of variance D acts only within the subspace of fast variables, whereby the terms $\xi_1(t)$ and $\xi_2(t)$ are independent ($\xi_i(t)\xi_j(t') = \delta_{ij}\delta(t-t')$ for $i, j \in \{1, 2\}$). In the context of neuroscience, I_0 can be interpreted as external bias current, whereas the impact of stochastic terms is analogous to that of synaptic noise. Note that the deterministic version of (1) is symmetric with respect to the exchange of indices $1 \leftrightarrow 2$.

The plasticity rule is controlled by the parameter β , which allows one to interpolate between the different adaptation modalities. The analogy between the adaptivity dynamics in classical neuronal systems and the systems of coupled phase oscillators has been addressed in [14,23,24], whereas a deeper analysis of the correspondence between the phase-dependent plasticity rules and the STDP has been provided in [13]. From these studies, it follows that the scenario found for $\beta = 3\pi/2$, where the stationary weights increase for smaller phase differences and decrease for larger ones (“like-and-like” form of behavior), qualitatively resembles the Hebbian learning rule [23,24]. Nevertheless, in the case $\beta = \pi$, the two coupling weights always change in opposite directions, which may be interpreted as promoting an STDP-like plasticity rule. In the present paper, we are interested in the β interval between these two limit cases, since it admits two coexisting excitable fixed points.

3 Deterministic dynamics of the full system

In this section, we analyze the details of the *deterministic* dynamics of the full system (1), considering first the stationary states and the associated excitability feature, and then focusing on the scenario that gives rise to emergent oscillations.

3.1 Stationary states and excitable dynamics

Fixed points $(\varphi_1^*, \varphi_2^*, \kappa_1^*, \kappa_2^*)$ of the complete system (1) for $D = 0$ are given by the solutions of the following set of equations:

$$\begin{aligned} \sin \varphi_1^* - \sin(\varphi_2^* - \varphi_1^* + \beta) \sin(\varphi_2^* - \varphi_1^*) &= I_0, \\ \sin \varphi_2^* - \sin(\varphi_1^* - \varphi_2^* + \beta) \sin(\varphi_1^* - \varphi_2^*) &= I_0, \end{aligned} \quad (2)$$

with

$$\begin{aligned} \kappa_1^* &= \sin(\varphi_2^* - \varphi_1^* + \beta), \\ \kappa_2^* &= \sin(\varphi_1^* - \varphi_2^* + \beta). \end{aligned} \quad (3)$$

Equation (2) can be solved numerically for any fixed parameter set, or numerical path-following can be applied in order to study the dependence of the fixed points on the parameters.

The bifurcation diagram in Figure 1 shows how the number and stability of fixed points of the full system change with β . In particular, depending on β , there may be two, four or six fixed points. Due to symmetry, the solutions always appear in pairs of points sharing the same stability features. Since our study concerns plasticity rules which support excitable fixed points, we have confined the analysis to the interval $\beta \in (3.298, 4.495)$, where the system has *two stable* fixed points, which lie off the synchronization manifold $\varphi_1 = \varphi_2$. Apart from that, there are also four unstable

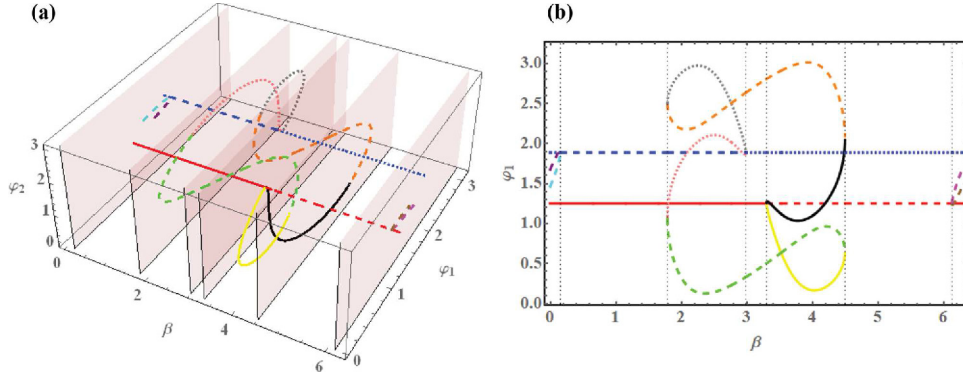


Fig. 1. (a) Bifurcation diagram for the fixed points of system (1) with $D = 0$ in the $(\beta, \varphi_1, \varphi_2)$ space. (b) Projection of the bifurcation diagram to (β, φ_1) plane. The two fixed points independent on β belong to the synchronization manifold: the red (blue) one is always longitudinally stable (unstable). The solid lines denote stable fixed points, whereas the dashed and dotted lines denote saddles of unstable dimension 1 and 2, respectively.

fixed points. The bifurcations associated to the boundaries of the given β interval are as follows: at $\beta = 3.298$ the system undergoes a supercritical symmetry-breaking pitchfork bifurcation where a symmetry related pair of two stable fixed points off the synchronization manifold is created, whereas at $\beta = 4.495$, this pair meets another pair of unstable fixed points off the synchronization manifold such that both are annihilated in symmetry related inverse saddle-node bifurcations. For instance, at $\beta = 4.1$, one finds the symmetry related pair of stable foci given by $(\varphi_1, \varphi_2, \kappa_1, \kappa_2) = (1.177, 0.175, 0.032, -0.92)$ and $(\varphi_1, \varphi_2, \kappa_1, \kappa_2) = (0.175, 1.177, -0.92, 0.032)$. Note that these weight levels support effective master-slave configurations, where one unit exerts a much stronger influence on the other unit than vice versa.

The two stable asymmetric fixed points in the interval $\beta \in (3.298, 4.495)$ are excitable, and may exhibit several different types of response to external perturbations, see the classification in Figure 2. Introducing the perturbations by setting different initial conditions, we plot in Figure 2 the phase dynamics in the fast subspace while keeping the weights (κ_1, κ_2) fixed. Note that in the case where both units respond with a single spike, the order of firing is such that the unit with larger initial phase $\varphi_i(0)$, $i \in \{1, 2\}$ fires first.

3.2 Onset of oscillations

The onset of emergent oscillations in system (1) with $D = 0$ depends on the interplay between the plasticity rule, specified by β , and the speed of adaptation, characterized by ϵ . A parameter scan indicating the variation of κ_1 , $A_{\kappa_1} = \max(\kappa_1(t)) - \min(\kappa_1(t))$ in terms of (β, ϵ) is shown in Figure 3a. The results are obtained by numerical continuation beginning from a stable periodic solution, such that the final state reached for a certain set of (β, ϵ) values provides the initial conditions for the simulation of the system at incremented parameter values. By this method, we have determined the maximal stability region of the periodic solution.

One finds that for a fixed β , there actually exists an interval of timescales separation $\epsilon \in (\epsilon_{min}, \epsilon_{max})$ admitting oscillations, cf. Figure 3b. The periodic solutions in this interval coexist with the two symmetry-related stable stationary states. One observes that the threshold ϵ_{min} reduces with β , whereas the upper boundary value ϵ_{max} grows with increasing β . The detailed bifurcation mechanisms behind the onset

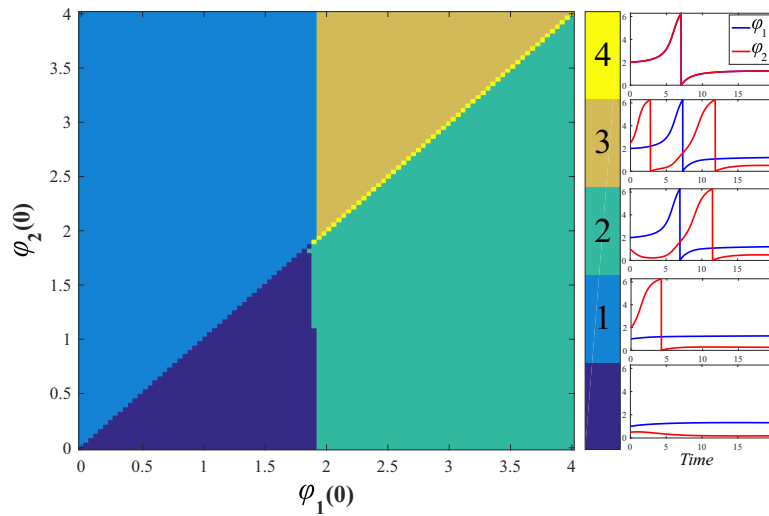


Fig. 2. Modalities of the response to external perturbation for system (1) with $D = 0$. The system parameters are $I_0 = 0.95$, $\epsilon = 0.01$ and $\beta = 4.212$, whereas the initial conditions for the coupling weights are set to $\kappa_1(0) = -0.0077$, $\kappa_2(0) = -0.846$. Depending on the initial phases $(\varphi_1(0), \varphi_2(0))$, one may observe the following regimes: (0) no spikes; (1) the unit with larger $\varphi(0)$ emits one spike and the other does not; (2) both units emit a single spike, with the unit with larger $\varphi(0)$ firing first; (3) the unit with larger $\varphi(0)$ emits two spikes and the other unit emits one; (4) both units spike synchronously.

of oscillations and multistability are beyond the scope of this paper, and essentially involve an interplay between the fast and slow variables.

Enhancing ϵ under fixed β gives rise to a supercritical symmetry-breaking pitchfork bifurcation of limit cycles, indicated by PFL in Figure 3b. Below the bifurcation, the phases $\varphi_1(t)$ and $\varphi_2(t)$ maintain a small phase-shift, while the oscillation profiles $\kappa_i(t), i \in \{1, 2\}$ are rather different, see Figures 3d and 3e, respectively. Above the bifurcation, the system gains the anti-phase space-time symmetry $\varphi_1(t) = \varphi_2(t + T/2), \kappa_1(t) = \kappa_2(t + T/2)$ where T denotes the oscillation period, cf. the associated waveforms in Figures 3g and 3f.

4 Slow-fast analysis of the deterministic dynamics

The deterministic dynamics in case of slow adaptation, corresponding to a strong timescale separation between the fast and slow variables, may be analyzed within the framework of standard fast-slow analysis. In general, one may either consider the layer problem, defined on the fast timescale, or the reduced problem, which concerns the slow timescale. Within the layer problem, the aim is to determine the fast flow dynamics $\varphi_1(t; \kappa_1, \kappa_2), \varphi_2(t; \kappa_1, \kappa_2)$ by treating the slow variables κ_1 and κ_2 as parameters, whereas the reduced problem consists in determining the dynamics of the slow flow $(\kappa_1(t), \kappa_2(t))$ (reduced flow) assuming that the fast flow of the layer problem is either at a stable equilibrium or at the averaged value of a stable regime.

In this section, we first investigate the fast layer problems. Depending on the values of the slow variables (κ_1, κ_2) , the fast flow can exhibit several attractors, such that multiple sheets of the slow flow emerge from the averaged dynamics on the different attractors of the fast flow.

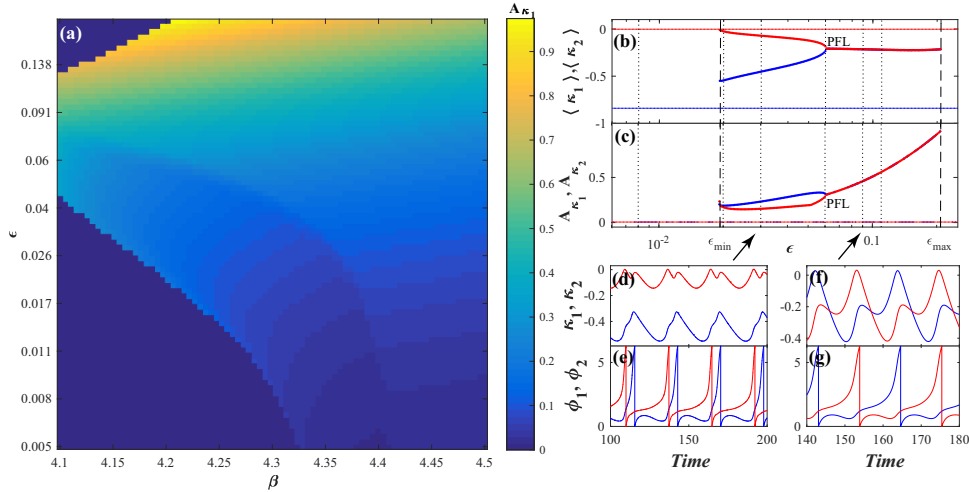


Fig. 3. Onset of oscillations in the full system (1) for $D = 0$. In panel (a) is shown how the variation A_{κ_1} of coupling weight κ_1 changes in the (β, ϵ) plane. Panel (b) shows how the mean coupling weights $\langle \kappa_1 \rangle$ and $\langle \kappa_2 \rangle$ of oscillatory states (thick lines) change with ϵ under fixed $\beta = 4.212$. The thin solid lines indicate the stationary state. In panel (c) are plotted the analogous dependencies for variation of the oscillation. The dotted lines in (b) and (c) indicate the ϵ values corresponding to the time traces in Figure 7, whereas the dashed lines indicate the boundaries of the ϵ region supporting the stable periodic solutions. The symmetry-breaking pitchfork bifurcation of limit cycles is denoted by PFL. In panels (d)–(g) are shown the waveforms of periodic solutions without and with the anti-phase space-time symmetry, obtained for $\epsilon = 0.03$ and $\epsilon = 0.09$, respectively (see the arrows). The excitability parameter is fixed to $I_0 = 0.95$.

4.1 Dynamics of the fast flow

Within the layer problem, one studies the dynamics of the fast variables

$$\begin{aligned}\dot{\varphi}_1 &= I_0 - \sin \varphi_1 + \kappa_1 \sin(\varphi_2 - \varphi_1) \\ \dot{\varphi}_2 &= I_0 - \sin \varphi_2 + \kappa_2 \sin(\varphi_1 - \varphi_2),\end{aligned}\quad (4)$$

where $\kappa_1, \kappa_2 \in [-1, 1]$ are considered as additional system parameters. Formally, system (4) is obtained by setting $\varepsilon = 0$ in (1) for $D = 0$.

The numerically obtained bifurcation diagram in Figure 4a shows that the fast flow is monostable for most of the (κ_1, κ_2) values, possessing either an equilibrium or a limit cycle attractor. The stability boundary of the periodic solution (red curves) has been obtained by the method of numerical continuation where, beginning from a stable periodic solution, the initial conditions for incremented parameter values are given by the final state reached for the previous set of (β, ϵ) values. The coexistence between a stable fixed point, lying on the synchronization manifold, and a limit cycle is found within a small region near the diagonal, see Figure 4a. Let us first classify the fixed points of the fast flow and then examine the scenarios that give rise to oscillations.

It can be shown that the fast flow admits either two or four fixed points, with the associated regions indicated in Figure 4b. In particular, two fixed points FP1 and FP2 on the synchronization manifold are *independent* on κ_1 and κ_2 . They are given by $(\varphi_1^*, \varphi_2^*) = (\arcsin I_0, \arcsin I_0)$ and $(\varphi_1^*, \varphi_2^*) = (\pi - \arcsin I_0, \pi - \arcsin I_0)$. One may also find two additional fixed points off the synchronization manifold, referred

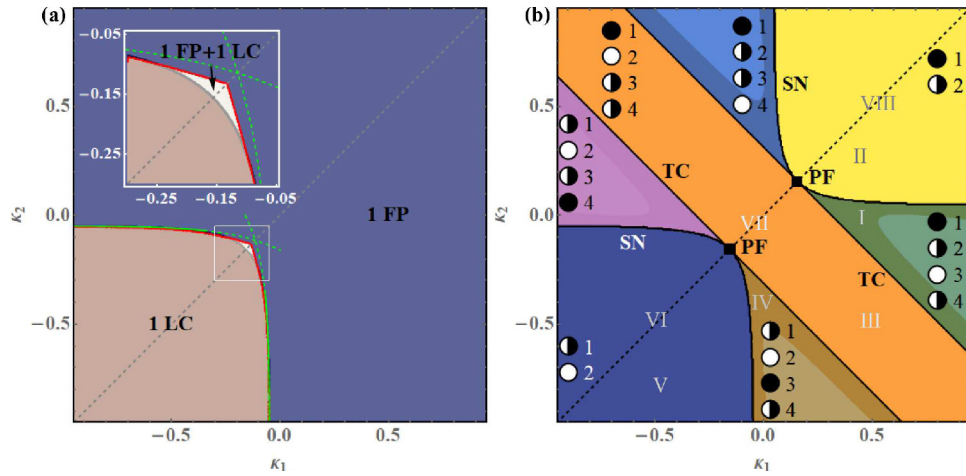


Fig. 4. (a) Attractors of the fast flow (4) in terms of κ_1 and κ_2 , now considered as parameters. The fast flow is typically monostable, supporting either a stable fixed point (FP) or a stable limit cycle (LC), apart from a small region around the main diagonal, where it exhibits bistable behavior. The green dashed curves indicate approximations of two branches of SNIPER bifurcations, obtained by the method described in the text. The red lines correspond to the numerically determined stability boundaries of the oscillatory solution. (b) Classification of the fixed points of the fast flow (4). The fixed points are labeled the same way as in the main text, with their stability indicated as follows: full circles denote stable fixed points, semi-full circles represent saddle points and white circles correspond to doubly unstable fixed points. Within the four light-shaded triangular-shaped regions, the doubly unstable fixed point is a focus, rather than a node. The notation I–VIII refers to parameter values corresponding to the phase portraits in Figure 5.

to as FP3 and FP4 in Figure 4b. The bifurcations affecting the number and stability of the fixed points, beginning from the lower left region of the (κ_1, κ_2) plane, can be summarized as follows. Along the main diagonal $\kappa_1 = \kappa_2$, we find two points of supercritical pitchfork bifurcations (PF), where from the symmetric fixed points the saddles FP3 and FP4 appear and disappear. Off the main diagonal, the pitchforks are unfolded into curves of saddle-node (SN) and transcritical bifurcations (TC), see Figure 4b.

The (κ_1, κ_2) region featuring stable oscillations almost completely matches the lower left domain admitting two unstable fixed points. Within this region, each periodic solution obtained for (κ_1, κ_2) above the main diagonal $\kappa_1 = \kappa_2$ has a counterpart in the domain below the main diagonal, related to it by the exchange symmetry of units indices. Typically, the periodic solutions emerge via SNIPER bifurcations, comprising two branches where either κ_1 or κ_2 remain almost constant and close to zero. In both cases, the two fixed points that collide and disappear are FP3 and FP4. Nevertheless, such scenarios cannot be maintained in the small (κ_1, κ_2) region admitting coexistence between a fixed point and a limit cycle, because the SNIPER bifurcation is accompanied by a change in the number of fixed points. Our findings suggest that near the main diagonal, the limit cycle emerges via a heteroclinic bifurcation, where an orbit connects two saddles lying off the synchronization manifold (not shown). Note that the orbit of the limit cycle follows the unstable manifold of the saddle point FP2 on the synchronization manifold. To the left or the right of the main diagonal, instead of a heteroclinic bifurcation, one finds homoclinic bifurcations, whereby a saddle point, either FP3 or FP4, touches the limit cycle orbit. The schematic phase portraits indicating the stable and unstable manifolds of the fixed points and the limit

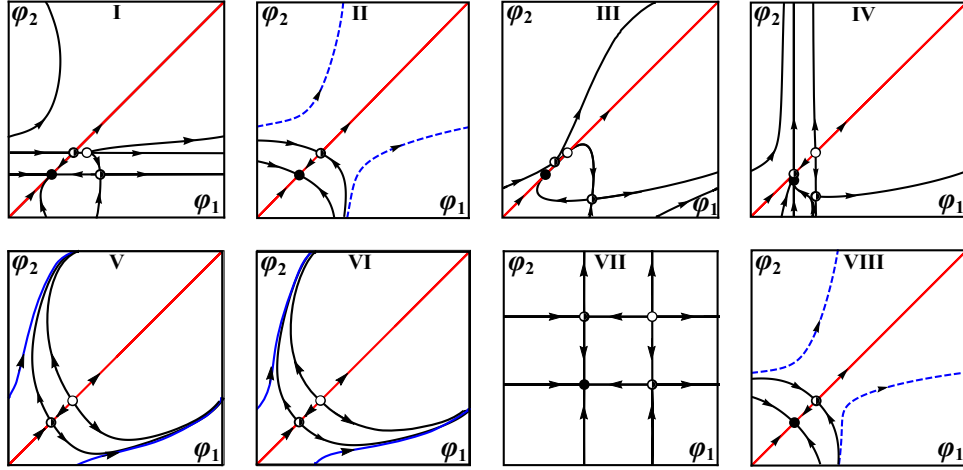


Fig. 5. Schematic phase portraits corresponding to the characteristic regimes of the fast flow. The panels I–VIII refer to representative parameter values indicated in Figure 4b. Also, the stability of fixed points is presented the same way as in Figure 4b. The invariant synchronization manifold is denoted by the red color, whereas the orbit of a stable/unstable limit cycle is indicated by the solid/dashed blue lines.

cycle for the characteristic regimes of the fast flow, denoted by I–VIII in Figure 4b, are illustrated in Figure 5.

The two branches of SNIPER bifurcations may readily be approximated for small values of κ_1 and κ_2 by a simple scheme, which amounts to reducing the fast flow to a normal form of saddle-node bifurcation. Suppose first that $\kappa_1 \ll 1$ and $I_0 - 1 \ll 1$. More specifically, let $\xi \ll 1$ be a small parameter such that $I_0 - 1 = \xi$ (close to the threshold) and $\kappa_1 = \gamma\xi$, i.e. γ is a rescaling parameter of κ_1 , allowing for a zoom in the neighborhood of zero. Then, the steady states are given by the system

$$\begin{aligned} 1 + \xi - \sin \varphi_1 + \xi\gamma \sin(\varphi_2 - \varphi_1) &= 0, \\ 1 + \xi - \sin \varphi_2 + \kappa_2 \sin(\varphi_1 - \varphi_2) &= 0. \end{aligned} \quad (5)$$

The first equation in the zeroth order approximation leads to $\varphi_1 = \pi/2$. Hence, using the perturbation approach, we have

$$\varphi_1^* = \frac{\pi}{2} + \sqrt{\xi}\Psi_1 + \dots; \quad \varphi_2^* = \Psi_2 + \dots, \quad (6)$$

where the $\sqrt{\xi}$ scaling follows from the Taylor expansion of the function $\sin \varphi_1$ at $\pi/2$. Inserting (6) into (5), one obtains the system of equations for Ψ_1 and Ψ_2

$$\begin{aligned} 1 + \frac{1}{2}\Psi_1^2 - \gamma \cos \Psi_2 &= 0, \\ 1 - \sin \Psi_2 + \kappa_2 \cos \Psi_2 &= 0. \end{aligned} \quad (7)$$

From system (7), it is not difficult to see that the saddle-node bifurcation takes place if the condition $1 - \gamma \cos \Psi_2 = 0$ is satisfied. This leads to the parametric representation $\kappa_1 = \xi\gamma = \frac{I_0-1}{\cos \Psi_2}$, $\kappa_2 = \frac{\sin \Psi_2 - 1}{\cos \Psi_2}$, of the saddle-node curve for small κ_1 values, where Ψ_2 plays the role of the parameter along the curve. An analogous approach may be used to capture the second branch of saddle-node bifurcations, cf. the green dashed lines in Figure 4a.

4.2 Dynamics of the slow flow

We have numerically obtained the dynamics of the slow flow by applying a two-step approach. First, for fixed values (κ_1, κ_2) , we determine the time-averaged dynamics of the fast flow (4), $\langle \varphi_2 - \varphi_1 \rangle_t = f(\kappa_1, \kappa_2)$. Here, the averaging $\langle \cdot \rangle_t$ is performed over a sufficiently large time interval, having eliminated a transient. Hence, this average depends on the attractor of the fast flow for the given (κ_1, κ_2) . In particular, if the fast flow possesses a stable fixed point, then $\langle \varphi_2 - \varphi_1 \rangle_t = \varphi_2^* - \varphi_1^*$, where $(\varphi_1^*, \varphi_2^*)$ is a solution of

$$\begin{aligned} I_0 - \sin \varphi_1^* + \kappa_1 \sin(\varphi_2^* - \varphi_1^*) &= 0 \\ I_0 - \sin \varphi_2^* + \kappa_2 \sin(\varphi_1^* - \varphi_2^*) &= 0. \end{aligned} \quad (8)$$

This procedure just results in determining the slow critical manifold of the system. In case when the attractor of the fast flow is periodic, $\langle \varphi_2 - \varphi_1 \rangle_t$ presents the time average over the period. Averaging approximation in case of a periodic attractor of the fast flow constitutes a standard approach [13,25], rather natural for describing the influence of oscillations in the fast flow on the dynamics of the slow flow. At the second stage, the obtained time-averages are substituted into the dynamics of the weights

$$\begin{aligned} \dot{\kappa}_1 &= \epsilon[-\kappa_1 + \sin(f(\kappa_1, \kappa_2) + \beta)] \\ \dot{\kappa}_2 &= \epsilon[-\kappa_2 + \sin(-f(\kappa_1, \kappa_2) + \beta)]. \end{aligned} \quad (9)$$

The system (9) is used to determine the vector field of the slow flow by taking into account only the attractors of the fast flow, such that the vector field associated to each attractor is plotted within its respective stability region, cf. Figure 6.

In regions of the (κ_1, κ_2) plane where there are coexisting stable solutions of the fast flow, the corresponding vector field of the slow flow is given on multiple overlapping sheets, since the value of the average $f(\kappa_1, \kappa_2)$ depends on the initial conditions. In our case, this occurs only in a small region of coexistence between an equilibrium and a stable limit cycle.

One should single out two important features of the slow flow: (i) it exhibits two symmetry-related fixed points in the green and blue regions in Figure 6, and (ii) the slow vector field is pointed in opposite directions close to the boundary between the fast oscillatory regime (orange region) and the steady states of the fast flow (blue, green and white regions). The latter in particular implies that interesting effects occur close to the border of the oscillatory and the steady state regime of the fast flow. Moreover, adding noise gives rise to fluctuations around this boundary, which leads to switching between the quasi-stationary and the fast spiking dynamics. Such effects are studied in more detail within the next section.

5 Switching dynamics

Our main observation in this section is that the interplay of plasticity and noise induces slow stochastic fluctuations (switching dynamics), mediating two qualitatively different scenarios depending on the speed of adaptation. The latter include (i) switching between two modes of *noise-induced* oscillations for slower adaptation (small $\epsilon \simeq 0.01$) and (ii) switching between multiple coexisting attractors of the deterministic dynamics for faster adaptation (intermediate $\epsilon \simeq 0.05$).

In case (i), the impact of noise is twofold: on a short timescale, it gives rise to spiking dynamics, whereas on a long time scale, it induces random transitions between

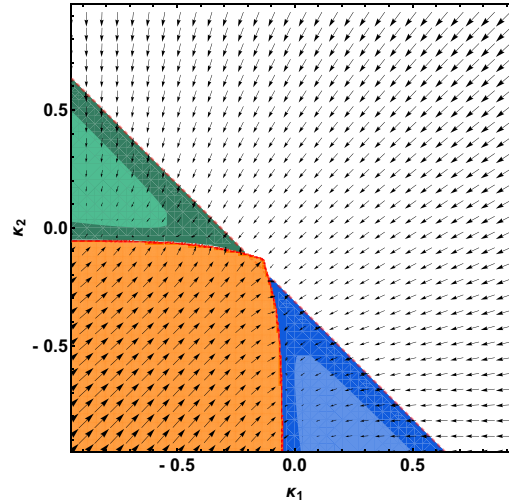


Fig. 6. Vector field of the slow flow obtained by taking into account only stable attractors of the fast flow for $\beta = 4.212$, $I_0 = 0.95$. The color coding is as follows: orange color denotes the region associated to the stable limit cycle of the fast flow, white stands for the stable fixed point of the fast flow FP1, whereas blue and green color correspond to the two stable fixed points FP3 and FP4. Within the light-shaded regions, FP3 and FP4 are foci rather than nodes, cf. Figure 4b.

the two oscillatory modes. In case (ii), the switching dynamics comprises metastable states derived from two fixed points, as well as two limit cycles associated to emergent oscillations of the corresponding deterministic system. The key difference between the effects (i) and (ii) is that for slower adaptation, the system switches between the oscillatory modes that do not exist as deterministic attractors. Moreover, the two generic types of switching are characterized by distinct phase dynamics: for slower adaptation, one finds alternation of patterns with different order of spiking between the units, whereas for faster adaptation, the phases effectively exhibit bursting behavior, involving a succession between episodes of spiking and relative quiescence. An overview on how the typical dynamics of couplings changes with ϵ at fixed β is provided in Figure 7. Note that the difference between the average coupling weights of the stable periodic solutions of the deterministic system are much smaller than a typical distance between the coupling levels for the stationary states. The prevalence of metastable states is affected by ϵ so that intermediate adaptation favors oscillatory modes, whereas the fast adaptation apparently promotes the two quasi-stationary states. In the next two subsections, we provide further insight into the mechanisms behind the switching dynamics using the results of the fast-slow analysis.

5.1 Switching dynamics under slow adaptation

As already indicated, ϵ is here taken sufficiently small, such that it cannot facilitate emergent oscillations in the full system (1). For $\epsilon \simeq 0.01$ and under appropriate noise levels, one observes noise-induced oscillations [26]. The latter arise via a scenario involving a multiple-timescale stochastic bifurcation, whereby noise acts only within the fast subsystem of (1). The onset of oscillations under increasing D occurs in two stages. In the first stage, the phase dynamics gradually exhibits more induced spikes,

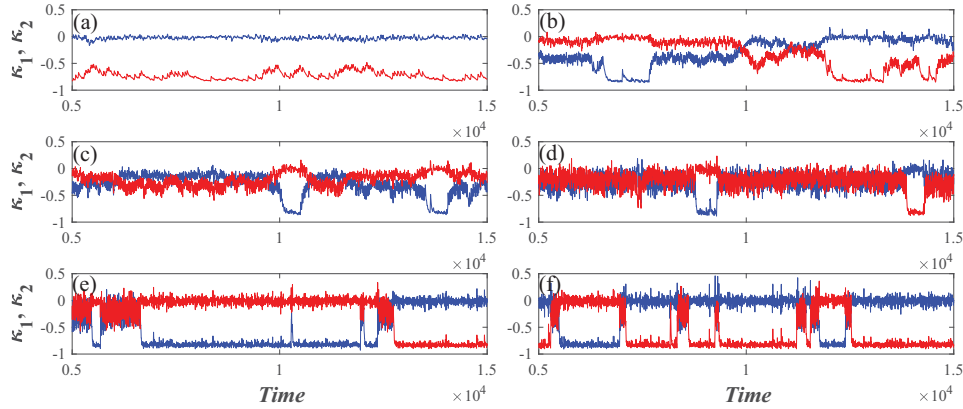


Fig. 7. Switching dynamics under variation of ϵ . The time traces $(\kappa_1(t), \kappa_2(t))$ are obtained for fixed $I_0 = 0.95$, $D = 0.006$, $\beta = 4.212$, whereas ϵ assumes the following values: (a) $\epsilon = 0.008$, (b) $\epsilon = 0.02$, (c) $\epsilon = 0.03$, (d) $\epsilon = 0.06$, (e) $\epsilon = 0.09$, (f) $\epsilon = 0.11$.

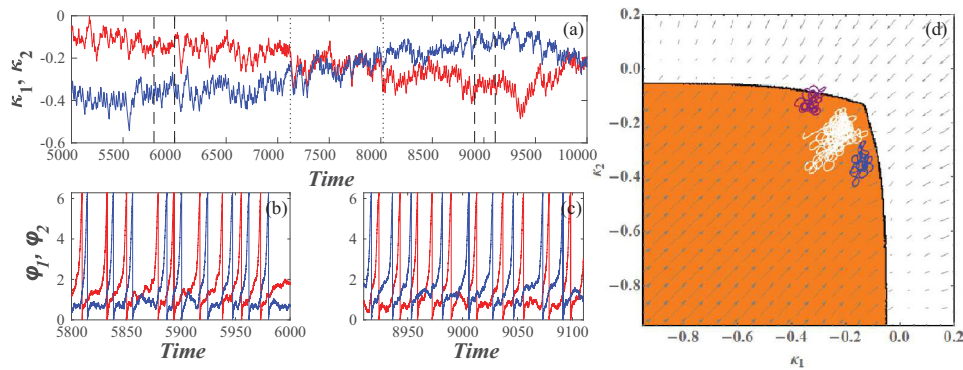


Fig. 8. Switching dynamics between the two modes of noise-induced oscillations. Time traces of the weights are shown in panel (a), whereas panel (b) and (c) display the corresponding time traces of the phases during the intervals between the dashed lines in panel (a). In panel (d), the $(\kappa_1(t), \kappa_2(t))$ projections of the orbits associated to each of the two modes (blue color), as well as the switching episode, shown in white, are superimposed to the vector field of the slow flow from Figure 6. The shaded area corresponds to the stable limit cycle. The system parameters are $I_0 = 0.95$, $\beta = 4.212$, $\epsilon = 0.01$, $D = 0.009$.

such that the stationary distributions of phases eventually acquire a longer tail reflecting the occurrence of spikes (not shown). Nevertheless, the stationary distributions $P(\kappa_i)$ change appreciably only at the second stage, which takes place for sufficiently large D . Such a change accompanies the emergence of coupling oscillations. Note that the system (1) actually exhibits *two modes* of noise-induced oscillations, characterized by the different order of firing between the two units, cf. the time traces of phase dynamics and the associated evolution of couplings in Figure 8a.

It is interesting to examine whether the vector field of the slow flow from Section 4.2 can be used to explain the slow stochastic fluctuations of the coupling weights. To this end, we have superimposed the $(\kappa_1(t), \kappa_2(t))$ orbits of the two noise-induced modes, as well as a switching episode, to a vector field of the slow flow from Figure 6. Note that the orbits typically lie close to the boundary outlining the transition between the two attractors of the fast flow, featuring non-negligible coupling weights. Moreover, the two modes are confined to small areas of the (κ_1, κ_2) plane

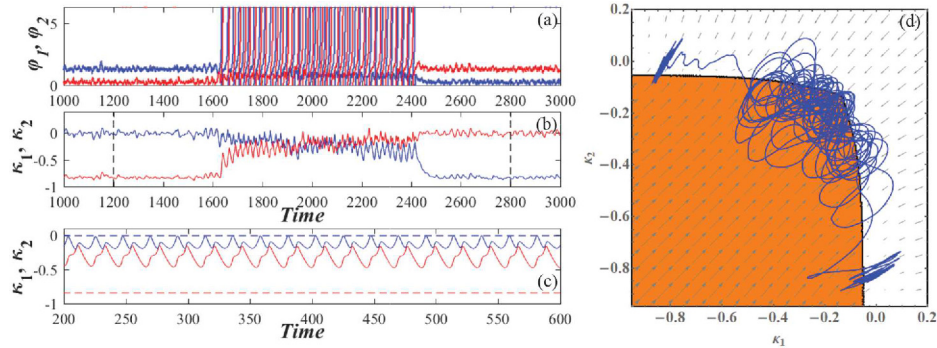


Fig. 9. Time traces of the phases (a) and weights (b) associated to noise-induced switching between the coexisting attractors of the deterministic system. The results are obtained for $I_0 = 0.95$, $\beta = 4.212$, $\epsilon = 0.05$, $D = 0.004$. In panel (c) is provided the deterministic dynamics of weights obtained for the same parameter values. In panel (d), the $(\kappa_1(t), \kappa_2(t))$ orbit corresponding to the interval between the dashed lines in (b) is super-imposed on the vector field of the slow flow cf. Figure 6.

symmetrical with respect to the main diagonal $\kappa_1 = \kappa_2$, whereas the switching episode virtually takes place on the diagonal. Apparently, the noise-induced modes occupy regions where the oscillations in the fast flow emerge via homoclinic bifurcations, rather than the SNIPER scenario. Nonetheless, the switching episode seems to involve the domain featuring coexistence of the two stable sheets of the slow vector field. Within these sheets, which correspond to two attractors of the fast flow (a stable node and a stable limit cycle), the vector fields are oriented in opposite directions, thereby contributing to switching.

5.2 Switching dynamics for faster adaptation

In case of faster adaptation associated to intermediate ϵ , the switching dynamics involves four metastable states, derived from the attractors of the deterministic system. The deterministic multistable behavior includes two symmetry-related stationary states, as well as two symmetry-related limit cycles. Note that while the two stable steady states exist for arbitrary small ϵ and are therefore visible in the slow flow in Figure 6, the oscillatory solutions disappear for small ϵ and hence cannot be observed in the slow flow. The two oscillatory regimes are characterized by the same phase shift, but the reverse order of firing between the two units. Influenced by noise, the phases effectively engage in bursting behavior, manifesting slow stochastic fluctuations between episodes of intensive spiking activity and periods of relative quiescence, see Figure 9a. For a fixed noise level, the prevalence of metastable states, defined by transition probabilities between them, changes with adaptation speed. One observes that for $\epsilon \simeq 0.05$, the oscillatory dynamics is preferred, whereas for $\epsilon \simeq 0.1$, the quasi-stationary states are more ubiquitous.

A comparison of the (κ_1, κ_2) orbits displaying switching dynamics and the vector field of the slow flow from Figure 6 again shows that the former is confined to the criticality region at the boundary between the stationary and oscillatory regimes in the fast flow, cf. Figure 9. One should remark on how the transitions between the different metastable states take place. In particular, from Figure 9b, it is clear that there can be no direct transitions between the two quasi-stationary states, but they rather have to be mediated by the system passing through the oscillatory states. Also, the transition from oscillatory to quasi-stationary states typically occurs

once the couplings approach a master-slave-like configuration, where the coupling in one direction is much stronger than the other one. This scenario coincides with the SNIPER bifurcation of the fast flow described in Section 4.1. The scenario of transition between the two metastable oscillatory states resembles closely the one from Section 5.2.

6 Summary

In the present study, we have analyzed a system of two adaptively coupled active rotators with excitable intrinsic dynamics, demonstrating that the interplay of plasticity and noise may give rise to slow stochastic fluctuations. Two qualitatively different types of self-organized behavior have been identified, depending on the adaptation speed. For slower adaptation, the switching dynamics consists of an alternation between two modes of noise-induced oscillations, associated to a preferred order of spiking between the two units. In this case, noise plays a twofold role: on one hand, it perturbs the excitable local dynamics giving rise to oscillations on a short timescale, whereas on the other hand, it elicits the alternation between the two oscillatory states on a long timescale. The underlying phase dynamics shows slow switching between two patterns distinguished by the different order in which the units are spiking. In case of faster adaptation, the coupling becomes capable of eliciting emergent oscillations in the deterministic system [27]. The latter then exhibits complex multistable behavior, involving two stationary and two oscillatory regimes. Under the influence of noise, the system undergoes switching between these four different metastable states, whose prevalence at fixed noise level depends on the speed of adaptation. The deterministic attractors associated to metastable states are related by the Z_2 symmetry. Thus, a mismatch in excitability parameters would lead to symmetry-breaking, whereby a small mismatch would induce a bias in switching dynamics, whereas a larger mismatch, corresponding to a scenario with one excitable and one oscillatory unit, would completely alter the observed dynamics.

Though the underlying phenomena are not found in the singular limit of infinite scale separation, the fast-slow analysis we have applied still allows one to explain the qualitative features of both considered types of switching behavior. Studying the layer problem, and in particular the vector field of the slow flow, has enabled us to gain insight into the metastable states and the transitions between them. It has been demonstrated that the coupling dynamics is always in a state of “criticality”, being confined to the boundary between the stationary and oscillatory regimes of the fast flow.

Given that excitability, plasticity and noise are inherent ingredients of neuronal systems, the obtained results can be interpreted in the context of neuroscience. It is well known that the backbone of neural networks is made up of binary and ternary neuron motifs, whereby the structural motifs typically support multiple functional motifs, essentially characterized by the weight configuration and the underlying direction of the information flow. With this in mind, the scenario of switching under slow adaptation may be important, because it implies that a binary motif can display slow alternation between two effectively unidirectional weight configurations, promoting opposite direction of information flow. For faster adaptation, one finds multistability between unidirectional coupling and bidirectional coupling of moderate strength. Nonetheless, the underlying phase dynamics, if extended to networks, may be considered as a paradigm for UP-DOWN states, typical for cortical dynamics [28,29]. Thus, it would be of interest to examine the impact of plasticity in networks of noisy excitable units, where one may expect different types of emergent behavior, such as cluster, non-synchronized and partially synchronized states, depending on the frustration of local dynamics and the impact of noise.

We thank S. Eydam for useful discussions. This work was supported by the Ministry of Education, Science and Technological Development of Republic of Serbia under project No. 171017, the DAAD Serbia-Germany Bilateral Project “Emergent Dynamics in Systems of Coupled Excitable Units”, as well as the DFG within the framework of Collaborative Research Center SFB 910.

Author contribution statement

I.F. and S.Y. conceived the model and defined the analysis of noise-induced switching as the main goal of the research. S.Y. and M.W. developed the general framework to investigating the deterministic fast-slow problem and the bifurcation analysis of the associated reduced systems. I.B. obtained all the numerical results, whereas I.B. and I.F. carried out the bifurcation analysis, identified the two types of noise-induced switching behavior and made the main contribution to writing the manuscript. All the authors discussed the findings and participated in interpretation of the results.

References

1. F. Sorrentino, E. Ott, Phys. Rev. Lett. **100**, 114101 (2008)
2. F. Vazquez, V.M. Eguiluz, M.S. Miguel, Phys. Rev. Lett. **100**, 108702 (2008)
3. N. Caporale, Y. Dan, Ann. Rev. Neurosci. **31**, 25 (2008)
4. C. Furusawa, K. Kaneko, Phys. Rev. Lett. **90**, 088102 (2003)
5. D.O. Hebb, *The Organization of Behavior: a Neuropsychological Approach* (John Wiley & Sons, New York, 1949)
6. S. Song, K.D. Miller, L.F. Abbott, Nat. Neurosci. **3**, 919 (2000)
7. R.C. Froemke, Y. Dan, Nature (London) **416**, 433 (2002)
8. H.-X. Wang, R.C. Gerkin, D.W. Nauen, G.-Q. Bi, Nat. Neurosci. **8**, 187 (2005)
9. O. Sporns, R. Kotter, PLoS Biol. **2**, e369 (2004)
10. I. Franović, V. Miljković, Chaos Soliton. Fract. **44**, 122 (2011)
11. I. Franović, V. Miljković, Chaos Soliton. Fract. **45**, 527 (2012)
12. I. Franović, V. Miljković, EPL **92**, 68007 (2011)
13. L. Lübben, O.V. Popovych, P.A. Tass, S. Yanchuk, Phys. Rev. E **93**, 032210 (2016)
14. Y.L. Maistrenko, B. Lysyansky, C. Hauptmann, O. Burylko, P.A. Tass, Phys. Rev. E **75**, 066207 (2007)
15. P. Seliger, S.C. Young, L.S. Tsimring, Phys. Rev. E **65**, 041906 (2002)
16. M. Li, S. Guan, C.-H. Lai, New J. Phys. **12**, 103032 (2010)
17. P.S. Skardal, D. Taylor, J.G. Restrepo, Physica D **267**, 27 (2014)
18. D. Kasatkin, S. Yanchuk, E. Schöll, V. Nekorkin, Phys. Rev. E **96**, 062211 (2017)
19. O.V. Popovych, S. Yanchuk, P.A. Tass, Sci. Rep. **3**, 2926 (2013)
20. K. Mikkelsen, A. Imparato, A. Torcini, Phys. Rev. Lett. **110**, 208101 (2013)
21. D. Millman, S. Mihalas, A. Kirkwood, E. Niebur, Nat. Phys. **6**, 801 (2010)
22. A. Levina, J.M. Hermann, T. Geisel, Phys. Rev. Lett. **102**, 118110 (2009)
23. T. Aoki, T. Aoyagi, Phys. Rev. Lett. **102**, 034101 (2009)
24. T. Aoki, T. Aoyagi, Phys. Rev. E **84**, 066109 (2011)
25. A. Shilnikov, Int. J. Bifurc. Chaos **18**, 2141 (2008)
26. S.-J. Wang, G. Ouyang, J. Guang, M. Zhang, Phys. Rev. Lett. **116**, 018101 (2016)
27. Q. Ren, K.M. Kolwankar, A. Samal, J. Jost, Phys. Rev. E **86**, 056103 (2012)
28. T.T.G. Hahn, J.M. McFarland, S. Berberich, B. Sakmann, M.R. Mehta, Nat. Neurosci. **15**, 1531 (2012)
29. V.V. Vyazovskiy, K.D. Harris, Nat. Rev. Neurosci. **14**, 443 (2013)

Inverse stochastic resonance in a system of excitable active rotators with adaptive coupling

IVA BAČIĆ¹, VLADIMIR KLINSHOV², VLADIMIR NEKORKIN², MATJAŽ PERC³ and IGOR FRANOVIĆ^{1(a)}

¹ *Scientific Computing Laboratory, Center for the Study of Complex Systems, Institute of Physics Belgrade, University of Belgrade - Pregrevica 118, 11080 Belgrade, Serbia*

² *Institute of Applied Physics of the Russian Academy of Sciences - 46 Ulyanov Street, 603950 Nizhny Novgorod, Russia*

³ *Faculty of Natural Sciences and Mathematics, University of Maribor - Koroška cesta 160, SI-2000 Maribor, Slovenia*

received 17 September 2018; accepted in final form 8 November 2018
published online 11 December 2018

PACS 05.40.Ca – Noise

PACS 87.19.1n – Oscillations and resonance

Abstract – Inverse stochastic resonance is a phenomenon where an oscillating system influenced by noise exhibits a minimal oscillation frequency at an intermediate noise level. We demonstrate a novel generic scenario for such an effect in a multi-timescale system, considering an example of emergent oscillations in two adaptively coupled active rotators with excitable local dynamics. The impact of plasticity turns out to be twofold. First, at the level of multiscale dynamics, one finds a range of intermediate adaptivity rates that give rise to multistability between the limit cycle attractors and the stable equilibria, a condition necessary for the onset of the effect. Second, applying the fast-slow analysis, we show that the plasticity also plays a facilitatory role on a more subtle level, guiding the fast flow dynamics to parameter domains where the stable equilibria become focuses rather than nodes, which effectively enhances the influence of noise. The described scenario persists for different plasticity rules, underlying its robustness in the light of potential applications to neuroscience and other types of cell dynamics.

Copyright © EPLA, 2018

Introduction. – Noise in coupled excitable or bistable systems may induce two types of generic effects [1]. On the one hand, it can modify the deterministic behavior by acting non-uniformly on different states of the system, thus amplifying or suppressing some of its features. On the other hand, noise may give rise to completely novel forms of behavior, typically based on crossing the thresholds or separatrices, or involving enhanced stability of deterministically unstable structures. In neuronal systems, the constructive role of noise at different stages of information processing, referred to as “stochastic facilitation” [2,3], mainly comprises resonant phenomena. A classical example is the stochastic resonance [4], which allows for the detection of weak subthreshold periodic signals. A more recent development concerns the effect of inverse stochastic resonance (ISR) [3,5–12], where noise selectively reduces the spiking frequency of neuronal oscillators, converting the tonic firing into intermittent bursting-like activity or a short-lived transient followed

by a long period of quiescence. The name of the effect should be taken *cum grano salis*, because in contrast to stochastic resonance, it involves no additional external signal: one rather observes a non-monotonous dependence of the spiking rate on noise variance, whereby the oscillation frequency becomes minimal at a preferred noise level. Such an inhibitory effect of noise has recently been shown for cerebellar Purkinje cells [11], having explicitly demonstrated how the lifetimes of the spiking (“up”) and the silent (“down”) states [13–15] are affected by the noise variance. ISR has been indicated to play important functional roles in neuronal systems, including the reduction of spiking frequency in the absence of neuromodulators, suppression of pathologically long short-term memories, triggering of on-off tonic spiking activity and even optimization of information transfer along the signal propagation pathways [3,7,9,11].

So far, theoretical studies on ISR have mostly concerned the scenario where a single neuron exhibits bistable deterministic dynamics, featuring coexistence between a limit cycle and a stable equilibrium. Such bistability is

^(a)E-mail: franovic@ipb.ac.rs

typical for Type-II neurons below the subcritical Hopf bifurcation, *e.g.*, classical Hodgkin-Huxley and Morris-Lecar models [3,6–8]. There, applying noise induces switching between the metastable states, but at an intermediate noise level, one surprisingly finds a strong asymmetry of the associated switching rates, which makes the periods spent in the vicinity of equilibrium much longer than the periods of spiking activity.

An important open problem concerns conditions giving rise to ISR in coupled excitable systems, where noise influences the emergent oscillations. Here we address in detail this issue, as it may be crucial to understanding the prevalence of the effect in neural networks, whose activity depends on the interplay of excitability, coupling properties and noise. Synaptic dynamics typically involves the plasticity feature, which makes self-organization in neuronal systems a multi-timescale process: the short-term spiking activity unfolds on a quasi-static coupling configuration, while the slow adjustment of coupling weights depends on the time-averaged evolution of units.

Motivated by the findings in neuroscience, we focus on the onset of ISR in a simplified, yet paradigmatic system of two adaptively coupled stochastic active rotators with excitable local dynamics. Active rotators are canonical for Type-I excitability and may be seen as equivalent to the theta-neuron model. Adaptivity is introduced in a way that allows continuous interpolation between a spectrum of plasticity rules, including Hebbian learning and spike-time-dependent plasticity (STDP) [16–18].

We demonstrate a generic scenario for the plasticity-induced ISR, where the system’s multiscale structure, defined by the adaptivity rate, plays a crucial role. On a basic level, plasticity gives rise to multistable behavior involving coexisting stationary and oscillatory regimes. An additional subtlety, which we show by the fast-slow analysis, is that the plasticity promotes the resonant effect by guiding the fast flow toward the parameter region where the stable fixed points are focuses rather than nodes.

The paper is organized as follows. In the next section the details of the model and the numerical bifurcation analysis of the deterministic dynamics are presented. The third section contains the results on the ISR effect and the supporting conditions. In the fourth section the fast-slow analysis is applied to explain the mechanism by which plasticity enhances the system’s non-linear response to noise. Apart from providing a brief summary, in the last section we also discuss the prevalence of the observed effect.

Model and bifurcation analysis of deterministic dynamics. – Our model involves two stochastic active rotators interacting by adaptive couplings [19–22],

$$\begin{aligned}\dot{\varphi}_1 &= I_0 - \sin \varphi_1 + \kappa_1 \sin(\varphi_2 - \varphi_1) + \sqrt{D}\xi_1(t), \\ \dot{\varphi}_2 &= I_0 - \sin \varphi_2 + \kappa_2 \sin(\varphi_1 - \varphi_2) + \sqrt{D}\xi_2(t), \\ \dot{\kappa}_1 &= \epsilon(-\kappa_1 + \sin(\varphi_2 - \varphi_1 + \beta)), \\ \dot{\kappa}_2 &= \epsilon(-\kappa_2 + \sin(\varphi_1 - \varphi_2 + \beta)),\end{aligned}\quad (1)$$

where the phases $\{\varphi_1, \varphi_2\} \in S^1$, while the coupling weights $\{\kappa_1, \kappa_2\}$ are real variables.

The excitability parameters I_0 , which one may interpret as external bias currents in the context of neuroscience, are assumed to be identical for both units. For such a setup, the deterministic version of (1) possesses a Z_2 symmetry, being invariant to the exchange of units’ indices. The uncoupled units undergo a SNIPER bifurcation at $I_0 = 1$, with the values $I_0 < 1$ ($I_0 > 1$) corresponding to the excitable (oscillatory) regime. We consider the case of excitable local dynamics, keeping $I_0 = 0.95$ fixed throughout the paper, such that the oscillations may emerge only due to the coupling terms and/or noise. The scale separation between the fast dynamics of the phases and the slow dynamics of adaptation is adjusted by the parameter $\epsilon \ll 1$. The fast variables are influenced by independent white noise of variance D such that $\xi_i(t)\xi_j(t') = \delta_{ij}\delta(t-t')$ for $i, j \in \{1, 2\}$. Conceptually, adding stochastic input to the fast variables embodies the action of synaptic noise in neuronal systems [23].

The modality of the plasticity rule is specified by the parameter β , whose role may be understood by invoking the qualitative analogy between the adaptation dynamics in classical neuronal systems and the systems of coupled phase oscillators. This issue has first been addressed in [24–26], and a deeper analysis of the correspondence between the phase-dependent plasticity rules and the STDP has been carried out in [19]. In particular, it has been shown that the plasticity dynamics for $\beta = 3\pi/2$, where the stationary weights between the oscillators with smaller/larger phase differences increase/decrease, qualitatively resembles the Hebbian learning rule [25,26]. Nevertheless, when $\beta = \pi$, the coupling weights encode a causal relationship between the spiking of oscillators by changing in the opposite directions, in analogy to an STDP-like plasticity rule. Our interest lies with the β interval interpolating between these two limiting cases.

Using bifurcation analysis of the deterministic dynamics of (1), we first show how the modality of the plasticity rule influences the number of stationary states, and then explain how the onset of oscillations depends on adaptivity rate. The bifurcation diagram in fig. 1 indicates that the number and the stability of fixed points of (1) change with β in such a way that the system may possess two, four or six fixed points. Due to invariance to Z_2 symmetry, one always finds pairs of solutions sharing the same stability features. We consider the plasticity rules described by $\beta \in (3.298, 4.495)$, cf. the shaded region in fig. 1, where the system has two stable fixed points lying off the synchronization manifold $\varphi_1 = \varphi_2$, as well as four unstable fixed points. The bifurcations occurring at the boundaries of the relevant β interval are as follows. At $\beta = 3.298$, the system undergoes a supercritical symmetry-breaking pitchfork bifurcation giving rise to a pair of stable fixed points off the synchronization manifold. For $\beta = 4.495$, this pair of stable fixed points collides with a pair of unstable fixed points off

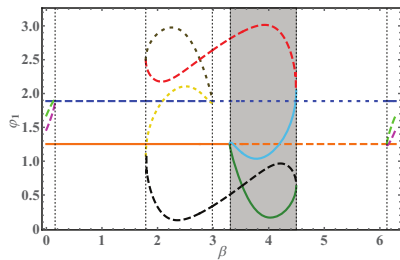


Fig. 1: (Color online) Bifurcation diagram for the fixed points of (1) with $D = 0$ under variation of β . Solid lines refer to stable fixed points, while dashed and dotted lines correspond to saddles of unstable dimension 1 and 2, respectively. Shading indicates the considered range of plasticity rules. The two fixed points independent on β belong to the synchronization manifold. The remaining parameters are $I_0 = 0.95, \epsilon = 0.05$.

the synchronization manifold, getting annihilated in two symmetry-related inverse fold bifurcations. Note that the weight levels typical for the two stable stationary states support effective unidirectional interaction, in a sense that one unit exerts a much stronger impact on the dynamics of the other unit than vice versa. When illustrating the effect of ISR, we shall mainly refer to the case $\beta = 4.2$. For this β , the two stable focuses of (1) at $D = 0$ are given by $(\varphi_1, \varphi_2, \kappa_1, \kappa_2) = (1.177, 0.175, 0.032, -0.92)$ and $(\varphi_1, \varphi_2, \kappa_1, \kappa_2) = (0.175, 1.177, -0.92, 0.032)$. Within the considered β interval, the two stable fixed points of the coupled system exhibit excitable behavior, responding to external perturbation by generating either the successive spikes or synchronized spikes [21].

The onset of oscillations for the deterministic version of (1) relies on the interplay between the plasticity rule, controlled by β , and the adaptation rate, characterized by ϵ . In fig. 2(a) are shown the results of parameter sweep indicating the variation of κ_1 variable, $\sigma_{\kappa_1} = \max(\kappa_1(t)) - \min(\kappa_1(t))$, within the (β, ϵ) parameter plane. The sweep indicates the maximal stability region of the two emerging periodic solutions, related by the exchange symmetry of units indices. The data are obtained by numerical continuation starting from a stable periodic solution, such that the final state reached for the given parameter set is used as initial conditions of the system dynamics for incremented parameter values. One observes that for fixed β , there exists an interval of timescale separation ratios $\epsilon \in (\epsilon_{min}, \epsilon_{max})$ admitting oscillations, see fig. 2(b). Within the given ϵ range, the system exhibits multistability where periodic solutions coexist with the two symmetry-related stable stationary states. The lower threshold for oscillations, ϵ_{min} , reduces with β , whereas the upper boundary value, ϵ_{max} , is found to grow as β is enhanced. Note that the waveform of oscillations also changes as ϵ is increased under fixed β . In particular, for smaller ϵ , the waveforms corresponding to the two units are rather different. Nevertheless, around $\epsilon \approx 0.06$ the system undergoes a pitchfork bifurcation of limit cycles, such that

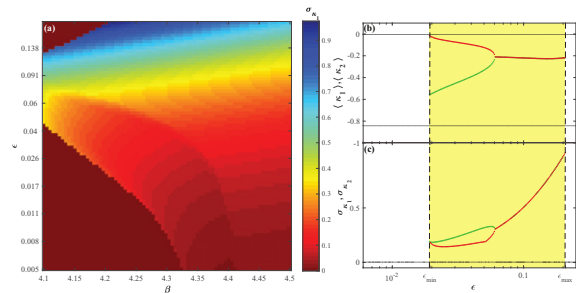


Fig. 2: (Color online) Onset of oscillations in (1) for $D = 0$. (a) Variation σ_{κ_1} of the coupling weight κ_1 in the (β, ϵ) -plane. (b) Mean coupling weights $\langle \kappa_1 \rangle(\epsilon)$ and $\langle \kappa_2 \rangle(\epsilon)$ for oscillatory (thick lines) and stationary states (thin lines) at $\beta = 4.2$. (c) Variation $\sigma_{\kappa_1}(\epsilon)$ and $\sigma_{\kappa_2}(\epsilon)$, presented as in (b). Shading in (b) and (c) indicates the ϵ interval admitting the stable periodic solutions.

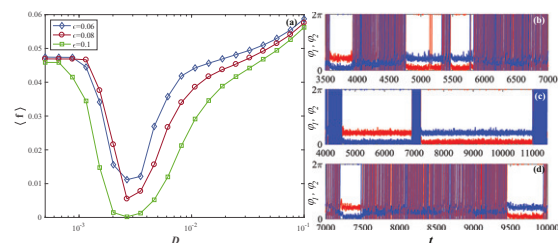


Fig. 3: (Color online) (a) Mean spiking rate $\langle f \rangle$ in terms of D for $\epsilon \in \{0.06, 0.08, 0.1\}$. The curves exhibit a characteristic minimum at an intermediate noise level. (b)–(d) Time traces $\varphi_1(t)$ and $\varphi_2(t)$ for noise levels below, at and above the resonant value. The remaining parameters are $I_0 = 0.95, \beta = 4.2, \epsilon = 0.06$.

the oscillatory solution gains the anti-phase space-time symmetry $\varphi_1(t) = \varphi_2(t + T/2), \kappa_1(t) = \kappa_2(t + T/2)$, where T denotes the oscillation period [21].

Numerical results on ISR. – Inverse stochastic resonance manifests itself as noise-mediated suppression of oscillations, whereby the frequency of noise-perturbed oscillations becomes minimal at a preferred noise level. For system (1), we find such an effect to occur generically for intermediate adaptivity rates, supporting multistability between the stationary and the oscillatory solutions, as described in the previous section. A family of curves describing the dependence of the oscillation frequency on noise variance $\langle f \rangle(D)$ for different ϵ values is shown in fig. 3. All the curves corresponding to $\epsilon \geq \epsilon_{min}(\beta)$ show a characteristic non-monotonous behavior, displaying a minimum at the optimal noise intensity. For weaker noise, the oscillation frequency remains close to the deterministic one, whereas for much stronger noise, the frequency increases above that of unperturbed oscillations. The displayed results are obtained by averaging over an ensemble of 1000 different stochastic realizations, having excluded the transient behavior, and having fixed a single set of initial conditions within the basin of attraction of the limit cycle attractor. Nevertheless, we have verified that the

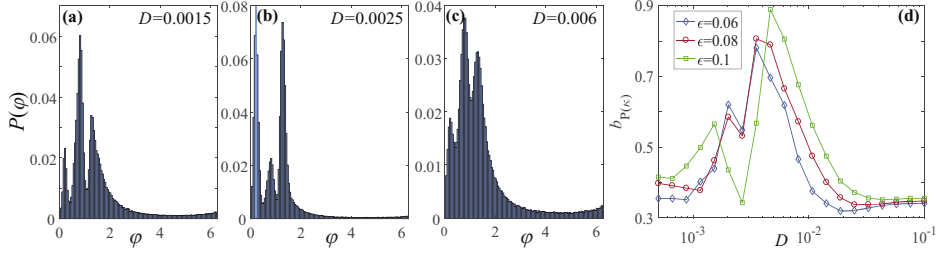


Fig. 4: (Color online) (a)–(c) Stationary distribution $P(\varphi_1)$ for the noise levels below, at and above the resonant value. System parameters are $I_0 = 0.95$, $\beta = 4.2$ and $\epsilon = 0.06$. From the three observable peaks, the middle one, prevalent in (a) and (c), refers to the metastable state associated to the oscillatory mode of (1) for $D = 0$. The two lateral peaks, dominant in (b), correspond to quasi-stationary states derived from the stable equilibria of the deterministic version of (1). (d) Bimodality coefficient for the stationary distribution of κ_1 , $b_{P(\kappa_1)}$, as a function of D . The three curves refer to $\epsilon = 0.06$ (diamonds), $\epsilon = 0.08$ (circles) and $\epsilon = 0.1$ (squares).

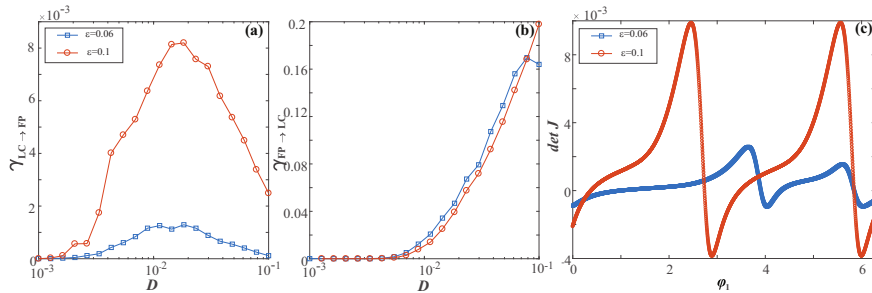


Fig. 5: (Color online) (a) and (b): transition rates from the stability basin of the limit cycle to the fixed point, $\gamma_{LC \rightarrow FP}(D)$ and vice versa, $\gamma_{FP \rightarrow LC}(D)$, numerically obtained for $\epsilon = 0.06$ (squares) and $\epsilon = 0.1$ (circles). The remaining parameters are $I_0 = 0.95$, $\beta = 4.2$. (c) Determinant of the Jacobian calculated along the limit cycle orbit as a function of the phase variable. The quantity provides an indication of the sensitivity of certain sections of the orbit to external perturbation. Blue and red colors correspond to $\epsilon = 0.06$ and $\epsilon = 0.1$, respectively.

qualitatively analogous results are obtained if for each realization of stochastic process one selects a set of random initial conditions lying within the stability basin of the periodic solution. The suppression effect of noise depends on the adaptivity rate, and is found to be more pronounced for faster adaptivity. Indeed, for smaller ϵ , $\varphi(t)$ series corresponding to the noise levels around the minimum of $\langle f \rangle(D)$ exhibit bursting-like behavior, whereas for larger ϵ , noise is capable of effectively quenching the oscillations, such that the minimal observed frequency approaches zero.

The core of the described effect concerns switching dynamics between the metastable states associated to coexisting attractors of the deterministic version of system (1). To illustrate this, in fig. 4 we have considered the stationary distributions of one of the phase variables, $P(\varphi)$, for the noise levels below, at and above the minimum of the $\langle f \rangle(D)$, having fixed the remaining parameters to $(\beta, \epsilon) = (4.2, 0.06)$. The distribution $P(\varphi)$ is characterized by two lateral peaks, reflecting the two symmetry-related quasi-stationary states, and the area around the central peak, corresponding to the oscillatory mode. For small noise $D = 0.0015$, see fig. 4(a), and very large noise $D = 0.006$, cf. fig. 4(c), the central peak of $P(\varphi)$ is expectedly prevalent compared to the two lateral peaks. Nevertheless, the switching dynamics for

$D = 0.0025$, the noise level about the minimum of $\langle f \rangle(D)$, is fundamentally different, and the corresponding distribution $P(\varphi)$ in fig. 4(b) shows that the system spends much more time in the quasi-stationary states than performing the oscillations. The onset of ISR in the dynamics of fast variables is accompanied by the increased bimodality of the stationary distribution of the couplings, see fig. 4(d).

In order to observe the non-monotonous response of the system's frequency to noise, the geometry of the phase space has to be asymmetrical with respect to the separatrix between the coexisting attractors in such a way that the limit cycle attractor lies much closer to the separatrix than the stationary states. Such structure of phase space gives rise to asymmetry in switching dynamics, whereby at the preferred noise level around the minimum of $\langle f \rangle(D)$, the transition rate from the stability basin of the limit cycle attractor to that of stationary states $\gamma_{LC \rightarrow FP}$ becomes much larger than the transition rate in the inverse direction, $\gamma_{FP \rightarrow LC}$. Figures 5(a) and (b) corroborate that the dependences $\gamma_{LC \rightarrow FP}(D)$ and $\gamma_{FP \rightarrow LC}(D)$ are qualitatively distinct: the former displays a maximum at the resonant noise level, whereas the latter just increases monotonously with noise. The fact that ISR is more pronounced for higher adaptivity rates is reflected in that the curve $\gamma_{LC \rightarrow FP}(D)$ for $\epsilon = 0.1$ lies substantially above that for $\epsilon = 0.06$, see fig. 5(a).

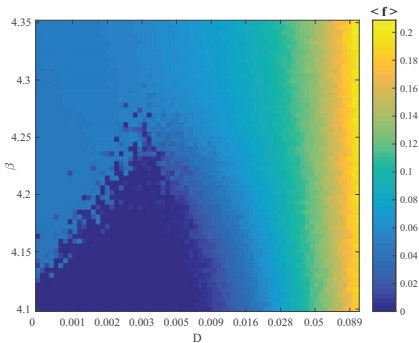


Fig. 6: (Color online) Mean spiking rate $\langle f \rangle$ as a function of β and D for fixed $\epsilon = 0.05$. The results evince the robustness of the ISR effect with respect to different plasticity rules.

To understand why the interplay of adaptivity rate and noise yields a stronger resonant effect for larger ϵ , we have investigated the susceptibility of the limit cycle attractor to external perturbation. In particular, fig. 5(c) shows how the determinant of the Jacobian calculated along the limit cycle orbit change for $\epsilon = 0.06$ (blue line) and $\epsilon = 0.1$ (red line), respectively. For smaller ϵ , one may identify two particular points where the determinant of the Jacobian is the largest, *i.e.*, where the impact of external perturbation is felt the strongest. This implies that noise is most likely to drive the systems trajectory away from the limit cycle attractor around these two sections of the orbit, which should lie closest to the boundary to the stability basins of the stationary states. Such a physical picture is maintained for larger ϵ , but one should stress that the sensitivity of limit cycle attractor to external perturbation substantially increases along the entire orbit, cf. fig. 5(c). In other words, faster adaptivity enhances the impact of noise, contributing to a more pronounced ISR effect. This point is addressed from another perspective in the next section.

We also examine the robustness of ISR to different modalities of the plasticity rule specified by β . Figure 6 shows how the average oscillation frequency changes with β and D for fixed $\epsilon = 0.05$. The non-linear response to noise, conforming to a resonant effect with a minimum of oscillation frequency at an intermediate noise level, persists in a wide range of β , essentially interpolating between the Hebbian-like and the STDP-like adaptive dynamics.

Fast-slow analysis: role of plasticity in the resonant effect. – Though ISR is observed for intermediate ϵ , here we show that the fast-slow analysis may still be applied to demonstrate a peculiar feature of the mechanism behind the resonant effect. In particular, we find that the plasticity enhances the resonant effect by driving the fast flow dynamics toward the parameter domain where the stationary state is a focus rather than a node. It is well known that the response to noise in multi-timescale systems qualitatively depends on the character of stationary states. Indeed, by using the sample-paths approach and other advanced techniques, it has already been shown

that such systems may exhibit fundamentally different scaling regimes with respect to noise variance and the scale-separation ratio [27,28]. Moreover, the resonant effects may typically be expected in the case in which quasi-stationary states are focuses [27], essentially because the local dynamics around the stationary state then involves an eigenfrequency.

Within the standard fast-slow analysis, one may either consider the layer problem, defined on the fast timescale, or the reduced problem, concerning the slow timescale [29]. For the layer problem, the fast flow dynamics $\varphi_1(t; \kappa_1, \kappa_2), \varphi_2(t; \kappa_1, \kappa_2)$ is obtained by treating the slow variables κ_1 and κ_2 as system parameters, whereas in the case of the reduced problem, determining the dynamics of the slow flow $(\kappa_1(t), \kappa_2(t))$ involves time-averaging over the stable regimes of the fast flow of the layer problem. The fast flow can in principle exhibit several attractors, which means that multiple stable sheets of the slow flow may emerge from the averaged dynamics on the different attractors of the fast flow. Our key point concerns the dynamics of the slow flow, which requires us to first classify the attractors of the fast flow.

The fast flow dynamics is given by

$$\begin{aligned}\dot{\varphi}_1 &= I_0 - \sin \varphi_1 + \kappa_1 \sin(\varphi_2 - \varphi_1), \\ \dot{\varphi}_2 &= I_0 - \sin \varphi_2 + \kappa_2 \sin(\varphi_1 - \varphi_2),\end{aligned}\quad (2)$$

where $\kappa_1, \kappa_2 \in [-1, 1]$ are considered as additional system parameters. One may formally obtain (2) by setting $\epsilon = 0$ in (1) with $D = 0$. We find that the fast flow is monostable for most of the (κ_1, κ_2) values, exhibiting either a stable equilibrium or a limit cycle attractor, see fig. 7(a). In general, the fast flow admits either two or four fixed points, and a more detailed physical picture, including the associated bifurcations, is presented in [21]. The stability region of the oscillatory regime, outlined by the red color, has been calculated by numerical continuation starting from a stable periodic solution. Bistability between a stable fixed point and a limit cycle is observed only in a small area near the main diagonal $\kappa_1 = \kappa_2$. Within the region featuring oscillatory regime, each periodic solution obtained for (κ_1, κ_2) above the main diagonal has a Z_2 symmetry-related counterpart below the diagonal. Typically, the periodic solutions emanate from SNIPER bifurcations, which make up two branches where either κ_1 or κ_2 are almost constant and close to zero.

Using the results from the analysis of the layer problem, our goal is to determine the vector fields corresponding to the stable sheets of the slow flow. We have numerically obtained the dynamics of the slow flow by a standard two-step approach [19,30]. First, for fixed values (κ_1, κ_2) , we have determined the time-averaged dynamics of the fast flow (2), $\langle \varphi_2 - \varphi_1 \rangle_t = h(\kappa_1, \kappa_2)$, whereby the averaging $\langle \cdot \rangle_t$ is carried out over a sufficiently long time interval, having excluded the transient behavior. As already indicated, such an average depends on the attractor of the fast flow for the given (κ_1, κ_2) . If the fast flow possesses

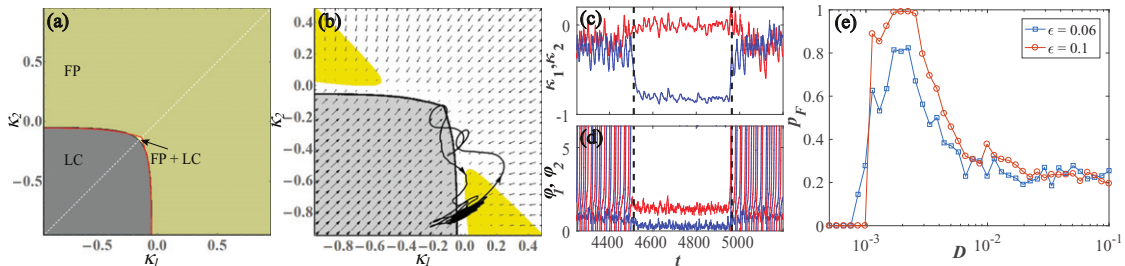


Fig. 7: (Color online) (a) Attractors of the fast flow (2) in terms of κ_1 and κ_2 , now treated as free parameters. The fast flow is typically monostable, admitting either a stable fixed point (FP) or a stable limit cycle (LC), apart from a small region of bistability (FP+LC) around the main diagonal. (b) Vector field of the slow flow (3) determined by considering only the stable regimes of the fast flow for $\beta = 4.2, I_0 = 0.95$. Within the yellow-highlighted regions, the stable fixed point of the fast flow is a focus rather than the node. The displayed orbit $(\kappa_1(t), \kappa_2(t))$ corresponds to a switching episode from the oscillatory state to the quasi-stationary state and back (evolution direction indicated by arrows). Panels (c) and (d) show the time traces of phases and couplings during the switching episode. (e) Conditional probability $p_F(D)$ for $\epsilon = 0.06$ (blue squares) and $\epsilon = 0.1$ (red circles).

a stable fixed point, then $\langle \varphi_2 - \varphi_1 \rangle_t = \varphi_2^* - \varphi_1^*$, which corresponds to the slow critical manifold of the system. For (κ_1, κ_2) where the attractor of the fast flow is a periodic solution, $\langle \varphi_2 - \varphi_1 \rangle_t$ amounts to the time average over the period. Averaging over a periodic attractor of the fast flow is a standard approximation [30], quite natural when describing the influence of oscillations in the fast flow to the dynamics of the slow flow.

As the second step, the obtained time averages are substituted into the coupling dynamics

$$\begin{aligned} \dot{\kappa}_1 &= \epsilon[-\kappa_1 + \sin(h(\kappa_1, \kappa_2) + \beta)], \\ \dot{\kappa}_2 &= \epsilon[-\kappa_2 + \sin(-h(\kappa_1, \kappa_2) + \beta)]. \end{aligned} \quad (3)$$

The system (3) allows one to determine the vector fields on the stable sheets of the slow flow, which correspond to the attractors of the fast flow. In fig. 7(b), the vector fields associated to each of the attractors (fixed point or limit cycle) are presented within its respective (κ_1, κ_2) stability region. In the small region of the (κ_1, κ_2) -plane supporting coexisting stable solutions of the fast flow, the corresponding vector field of the slow flow is given on multiple overlapping sheets, since the value of the average $f(\kappa_1, \kappa_2)$ depends on the initial conditions.

Within the above framework, one is able to explain a subtle influence of adaptivity on the mechanism behind the ISR. To this end, in fig. 7(b) we have projected a typical example of the $(\kappa_1(t), \kappa_2(t))$ trajectory of the full system (1) corresponding to a switching episode between the metastable states associated to a limit cycle attractor and a stable equilibrium of the deterministic system, see the time traces in figs. 7(c), (d). One observes that for the oscillating regime, the coupling dynamics always remains close to the SNIPER bifurcation of the fast flow, cf. fig. 7(a), which makes the oscillations quite susceptible to noise. Recall that the fast flow is typically monostable. Thus, switching events in the full system are naturally associated to the fast flow undergoing the SNIPER bifurcation: either a direct one, leading from the oscillatory to the stationary regime, or the inverse one, unfolding in the

opposite direction. For (κ_1, κ_2) values immediately after the SNIPER bifurcation toward the quiescent state, the stable equilibrium of the fast flow is a node. Nevertheless, for the noise levels where the effect of ISR is most pronounced, we find that the coupling dynamics guides the system into the region where the equilibrium is a stable focus rather than a node, see the yellow highlighted region in fig. 7(b). We have verified that this feature is a hallmark of the resonant effect by numerically calculating the conditional probability p_F that the events of crossing the SNIPER bifurcation are followed by the system's orbit visiting the (κ_1, κ_2) region where the stable equilibrium is a focus. The $p_F(D)$ dependences for two characteristic ϵ values at fixed $\beta = 4.2$ are plotted in fig. 7(e). One learns that $p_F(D)$ has a maximum for the resonant noise levels, where the corresponding curve $f(D)$ displays a minimum. In other words, the fact that the coupling dynamics drives the fast flow to the focus-associated regions of the (κ_1, κ_2) -plane results in trapping the phase variables for a longer time in the quasi-stationary (quiescent) state. Small noise below the resonant values is insufficient to drive the system to this region, whereas for too large a noise, the stochastic fluctuations completely take over, washing out the quasi-stationary regime. Note that for the faster adaptivity rate, the facilitatory role of coupling becomes more pronounced, as evinced by the fact that the curve $p_F(D)$ for $\epsilon = 0.1$ lies above the one for $\epsilon = 0.06$.

Discussion. – In the present paper, we have demonstrated a novel generic scenario for the onset of ISR, which involves an interplay between the local excitability feature and the adaptive dynamics of the couplings. For the example of two active rotators with coupling plasticity, we have shown that the spiking frequency corresponding to emergent oscillations varies non-monotonously with noise, displaying a minimum at a preferred noise level. Though the model *per se* is simplified, the underlying paradigm is relevant for combining the two core features of typical neuronal systems. The effect derives from the multi-timescale structure of the system, whereby the scale

separation between the local and the weight dynamics is tuned via adaptivity rate. Within a range of intermediate adaptivity rates, the deterministic dynamics of the full system exhibits multistability between the limit cycle attractors and the stable equilibria, each appearing in pairs due to the systems invariance to Z_2 symmetry. Applying the standard fast-slow analysis, we have shown that the resonant effect with noise is in fact plasticity-enhanced: plasticity promotes the impact of noise by guiding the fast flow toward the parameter domain where the stable equilibria become focuses instead of nodes. This mechanism increases the trapping efficiency by which the noise is able to deviate the systems trajectory from the metastable oscillatory states to the non-spiking regime. For faster adaptivity, the resonant effect is found to be more pronounced in a sense that the frequency dependence on noise shows deeper minima. Our scenario has proven to persist in a wide range of plasticity rules, interpolating between the cases analogous to Hebbian learning and STDP.

In earlier studies, observation of ISR has mostly been confined to Type-II neurons with intrinsic bistable dynamics, as in case of Hodgkin-Huxley or Morris-Lecar neurons near the subcritical Hopf bifurcation [3,6–9]. Even in case of networks, the macroscopic ISR effect has been linked to dynamical features of single units, only being modulated by the details of synaptic dynamics and the network topology [10]. In contrast to that, our results show that ISR may not rely on bistability of local dynamics, but may rather emerge due to the facilitatory role of coupling, here reflected in the interplay of multiscale dynamics and plasticity. Another distinction from most of the previous studies is that our scenario concerns Type-I units. For this class of systems, it is known that the dependence of the oscillating frequency of a single unit with noise is just monotonous [3,12], so that the resonant effect can only be observed in case of coupled units. So far, the latter case has been analyzed only once [5], but the underlying scenario is different from ours insofar as it involves static, rather than the adaptive couplings, and the effect *per se* is confined to a narrow region of the parameter space.

Quite recently, the onset of ISR has been reported for a single Fitzhugh-Nagumo oscillator [12], which is the first observation of the effect for Type-II neuron model in the vicinity of the supercritical Hopf bifurcation. Similar to the scenario we elaborated, ISR there also derives from the multiscale structure of the system. However, the actual mechanism behind the effect is associated to phase-sensitive (non-uniform) excitability of a limit cycle orbit conforming to relaxation oscillations [12]. These findings and the results here suggest that ISR may indeed provide a generic means of controlling and optimizing the firing rate in multi-timescale systems, which can be applied to neuronal activity, calcium signaling and other types of cell dynamics.

IF and IB would like to thank M. WOLFRUM and S. YANCHUK for useful discussions. The work of VK on

the third section was supported by the Russian Science Foundation, grant No. 16-42-01043. The work of VN on the fourth section was supported by the Russian Science Foundation, grant No. 14-12-01358.

REFERENCES

- [1] LINDNER B., GARCIA-OJALVO J., NEIMAN A. and SCHIMANSKY-GEIER L., *Phys. Rep.*, **392** (2004) 321.
- [2] MCDONNELL M. D. and WARD L. M., *Nat. Rev. Neurosci.*, **12** (2011) 415.
- [3] SCHMERL B. A. and MCDONNELL M. D., *Phys. Rev. E*, **88** (2013) 052722.
- [4] GAMMAITONI L., HÄNGGI P., JUNG P. and MARCHESONI F., *Rev. Mod. Phys.*, **70** (1998) 223.
- [5] GUTKIN B. S., JOST J. and TUCKWELL H. C., *EPL*, **81** (2008) 20005.
- [6] TUCKWELL H. C., JOST J. and GUTKIN B. S., *Phys. Rev. E*, **80** (2009) 031907.
- [7] UZUNTARLA M., CRESSMAN J. R., OZER M. and BARRETO E., *Phys. Rev. E*, **88** (2013) 042712.
- [8] UZUNTARLA M., *Phys. Lett. A*, **377** (2013) 2585.
- [9] UZUNTARLA M., TORRES J. J., SO P., OZER M. and BARRETO E., *Phys. Rev. E*, **95** (2017) 012404.
- [10] UZUNTARLA M., BARRETO E. and TORRES J. J., *PLoS Comput. Biol.*, **13** (2017) e1005646.
- [11] BUCHIN A., RIEUBLAND S., HÄUSSER M., GUTKIN B. S. and ROTH A., *PLoS Comput. Biol.*, **12** (2016) e1005000.
- [12] FRANOVIĆ I., OMEL'CHENKO O. E. and WOLFRUM M., *Chaos*, **28** (2018) 071105.
- [13] HAHN T. T. G., MCFARLAND J. M., BERBERICH S., SAKMANN B. and MEHTA M. R., *Nat. Neurosci.*, **15** (2012) 1531.
- [14] FRANOVIĆ I. and KLINSHOV V., *Chaos*, **28** (2018) 023111.
- [15] FRANOVIĆ I. and KLINSHOV V., *EPL*, **116** (2016) 48002.
- [16] SONG S., MILLER K. D. and ABBOTT L. F., *Nat. Neurosci.*, **3** (2000) 919.
- [17] FROMKE R. C. and DAN Y., *Nature*, **416** (2002) 433.
- [18] WANG H.-X., GERKIN R. C., NAUEN D. W. and BI G.-Q., *Nat. Neurosci.*, **8** (2005) 187.
- [19] LÜCKEN L., POPOVYCH O. V., TASS P. A. and YANCHUK S., *Phys. Rev. E*, **93** (2016) 032210.
- [20] KASATKIN D. V. and NEKORKIN V. I., *Radiophys. Quantum Electron.*, **58** (2016) 877.
- [21] BAČIĆ I., YANCHUK S., WOLFRUM M. and FRANOVIĆ I., *Eur. Phys. J. ST*, **227** (2018) 1077.
- [22] KASATKIN D., YANCHUK S., SCHÖLL E. and NEKORKIN V., *Phys. Rev. E*, **96** (2017) 062211.
- [23] DESTEXHE A. and RUDOLPH-LILITH M., *Neuronal Noise* (Springer, New York) 2012.
- [24] MAISTRENKO Y. L., LYSYANSKY B., HAUPTMANN C., BURLYKO O. and TASS P., *Phys. Rev. E*, **75** (2007) 066207.
- [25] AOKI T. and AOYAGI T., *Phys. Rev. Lett.*, **102** (2009) 034101.
- [26] AOKI T. and AOYAGI T., *Phys. Rev. E*, **84** (2011) 066109.
- [27] BERGLUND N. and GENTZ B., *Noise-Induced Phenomena in Slow-Fast Dynamical Systems* (Springer, Berlin) 2006.
- [28] LAING C. and LORD G. J. (Editors), *Stochastic Methods in Neuroscience* (Oxford University Press, London) 2009.
- [29] KUEHN C., *Multiple Time Scale Dynamics* (Springer International Publishing, Switzerland) 2015.
- [30] SHILNIKOV A., *Int. J. Bifurcat. Chaos*, **18** (2008) 2141.

Inverse stochastic resonance in a system of active rotators with adaptive coupling

Iva Bačić

Institute of Physics Belgrade

Inverse stochastic resonance is a phenomenon where an oscillating system shows a nonlinear response to noise, displaying a minimal oscillation frequency at an intermediate noise level. Such an effect has been indicated to play important functional roles in neuronal systems, contributing to reduction of spiking frequency in the absence of neuromodulators or to triggering of the on-off tonic spiking activity. We demonstrate a novel generic scenario for such an effect in a multi-timescale system, considering the example of emergent oscillations in two adaptively coupled active rotators with excitable local dynamics. The fast-slow analysis we carry out indicates that the plasticity plays a facilitatory role by guiding the fast-flow dynamics to parameter domains where the stable equilibria change character from nodes to foci, which ultimately enhances the influence of noise. The described scenario persists for different plasticity rules, underlying its robustness in light of potential application to neuronal systems.

Gas-phase X-ray action spectroscopy of protonated nanosolvated substance P peptide around O K-edge

I. Bačić¹, M. Lj. Ranković¹, F. Canon², V. Cerovski¹, C. Nicolas³, A. Giuliani^{3,4} and A. R. Milosavljević¹

¹ Institute of Physics Belgrade, University of Belgrade, Pregrevica 118, 11080 Belgrade, Serbia

² INRA, UMR1324 Centre des Sciences du Goût et de l'Alimentation, F-21000 Dijon, France

³ SOLEIL, l'Orme des Merisiers, St Aubin, BP48, 91192 Gif sur Yvette Cedex, France

⁴ INRA, UAR1008, CEPIA, Rue de la Géraudière, BP 71627, 44316 Nantes, France

We report preliminary results from unprecedented near edge X-ray absorption fine structure action spectroscopy of a gas-phase nanosolvated peptide ion. Doubly protonated substance P (Arg-Pro-Lys-Pro-Gln-Gln-Phe-Phe-Gly-Leu-Met-NH₂) cations have been isolated in a linear ion trap and submitted to soft X-ray synchrotron radiation by means of coupling a commercial quadrupole ion trap mass spectrometer (Thermo Finnigan LTQ XL) to the PLEIADES beamline at the SOLEIL synchrotron radiation facility (France) [1]. X-ray activation tandem mass spectra have been recorded for different photon energies, scanned over C, N and O K-edge ionization thresholds.

Figure 1 shows the photofragment ions yield corresponding to a total water loss (a normalized integral yield of all fragments corresponding to the loss of one or more water molecules) from the doubly protonated substance P cation nanosolvated with 11 water molecules $[M+2H+11H_2O]^{2+}$ upon soft X-ray irradiation. We observed that a resonant excitation of an O 1s electron to an unoccupied molecular orbital, following by a resonant Auger decay, induces an increased water detachment from the precursor.

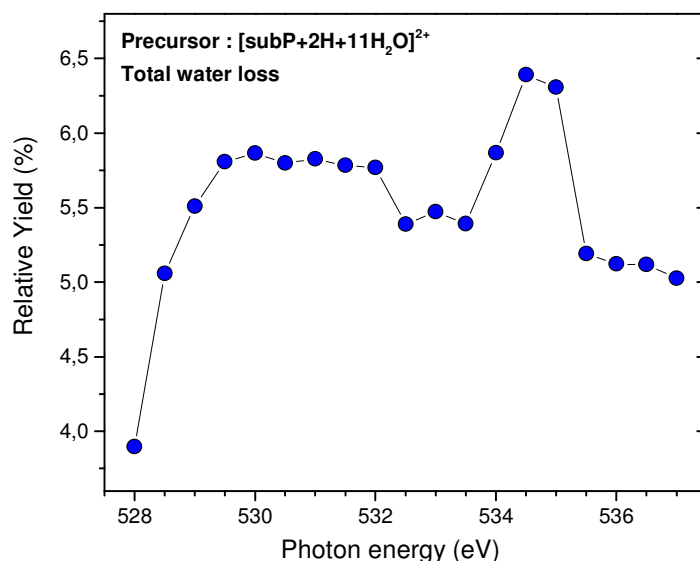


Fig.1. Photofragment ions yield that corresponds to a range m/z 674-766 (an integral yield of all fragments corresponding to the loss of one or more water molecules) from a doubly protonated nanosolvated substance P cation precursor $[M+2H+11H_2O]^{2+}$ (m/z 773.5).

Acknowledgements: Supported by ANR-08-BLAN-0065 (France), MESTD (Serbia) (projects 171020 and 171033) and COST Action XLIC. SOLEIL general staff (project 20140023).

REFERENCES

[1] A. R. Milosavljević et al., J. Phys. Chem. Letters 3, 1191 (2012).



Република Србија
Универзитет у Београду
Физички факултет
Д.Бр.2015/8018
Датум: 15.01.2019. године

На основу члана 161 Закона о општем управном поступку и службене евиденције издаје се

УВЕРЕЊЕ

Бачић (Јасмина) Ива, бр. индекса 2015/8018, рођена 12.06.1992. године, Суботица, Суботица-град, Република Србија, уписана школске 2018/2019. године, у статусу: самофинансирање; тип студија: докторске академске студије; студијски програм: Физика.

Према Статуту факултета студије трају (број година): три.
Рок за завршетак студија: у двоструком трајању студија.

Ово се уверење може употребити за регулисање војне обавезе, издавање визе, права на дечији додаток, породичне пензије, инвалидског додатка, добијања здравствене књижице, легитимације за повлашћену возњу и стипендије.

Овлашћено лице факултета



[Handwritten signature]



Република Србија
Универзитет у Београду
Физички факултет
Д.Бр.2015/8018
Датум: 15.01.2019. године

На основу члана 161 Закона о општем управном поступку и службене евиденције издаје се

УВЕРЕЊЕ

Бачић (Јасмина) Ива, бр. индекса 2015/8018, рођена 12.06.1992. године, Суботица, Суботица-град, Република Србија, уписана школске 2018/2019. године, у статусу: самофинансирање; тип студија: докторске академске студије; студијски програм: Физика.

Према Статуту факултета студије трају (број година): три.
Рок за завршетак студија: у двоструком трајању студија.

Ово се уверење може употребити за регулисање војне обавезе, издавање визе, права на дечији додаток, породичне пензије, инвалидског додатка, добијања здравствене књижице, легитимације за повлашћену возњу и стипендије.

Овлашћено лице факултета



[Handwritten signature]



UNIVERSITY OF BELGRADE FACULTY OF PHYSICS

Студентски трг 12, 11000 Београд, П.П. 44, Тел: 011-7158-151, Факс: 011-3282-619
Studentski trg 12, 11000 Belgrade, Serbia, POB 44, Tel: +381-11-7158-151, Fax: +381-11-3282-619
www.ff.bg.ac.rs e-mail: dekanat@ff.bg.ac.rs

Број 2602014

Београд, 05. 11. 2014. године

На основу члана 161. Закона о општем управном поступку и члана 4. Правилника о садржају и облику образаца јавних исправа које издају више школе, факултети и универзитети, по захтеву, Бачић (Јасмина) Иве издаје се следеће

У В Е Р Е Њ Е

БАЧИЋ (ЈАСМИНА) ИВА рођен- а 12. 06. 1992. године у Суботици, Суботица, Република Србија уписан-а школске 2010/2011. године на четворогодишње основне академске студије првог степена, Студијска група **ФИЗИКА**, смер: **Теоријска и експериментална физика**, положио-ла је испите предвиђене наставним планом и програмом наведене Студијске групе и завршио-ла студије на Физичком факултету 28. октобра 2014. године, са средњом оценом 9,44 (девет и 44/100) у току студија и постигнутим укупним бројем 244 ЕСПБ (двестачетрдесетчетири ЕСП бодова) и тиме стекао-ла високу стручну спрему и стручни назив

ДИПЛОМИРАНИ ФИЗИЧАР

Уверење се издаје на лични захтев, а служи као доказ о завршеној високој стручној спремности до издавања дипломе.

**ДЕКАН
ФИЗИЧКОГ ФАКУЛТЕТА**

Проф. др Јаблан Дојчиловић

6. 11. 2015.

Иве Бачић





УНИВЕРЗИТЕТ У БЕОГРАДУ ФИЗИЧКИ ФАКУЛТЕТ
UNIVERSITY OF BELGRADE FACULTY OF PHYSICS

Студентски трг 12, 11000 Београд, П.П. 44, Тел: 011-7158-151, Факс: 011-3282-619
Studentski trg 12, 11000 Belgrade, Serbia, POB 44, Tel: +381-11-7158-151, Fax: +381-11-3282-619
www.ff.bg.ac.rs e-mail: dekanat@ff.bg.ac.rs

Број 2572015
Београд, 09. 11. 2015. године

На основу члана 99. Закона о високом образовању ("Сл. гласник Републике Србије" број 76/05), и члана 9. и 184. Статута Физичког факултета (број 442/1 од 10.10.2006 и дате сагласности Универзитета у Београду број 02 612-1852 од 29.01.2007), у складу са Правилником о садржају и облику образаца јавних исправа које издају високошколске установе ("Сл. гласник Републике Србије" број 21/06, 66/06 и 8/07) издаје се следеће

У В Е Р Е Њ Е

БАЧИЋ (СЛАВЕН) ИВА рођен-а 12. 06. 1992. године у Суботици, Суботица, Република Србија уписан-а школске 2014/2015. године, завршио-ла је дипломске академске студије – студије другог степена (мастер) на студијском програму Физичког факултета Универзитета у Београду, смер: ТЕОРИЈСКА И ЕКСПЕРИМЕНТАЛНА ФИЗИКА, дана 22. октобра 2015. године, са просечном оценом 9,67 (девет и 67/100) у току студија и постигнутим укупним бројем 60 ЕСПБ (шездесет ЕСП бодова) и тиме стекао-ла високо образовање и академски назив:

МАСТЕР ФИЗИЧАР

Уверење се издаје на лични захтев, а служи као доказ о завршеној стручној спреми до издавања дипломе.



ДЕКАН

Jablan Dojčilović
Проф. др Јаблан Дојчиловић



ДОКТОРСКЕ СТУДИЈЕ

ПРЕДЛОГ ТЕМЕ ДОКТОРСКЕ ДИСЕРТАЦИЈЕ КОЛЕГИЈУМУ ДОКТОРСКИХ СТУДИЈА

Школска година
2018/2019

Подаци о студенту

Име

Ива

Презиме

Бачић

Број индекса

8018/2015

Научна област дисертације

Физика кондензоване материје и
статистичка физика

Подаци о ментору докторске дисертације

Име

Игор

Презиме

Франовић

Научна област

Физика кондензоване материје и
статистичка физика

Звање

Научни сарадник

Институција

Институт за физику у Београду

Предлог теме докторске дисертације

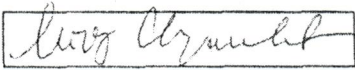
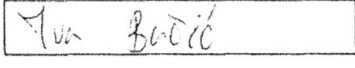
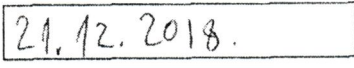
Наслов

Self-Organization in Coupled Excitable Systems: Interplay Between Multiple Timescale Dynamics and Noise

(Самоорганизација у спрегнутим ексцитабилним системима: садејство вишеструких временских скала и шума)

Уз пријаву теме докторске дисертације Колегијуму докторских студија, потребно је приложити следећа документа:

1. Семинарски рад (дужине до 10 страница)
2. Кратку стручну биографију писану у трећем лицу јединине
3. Фотокопију индекса са докторских студија

Потпис ментора	
Потпис студента	
Датум	

Мишљење Колегијума докторских студија	
Након образложења теме докторске дисертације Колегијум докторских студија је тему	
прихватио <input checked="" type="checkbox"/>	није прихватио <input type="checkbox"/>
Датум	Продекан за науку Физичког факултета
